Surprising microscopy subtleties: measuring picoscale thicknesses, visualizing core orbitals, and detecting charge transfer using the TEM

A DISSERTATION
SUBMITTED TO THE FACULTY OF THE GRADUATE SCHOOL
OF THE UNIVERSITY OF MINNESOTA
BY

Michael Luke Odlyzko

IN PARTIAL FULFILLMENT OF THE REQUIREMENTS
FOR THE DEGREE OF
DOCTOR OF PHILOSOPHY

Advisor: K. Andre Mkhoyan

November, 2015

Acknowledgements

Any good work that I have done has definitely been shaped by the influence and support of others.

First and foremost, I acknowledge the triune God as my creator, sustainer, savior, and king. Anything truly good in any human being, anything truly beautiful in this universe, anything truly worth hoping for in the future... all are authored by Him and show that He alone is worthy of worship and total trust. My work has no lasting value or meaning apart from Him. Anything really praiseworthy in who I am and what I have done is thanks to his work in creating and re-creating me; all of my folly, snottiness, insecurity, cruelty, and other wretched are rebellions against Him that He alone can forgive and subdue. I have tasted and seen that He is good, and I want more.

Throughout my life, my parents Paul and Anna and sister Kasia have been full of affection, generosity, and faithfulness. During my time in Minnesota, my wife Louisa, Louisa's family (Bob, Connie, Nate, Jon), my old roommates (Gagan, Jesse, Forrest), my uncle Andrew, and my brother-in-law Micah have all been part of a new "extended" family to me. The care of family has been precious and grounding to me, all the more so because they all seem to have given me far more than they received from me.

I am very grateful to have been advised by Andre. I might not have managed to complete my PhD with any other advisor even in such a great department; regardless, I am pretty sure that I could not have done it as happily and sanely. Andre has proven himself exceptionally warm, loyal, adaptable, service-minded, shrewd, frank, curious,

clear-sighted, and colorful. I could not have asked for a better companion-guide for my oft-wandering, oft-lonely, but always-interesting explorations of science (and life generally) in these last six years. His good-willed hunger to teach, explore, and achieve is a blessing to those who have the privilege of working with him.

Perhaps just as important as a great adviser, I have been blessed with a great group of peers. Al, Andrew, and Anudha were so good as mentors, colleagues, and friends, in ways too diverse to enumerate and with a quality that I cannot match. In his quiet thoroughness, caring, and humility, Jong has been a model senior scientist, and a model person period. Al, Anudha, Claire, Jake, and Danielle each did so much to make lab a stimulating, comfortable, and fun place. Most recently, I have loved sharing a lab with Eric, Prashant, Ryan, Claire, Jake, Hwanhui, and Danielle; and although I will not be counted among Andre's successful microscopist "progeny," any of them could easily join Jong and Andrew in carrying on a fertile "family line."

My passions for learning and problem-solving has been heavily cultivated by my research endeavors, but it has a long history preceding it. My father has done so much to stimulate independent thought and love for learning throughout the years, even when I have found his methods frustrating. He is the main reason that I have gone as far as I have in scientific learning and investigation. In addition to him, though, there are many others who have been especially impactful in their skillful, enthusiastic teaching: John Figliewicz and Linda Rodenburg of Thomas Middle School; James Behymer, Karen Levin, and Chet Pierce of Buffalo Grove High School; Paul Kwiat, S. Lance Cooper, John Weaver, Angus Rockett, and Peter Abbamonte of the University of Illinois, Urbana-Champaign; and Eray Aydil and Chris Leighton of the University of Minnesota, Twin Cities.

Thank you to all those named above and many others who have taught, befriended, and otherwise shaped me. My life and work do not do justice to the generous contributions that you have made.

Dedication

To Dad: I want to be you when I grow up.

To Louisa and Baby: I want to grow up for you.

And to all who thirst for truths to learn and problems to solve: may you channel that drive far more fruitfully than I have.

Abstract

50 years ago, Richard Feynman delivered a now-famous address outlining why there was "plenty of room left at the bottom": there remained much progress to be made in seeing and manipulating matter all the way down to the atomic scale. One of many means to that end, argued Feynman, was to make electron microscopes better. Why could not electrons with wavelengths of a few picometers not be used to clearly image atoms hundreds of picometers in size? Why could not electron beams be used to pattern miniscule wires a handful of metal atoms across?

Over the course of decades, Feynmans vision has been pursued zealously with rich reward, not least in the electron microscopy field. Enabled by the development of bright field-emission electron sources, high-resolution polepieces, and now aberration correctors, transmission electron microscopy (TEM) at atomic resolution has become routine. Seemingly, there is little room left at the bottom; after all, once you can clearly see atoms, what more is there left to do? Thankfully, there is plenty. Much of the hard work has been in the development of equipment that expands TEM to allow unprecedented spatially resolved analysis of elemental composition, inelastic scattering, and temporal processes. But there are also many opportunities to uncover new information using now widely available techniques and equipment.

In the studies presented here, there has been some success in following the latter path. In tandem with careful computational analysis, selected-area electron diffraction allows not only determination of crystal symmetry, lattice parameter, and microstructure, but also measurements of material thickness on the scale of atomic layers. Supported by careful data processing and rigorous simulations, spatially resolved X-ray spectroscopy data is converted into real-space measurements of core-level electronic orbitals, in addition to providing routine atomic resolution chemical mapping. And aided

by the development of novel bonding-inclusive TEM simulations, the detection of chemical bonding using nominally bonding-independent high-angle elastic scattering is both theoretically predicted and experimentally observed. Even once you have gone all the way down to the bottom, there is still a wide world of wonders left to explore.

Contents

Acknowledgements **i**

Dedication **iii**

Abstract **iv**

List of Tables **ix**

List of Figures **x**

1 Introduction **1**

2 Methods **6**

2.1 Conventional transmission electron microscopy 7

2.1.1 Imaging in CTEM 7

2.1.2 Diffraction in CTEM 7

2.2 Scanning transmission electron microscopy 9

2.2.1 Annular dark-field STEM 10

2.2.2 Electron energy-loss spectroscopy 12

2.2.3 X-ray energy-dispersive spectroscopy 13

2.3 Transmission electron microscope resolution 13

2.4 Transmission electron microscopy simulation 16

2.4.1 Multislice method 16
2.4.2 Simulating imaging and diffraction 16
2.5 Transmission electron microscopy resources at the University of Minnesota 17
2.5.1 Characterization Facility 17
2.5.2 Minnesota Supercomputing Institute 18

3 Measuring thicknesses of atomically thin layered crystals 19
3.1 Introduction 19
3.2 Methods 21
3.3 ADF-STEM imaging 24
3.3.1 Zone axis orientation 24
3.3.2 Tilt series 29
3.3.3 Origin of ADF-STEM tilt series effects 37
3.4 SAED characterization 38
3.4.1 Zone axis orientation 38
3.4.2 Tilt series 40
3.4.3 Origin of SAED tilt series effects 50
3.5 Conclusion 55

4 Probing core electron orbitals and measuring the delocalization of core-level excitations 57
4.1 Introduction 57
4.2 Methods 58
4.3 Results and discussion 62
4.3.1 Experimental XEDS spectrum imaging 63
4.3.2 Theoretical framework for XEDS spectrum imaging 65
4.3.3 Deconvolution of probe effects from XEDS spectrum images . . . 68
4.3.4 Measurement of impact parameters using XEDS spectrum images 76
4.4 Conclusion 79

5 Computational predictions of bonding effects for ADF-STEM imaging 81

5.1 Introduction . . . 81

5.2 Methods . . . 83

5.3 Results and Discussion . . . 86

5.3.1 HAADF imaging . . . 86

5.3.2 Beam propagation . . . 92

5.3.3 Incident probe effects . . . 96

5.3.4 Detector geometry effects . . . 99

5.3.5 Thermal vibration effects . . . 101

5.4 Conclusions . . . 104

6 Experimental testing of bonding effects for ADF-STEM imaging 106

6.1 Introduction . . . 106

6.2 Methods . . . 108

6.3 Results and discussion . . . 116

6.3.1 Experimental imaging . . . 116

6.3.2 Multislice simulation . . . 119

6.3.3 Comparison of experiment and simulation . . . 122

6.4 Conclusion . . . 125

References 127

A Slice thickness effects in multislice simulation 138

List of Tables

5.1 Comparison of the crystal structure, bond length, bond polarity, and bond valency of the crystals studied. Crystals increase in bond polarity from left to right. 83

5.2 Rayleigh criterion diffraction-limited resolution of the STEM probes considered in this study. Each value corresponds to the radius of the central Airy disk formed in each condition, which is approximately equal to the full-width-at-half-maximum (FWHM) of an aberration-free probe. . . . 85

6.1 Comparison of key properties of AlN and MgO crystals. Both materials are insulators with large net charge transfer. 108

6.2 Summary of parameters used to simulate conditions of each AlN imaging experiment. Zero corresponds to Gaussian focus, while positive values of defocus correspond to overfocus. 122

6.3 Summary of parameters used to simulate conditions of each MgO imaging experiment. Zero corresponds to Gaussian focus, while positive values of defocus correspond to overfocus. 122

List of Figures

2.1 Schematics of CTEM operation in (a) bright-field image and (b) selected-area diffraction modes. 8

2.2 (a) Ray diagram of a (S)TEM operating as a scanning transmission electron microscope. (b) FEI Titan G2 60–300 (S)TEM at the University of Minnesota Characterization Facility. (c) Schematic of the probe scan coils of a STEM. 10

2.3 Schematic of electron-sample interaction under TEM illumination of a thin specimen. 11

2.4 Schematic of parallel EELS and ADF imaging in STEM. 12

2.5 Example of different XEDS spectrum images of ⟨001⟩-oriented STO formed using each of five distinct characteristic X-ray peaks. 14

2.6 Comparison of HAADF-STEM imaging of ⟨110⟩-oriented Si using (a) an uncorrected TEM and (b) an aberration-corrected TEM. Scale bars are 0.5 nm in length, and the separation between nearest-neighboring columns is 0.136 nm. 15

2.7 Schematic of multislice TEM simulation showing the scattering and propagation of a STEM probe through an AlN crystal. 17

3.1 Tilt axis conventions; in each case, the blue vector indicates the [0001] zone axis. (a) Schematic illustrating an x-tilt performed on a h-BN monolayer. (b) Schematic illustrating a y-tilt performed on a h-BN monolayer. 22

3.2 Structural models of single layer 2H and 1T MX_2 crystals, where M is a Mo or W site and X is a S site, and tilt conventions. (a): 2H MX_2 structure; (top) [0001] view and (bottom) $\left[\bar{1}2\bar{1}0\right]$ view. (b): 1T MX_2 structure; (top) [0001] view and (bottom) $\left[\bar{1}2\bar{1}0\right]$ view. X-tilt corresponds to a rotation around the $\left[\bar{1}2\bar{1}0\right]$ axis and y -tilt corresponds to a rotation around the $\left[10\bar{1}0\right]$ axis. (c) Illustration of the stacking of 2H and 1T MX_2 layers using the M- and X-site convention. 23

3.3 Line scans for [0001]-oriented samples of h-BN along a $\left[11\bar{2}0\right]$ direction; the red stripe indicates the six-pixel band of the image for which line scans were performed. ADF detector intensity, normalized to the incident beam current, is plotted on a linear scale. 25

3.4 ADF-STEM intensity ratios of X-site to M-site at [0001] zone axis for 1–4 layers of 2H MX_2 and 1T MX_2. Yellow dots represent the X-site and blue dots the M-site. 2H configuration alternates the higher intensity site as a result of the ABA-BAB stacking, whereas in 1T configuration with ABA-ABA stacking it remains constant (see also Figure 3.2(c)). For comparison, experimental ADF-STEM image intensity ratios for 2H and 1T MoS_2 monolayers from Eda et al. are also shown. 26

3.5 Simulated ADF-STEM intensity linescans at [0001] zone axis: (a) 2H MoS_2; (b) 2H-WS_2; (c) 1T MoS_2; (d) 1T WS_2. Each line profile is averaged over a strip 12 pixels (or 0.04 nm) wide. The insets are corresponding ADF-STEM images with arrows indicating directions of linescans. Intensities are normalized to the incident beam current. 30

3.6 Series of simulated ADF-STEM images of atomically thin h-BN for an aberration-corrected 100 keV TEM, x-tilts. For a one-layer-thick region, tilt only serves to produce a distorted projection of the honeycomb-structured layer; for multiple-layer regions, tilting introduces distinctive complex distortions to the images, visible as streaking perpendicular to the y-axis. Linear intensity scale; scale bar = 0.2 nm. 31

3.7 Series of simulated ADF-STEM images of atomically thin h-BN for an aberration-corrected 100 keV TEM, y-tilts. For a one-layer-thick region, tilt only serves to produce a distorted projection of the honeycomb-structured layer; for multiple-layer regions, tilting introduces distinctive complex distortions to the images, visible as streaking perpendicular to the y-axis. Linear intensity scale; scale bar = 0.2 nm. 32

3.8 Simulated ADF-STEM images of 2H MoS_2 at various x- and y-tilt angles. Both tilt directions produce unique intensity patterns at all thicknesses as a result of overlapping of Mo and S atoms. Color bars are scaled to each row with intensities normalized to the incident beam; scale bars = 0.18 nm. 33

3.9 Simulated ADF-STEM images of 2H WS_2 at various x- and y-tilt angles. Both tilt directions produce unique intensity patterns at all thicknesses as a result of overlapping of W and S atoms. Color bars are scaled to each row with intensities normalized to the incident beam; scale bars = 0.18 nm. 34

3.10 Simulated ADF-STEM images of 1T MoS_2 at various x- and y-tilt angles. Both tilt directions produce unique intensity patterns at all thicknesses as a result of overlapping of Mo and S atoms. Color bars are scaled to each row with intensities normalized to the incident beam; scale bars = 0.18 nm. 35

3.11 Simulated ADF-STEM images of 1T WS_2 at various x- and y-tilt angles. Both tilt directions produce unique intensity patterns at all thicknesses as a result of overlapping of Mo and S atoms. Color bars are scaled to each row with intensities normalized to the incident beam; scale bars = 0.18 nm. 36

3.12 Crystal model of the 2H polymorph of MX_2: (a) Monolayer MX_2 in [0001] projection tilted at different angles of x-tilt, (b) 1 to 4 layers of MX_2 in [0001] projection tilted to 200 mrad of x-tilt. Corresponding simulated ADF-STEM images of 2H MoS_2 are presented as insets. 38

3.13 Line scans for [0001]-oriented samples of h-BN through $\{10\bar{1}0\}$ and $\{11\bar{2}0\}$ reflections; red stripe indicates the band of the diffraction pattern for which line scans were performed. Diffracted spot intensities are plotted on a linear intensity scale, with each line scan individually normalized to its maximum value. 39

3.14 PACBED patterns for [0001]-oriented samples of h-BN (a) 1, (b) 2, (c) 3, and (d) 4 atomic layers thick. Linear intensity scale; scale bar = 2 nm^1. 40

3.15 Intensity ratios of $\{10\bar{1}0\}$ to $\{11\bar{2}0\}$ spots of [0001] zone axis SAED pattern simulated for both materials and polymorphs. The yellow and orange hexagon traces in the inset diffraction pattern are the two sets of spots that were used to evaluate the average $I_{\{10\bar{1}0\}}$ and $I_{\{11\bar{2}0\}}$. . . . 41

3.16 Series of simulated ADF-STEM images of atomically thin h-BN for an aberration-corrected 100 keV TEM, x-tilts. For a one-layer-thick region, tilt only serves to produce a distorted projection of the honeycomb-structured layer; for multiple-layer regions, tilting introduces distinctive complex distortions to the images, visible as streaking perpendicular to the y-axis. Linear intensity scale; scale bar = 0.2 nm. 42

3.17 Series of simulated ADF-STEM images of atomically thin h-BN for an aberration-corrected 100 keV TEM, y-tilts. For a one-layer-thick region, tilt only serves to produce a distorted projection of the honeycomb-structured layer; for multiple-layer regions, tilting introduces distinctive complex distortions to the images, visible as streaking perpendicular to the y-axis. Linear intensity scale; scale bar = 0.2 nm. 43

3.18 Intensity variation of diffracted spots as a function of tilt angle and sample thickness. For both x-tilt and y-tilt series, one $\{10\bar{1}0\}$ and one $\{11\bar{2}0\}$ reflection was chosen and then analyzed for samples 14 layers thick. (a) $(10\bar{1}0)$ over x-tilt series. (b) $(11\bar{2}0)$ over x-tilt series. (c) $(01\bar{1}0)$ over y-tilt series (d) $(\bar{1}2\bar{1}0)$ over y-tilt series. Each simulated data point is a 7×7 average of the pixels surrounding the center of that diffracted spot. Intensity values are normalized to the averaged value at the [0001] zone axis. 44

3.19 Simulated SAED patterns of 2H MoS_2 at various x- and y-tilt angles. Both monolayer and multi-layer patterns contain diffraction spots that vanish with tilt, primarily for the band of spots perpendicular to the tilt axis. Linear intensity scaling; scale bars = 2.4 $nm^{-}1$. 46

3.20 Simulated SAED patterns of 1T MoS_2 at various x- and y-tilt angles. Both monolayer and multi-layer patterns contain diffraction spots that vanish with tilt, primarily for the band of spots perpendicular to the tilt axis. Linear intensity scaling; scale bars = 2.4 $nm^{-}1$. 48

3.21 SAED spot intensity variations as a function of tilt angle for 1- to 4-layered 2H MoS_2. The spot tracked in each plot is highlighted in red in the sample diffraction pattern. Scattered points represent simulated multislice data; solid lines represent a kinematic diffraction calculation. (a) $\left(10\bar{1}0\right)$ over y-tilt series. (b) $\left(1\bar{2}10\right)$ over x-tilt series. (c) $\left(1\bar{1}00\right)$ over y-tilt series (d) $\left(2\bar{1}\bar{1}0\right)$ over x-tilt series. Each simulated data point is a $12times12$ average of the pixels surrounding the center of that diffracted spot. Intensity values are normalized to the averaged value at the [0001] zone axis. 49

3.22 Single-period plot of the relrod intensity for identical atomic layers spaced 0.333 nm apart. If calculated using the scattering factors of B and N atoms with correct stacking order, these intensities would correspond to the exact out-of plane modulation of the relrods (the exact modulation is in fact mapped in the SAED tilt-effect simulations presented previously). 52

3.23 Intensity variation along reciprocal space lattice rod: (a) $\left(10\bar{1}0\right)$ spot, 2H MoS_2; (b) $\left(1\bar{2}10\right)$ spot, 2H MoS_2; (c) $\left(01\bar{2}0\right)$ spot, 1T MoS_2; (d) $\left(1\bar{2}10\right)$ spot, 1T MoS_2. Plots are constructed using the kinematic model of electron diffraction. Intensity values are normalized to the value at s_z=0. 54

4.1 (a) HAADF-STEM image of STO viewed along a ⟨001⟩ crystallographic direction. A model of the atomic positions is overlaid on the image to clarify identification of atomic columns. (b) Composite STEM-XEDS map of STO, superposing combined Sr K and L (purple), Ti K (green), and O K (yellow) maps. Individual XEDS maps of Sr K (c) and Sr L (d) are also shown, demonstrating simultaneous atomic-resolution XEDS using two different characteristic X-ray types. The scale bar is 0.2 nm in length. XEDS maps were acquired simultaneously by collecting a full 0-20 keV XEDS spectrum at each probe position. The non-circular symmetry of the STEM probe tails produces slightly asymmetric shapes of the atomic columns in HAADF-STEM images and STEM-XEDS maps, a subtle effect that is largely invisible in data sets with lower signal-to-noise ratios. 60

4.2 Resolution tests after probe correction and before XEDS acquisition from each days experiment: (a) and (b), high-resolution HAADF-STEM image from the Au specimen and its FFT; (c) and (d), high-resolution HAADF-STEM image from the STO specimen and its FFT. The probe currents (I_p) for the experiments were indicated on the HAADF-STEM images. Information limits and selected lattice spacings are indicated on the corresponding FFTs. 61

4.3 (a) Raw Sr L XEDS map of 600×600 pixel^2 image size, where 49 overlapping squares 101×101 pixel^2 in size are selected with each centered on a Sr atomic column. (b) 49 individual single-column images from (a). A reference image, a 2D gaussian with a FWHM of 0.148 nm, was used to align the 49 images by applying a cross-correlation algorithm before averaging them into a resulting final image. 63

4.4 Iteration of cross-correlation process of experimental XEDS maps from Day II to determine a proper size of the reference image. The first cycle of each cross-correlation sequence was done using a 2D gaussian image with FHWM of 0.08 nm (solid) and 0.20 nm (open). Converged FWHM reference values are indicated by horizontal dotted lines for each case: Ti K (0.135 nm), Sr K (0.139 nm), and Sr L (0.148 nm) for the XEDS maps. 64

4.5 (Individual Sr K and L XEDS maps from the Sr column of STO viewed along a ⟨001⟩ crystallographic direction alongside individual Ti K and L XEDS maps from the Ti/O column of STO viewed along the same direction for four independent data sets: (a) Day I, (b) Day II-128, (c) Day II-256, and (d) Day III. Azimuthally averaged radial profiles presented at right show that for each atom the L map is wider than the K map. These maps constitute the cross-correlated average of data from approximately 300–600 identical atomic columns each, with all maps obtained simultaneously. 66

4.6 (a) Perspective rendering of a ball-and-stick atomic model of the STO crystal viewed along a ⟨001⟩ direction. Sr atoms are in purple, Ti are in green, and O are in yellow. The square box around the Sr atomic column drawn by the dashed line indicates the area considered in channeling simulations. (b)-(e) Simulated intensities of a STEM beam located 40 pm away from the Sr atomic column at depths of 0.0, 3.5, 5.5, and 10.5 nm in the crystal. The position of the Sr column is indicated by the purple dot and the extents of both 1s and 2p orbitals are highlighted by the solid and dashed orange circles, respectively. As the probe propagates through the crystal it is drawn onto the Sr atomic column and oscillates inside the column atoms, intensifying the overlap with core-level orbitals. The thermal vibrations of atoms are taken into account. The scale bar is 50 pm in length. 67

4.7 Linescans of the depth-averaged probe intensity for three STEM probes of varying size in the vicinity of the Sr column. The linescan direction within the STO crystal is indicated by a white dashed line in the inset. 69

4.8 Comparison of Sr 1s, Sr 2p, Ti 1s, and Ti 2p orbitals. (a) Simple projected charge density approximation and (b) first-principles excitation potential in the local approximation for 300 keV incident electrons. 70

4.9 Linescans of probes with and without finite source size used to model each experiment. (a) Day I: $d_p = 45$ pm, $d_{ss} = 110$ pm, (b) Day II: $d_p = 45$ pm, $d_{ss} = 90$ pm, and (c) Day III: $d_p = 45$ pm, $d_{ss} = 120$ pm. 70

4.10 Source-size removal for Day II-128 images, left to right: experimental XEDS maps (processed as discussed), maps formed by restoring source distribution to source-removed data, and the difference between the two. Difference plots (root-mean-square difference given in top right corner of each difference map) illustrate successful source-size removal by the Richardson-Lucy method. All plots span 11 u.c.^{2} in area. 72

4.11 Comparison of projected orbital theory with best-fitting lorentzian trial solution determined from each experiment. All best fits were determined from background-subtracted point-source comparisons. 75

4.12 Comparison of the radial distribution of experimentally observed and calculated transition potentials, alongside calculated projected charge densities, for (a) Sr 1s, (b) Sr 2p, (c) Ti 1s, and (d) Ti 2p orbitals. All sets of theoretical calculations include the effects of atomic thermal vibrations. Calculations with excitation broadening are indicated by dashed black lines and those without excitation broadening by solid colored lines. . . 77

4.13 Comparison of experimentally measured and theoretically predicted impact parameters. Experimental measures correspond to the average of all four independent experiments, with error bars corresponding to one standard deviation of the data for each orbital. 78

5.1 Schematics of image simulation using different bonding models. Dark-colored regions indicate contributions of atomic ion cores (nucleus plus all non-valence electrons). Light-colored volumes indicate contributions of the valence electrons of a neutral atom. 84

5.2 For an x-z profile of the HAADF signal along the indicated line in $\langle\bar{2}110\rangle$-oriented AlN (a), HAADF-STEM image simulations of a 25 mrad 100 keV probe using each bonding model (b) give slightly different depth-dependent contrast, most visible as a weakening of the N column shoulder as a function of increasing charge transfer. 87

5.3 For an x-z profile of the HAADF signal along the indicated line in $\langle\bar{2}110\rangle$-oriented AlN (a), HAADF-STEM image simulations of a 25 mrad 100 keV probe using each bonding model (b) give slightly different depth-dependent contrast, most visible as a weakening of the N column shoulder as a function of increasing charge transfer. 88

5.4 Normalized HAADF x-z profile differences of (a) BCM and (b) FIM bonding models relative to IAM reference, for $\langle\bar{2}110\rangle$-oriented wurtzite crystals. Crystals increase in polarity from left to right. BCM vs. IAM differences are weaker than FIM vs. IAM. 89

5.5 Normalized HAADF x-z profile differences of (a) BCM and (b) FIM bonding models relative to IAM reference, for $\langle 110\rangle$-oriented halite crystals. Crystals increase in polarity from left to right. BCM vs. IAM differences are weaker than FIM vs. IAM. 90

5.6 Normalized HAADF x-z profile differences for $\langle\bar{2}110\rangle$-oriented AlN with increasing charge transfer between Al and N from left to right: low polarity BCM model (electron potential energy on Al artificially lowered by 1 eV), standard BCM model, high-polarity BCM model (electron potential energy on Al artificially increased by 1 eV), and standard FIM model. As charge transfer between columns increases, normalized x-z profile differences for $\langle\bar{2}110\rangle$-oriented AlN reveal proportional strengthening of Al column intensity and weakening of N column intensity. 91

5.7 Contrast signal for a 100 keV probe with 25 mrad convergence in $\langle\bar{2}110\rangle$-oriented AlN and $\langle 110\rangle$-oriented NaF. The contrast signal varies both as a function of depth and bonding model. When the difference in Z is larger, the contrast signal is larger and varies more widely as a function of depth. 91

5.8 Change in HAADF contrast signal as a function of depth relative to IAM for a 100 keV probe with 25 mrad convergence. Effect of bonding on contrast is stronger for FIM model than for BCM, and in either case maximum changes in contrast ratio emerge at thicknesses of 20 nm or greater. 92

5.9 Intensity along line between nearest-neighboring columns in $\langle\bar{2}110\rangle$-oriented AlN as a function of depth, with incident 25 mrad 100 keV probe centered on the N column. Intensity fluctuates with thickness on the N column, but also couples to the neighboring Al column. Beam propagation visibly changes with bonding model. 93

5.10 Probe intensity incident on atomic columns as a function of depth for $\langle\bar{2}110\rangle$-oriented wurtzite crystals, with incident probe centered on the (a) cation column and (b) anion column. Bond polarity increases from left to right. Intensity is tracked on incident columns, first-nearest-neighboring columns, and second-nearest-neighboring columns. 94

5.11 Probe intensity incident on atomic columns as a function of depth for ⟨110⟩-oriented halite crystals, with incident probe centered on the (a) cation columns and (b) anion column. Bond polarity increases from left to right. Intensity is tracked on incident columns, first-nearest-neighboring columns, and second-nearest-neighboring columns. 95

5.12 Probe intensity incident on atomic columns as a function of depth for ⟨100⟩-oriented cubic crystals, with incident probe centered on the (a) C column in d-C, (b) B column in c-BN, and (c) N column in c-BN. Bond polarity increases from left to right. Intensity is tracked on incident columns, first-nearest-neighboring columns, second-nearest-neighboring columns, and third-nearest-neighboring columns. 95

5.13 Change in contrast signal relative to IAM for 25 mrad probes imaging $\langle\bar{2}110\rangle$-oriented AlN, plotted as a function of depth, bonding model, and electron energy. With convergence angle fixed, the magnitude of contrast change decreases as probe energy increases. Also, the period of depth-dependent fluctuations in the contrast difference increases as probe energy increases. 97

5.14 Change in contrast signal relative to IAM for 200 keV probes imaging $\langle\bar{2}110\rangle$-oriented AlN, plotted as a function of depth, bonding model, and convergence angle. With beam energy fixed, the magnitude of contrast change decreases as convergence angle increases. The period of depth-dependent fluctuations in the contrast difference does not change with convergence angle, only with bonding model. 98

5.15 Change in contrast signal relative to IAM for 35 mrad 200 keV probes imaging $\langle\bar{2}110\rangle$-oriented AlN, plotted as a function of depth, bonding model, and source size. With convergence angle fixed, the magnitude of contrast change decreases as source size increases. The period of depth-dependent fluctuations in the contrast difference does not change with source size, only with bonding model. 99

5.16 Change in contrast ratio relative to IAM for 35 mrad probes imaging $\langle\bar{2}110\rangle$-oriented AlN, plotted as a function of depth, bonding model, and detector geometry for (a) 60 keV, (b) 100 keV, and (c) 200 keV. Although all detectors collect high-angle-scattered electrons, decreasing the contribution of coherent beams from LAADF to HAADF to UHAADF settings strengthens the contrast fluctuations due to channeling and beam spreading effects. 100

5.17 Examples of temperature effects on contrast, 100 keV probe with 25 mrad convergence: (a) contrast signal plots for $\langle\bar{2}110\rangle$-oriented AlN with and without thermal vibrations, (b) differences in BCM vs. IAM contrast signal for $\langle\bar{2}110\rangle$-oriented AlN and $\langle 110\rangle$-oriented LiF. TDS effects decrease image contrast for all bonding models, as well as perturb the contrast changes due to bonding. 103

5.18 Examples of temperature effects on contrast: 100 keV probe with 25 mrad convergence for LAADF, HAADF, and UHAADF detectors. TDS effects slightly increase the magnitude of contrast fluctuations relative to IAM and slightly increase the period of these fluctuations. 104

6.1 Perspective crystal structure renderings of (a) $\langle\bar{2}110\rangle$-oriented AlN and (b) $\langle 110\rangle$-oriented MgO. Both nearest-neighbor and second-nearest-neighbor inter-column spacings are indicated; in each case, the nearest-neighboring column is 0.6–0.7$\times$ the bond length. 109

6.2 Quantification of an experimental HAADF image. (a) Detector response map $D(\boldsymbol{k})$ acquired with 1.5 pA incident current; 68–200 mrad conditions correspond to scale bar length 200 mrad (800 nm^{-1}). (b) Radially averaged efficiency profile $\hat{D}(k)$ for 68–200 mrad collection. (c) Radially integrated fluxes for 68–200 mrad collection, where the scattered flux is attenuated by the efficiency profile to determine the detected flux. (d) Cross-correlated image of 80 nm thick AlN using a 68–200 mrad detector, both in terms of detected intensity $I(\boldsymbol{r})$ and quantitative calibrated intensity $N(\boldsymbol{r})$ ($\overline{D} = 3.10 \times 10^5$, $\xi = 0.77$), scale bar length = 0.2 nm. . 113

6.3 Quantitatively calibrated HAADF-STEM imaging of different sections of a $\langle\overline{2}110\rangle$-oriented AlN sample. Thickness was determined by PAHAADF, orientation was determined by PACBED. For images, regions are 2×2 rectangular unit cells in area, intensity is quantitatively calibrated, scale bar length is 0.2 nm. Diffraction patterns are normalized relative to the most intense region of the pattern, scale bar corresponds to 20 mrad (8 nm^{-1}). 117

6.4 Quantitatively calibrated HAADF-STEM imaging of different sections of a $\langle 110\rangle$-oriented MgO sample. Thickness was determined by PAHAADF, orientation was determined by PACBED. For images, regions are 3×2 rectangular unit cells in area, intensity is quantitatively calibrated, scale bar length is 0.2 nm. Diffraction patterns are normalized relative to the most intense region of the pattern, scale bar corresponds to 20 mrad (8 nm^{-1}). 118

6.5 HAADF-STEM image contrast for AlN and MgO in point-source conditions. (a) Variation in contrast signal as a function of depth. (b) Differences in contrast signal relative to IAM. 120

6.6 Radial profiles of the point-source electron probe, the estimated source distribution, and the finite-source probe. Including source size broadens the incident probe from a FWHM of 0.043 nm to a FWHM of 0.079 nm. 121

6.7 Comparison of quantitatively calibrated HAADF-STEM imaging of different sections of a $\langle\bar{2}110\rangle$-oriented AlN sample to corresponding simulations. Regions are 2×2 rectangular unit cells in area, scale bar length is 0.2 nm. Error bars correspond to one standard deviation of linescan-to-linescan variation. 123

6.8 Comparison of quantitatively calibrated HAADF-STEM imaging of different sections of a $\langle 110\rangle$-oriented MgO sample to corresponding simulations. Regions are 3×2 rectangular unit cells in area, scale bar length is 0.2 nm. Error bars correspond to one standard deviation of linescan-to-linescan variation. 124

A.1 Beam intensity profiles of $E_0 = 100$ keV and $\alpha_{obj} = 25$mrad aberration-free STEM probe in an isolated column of Ge with interatomic spacing 2 Å. (a) Comparison of two methods used to calculate projected atomic potentials: (i) integration along the entire z-axis with 3-D atomic potentials calculated using Hartree-Fock approximation (standard multislice approach implemented in TEMSIM) and (ii) integration along the z-axis through the slice thickness of 3-D atomic potentials calculated using Quantum Espresso code with PBE-GGA functionals. (b) Comparison of beam intensity profiles simulated with projected atomic potentials calculated using Quantum Espresso code with PBE-GGA functionals with different slicing, including sub-atomic slicing (0.5 and 0.2 Åslice thicknesses). 139

Chapter 1

Introduction

The scientific venture of imaging the natural world has a long, rich history. Observations of both the heavens and the earth progressed extensively by the unaided eye. But both made significant further advances with the development of glass lenses and mirrors that allowed magnification of objects to unprecedented new levels, enabling discovery of new planets and detailed imaging of microorganisms. However, the accompanying understanding of the wave nature of light revealed the fundamental diffraction limit to image resolution, wherein any point can be focused into a spot no smaller than the wavelength of the imaging medium. The development of "perfect" optical lenses and use of short wavelengths allows visible light imaging with resolution below 500 nm in air, but this remains far short of the atomic scale.

The rapid developments in light optics and electromagnetic theory in the nineteenth century were followed by another scientific revolution early in the twentieth century: the discovery of the paradoxical laws of quantum mechanics. Empowered by a key result of quantum theory — namely that matter, like light, simultaneously possesses both particle and wave character — scientists began to build instruments that focused free electrons to form images, and the field of electron microscopy was born. Scanning

electron microscopy (SEM) images could easily be formed by scanning a surface and collecting electrons emitted from each point. In spite of being limited to a spatial resolution on the order of 10 nm, SEM is a fast, versatile, inexpensive materials characterization tool now employed more ubiquitously than any other form of electron microscopy.

Owing to the strength of electron-matter interaction, transmission electron microscopy (TEM) required use of high-energy electrons (accelerating voltage on order of 100 kV) and thin specimens (thickness on order of 100 nm), difficult challenges rewarded by more than an order of magnitude improvement in resolution over SEM. When converged into a focused spot on the specimen, a convergent-beam electron diffraction (CBED) pattern can yield full 3D crystallographic information while simple rastering forms a scanning TEM (STEM) bright-field or dark-field image. When spread into an intense parallel beam, sharp selected-area electron diffraction (SAED) patterns yield rich surveys of structural information while complementary conventional TEM (CTEM) bright-field and dark-field images spatially map structural variation. This suite of techniques enabled direct detection of line defects, planar defects, full crystal symmetry, individual atoms, plasmon modes, and vibrational modes with unprecedented spatial resolution.

For both CTEM and STEM imaging, spatial resolution is not wavelength-limited as light microscopy is, but rather aberration-limited and point-spread-limited. Owing to the incomplete control over the magnetic field in round electromagnetic lenses, spherical aberration limits TEM resolution to above 0.1 nm; when substantial energy spreads exist in the "image-forming" lens, chromatic aberration constrains to the same resolution limit. Additional resolution degradation occurs in either mode due to point-spread effects that combine to produce broadening of at least 0.04 nm, and in historically typical operating conditions 0.1 nm or more. Yet even with all of these limitations, TEM now routinely operates at a resolution sufficient to resolve two bonded atoms from one another!

Elastic scattering from a TEM specimen yields rich quantitative information about the crystal structure of a specimen, and also serves to give qualitative information about the composition of a system via mass-thickness contrast. However, other often-critical information about the specimen — such as elemental composition, electronic structure, and collective excitation properties — remain inaccessible apart from the analysis of inelastic scattering. Inelastic scattering can be analyzed as a primary signal by means of electron-energy-loss spectroscopy (EELS), wherein transmitted electrons are separated by the amount of energy transferred to the sample. Inelastic scattering can also be characterized by means of indirect secondary signals, such as photons and electrons emitted by the sample in the course of an inelastic scattering process. Either way, the combination of inelastic scattering signals with elastic scattering greatly enriches characterization of TEM specimens, allowing studies of myriad properties of solids at atomic resolution.

In spite of the remarkable progress that has been made in pushing TEM characterization down to the atomic scale, deciphering TEM data remains as challenging as ever. The same strong electron-matter interaction that enables detection of single atoms complicates interpretation: both the propagation of the electron beam and the generation of detected signals must closely match physical reality. A century of careful experimental and theoretical work has revealed much about how the fast electrons used in TEM scatter from solids, yet this knowledge must be applied to simulate any TEM experiment that is to be interpreted conclusively. Consequently, both qualitative and quantitative interpretation have been furthered by powerful computer simulations that include both elastic and inelastic scattering.

The non-intuitive nuances of TEM data interpretation are at the heart of the studies presented here. Carefully treating the interference, propagation, and interaction localization of TEM beams using computational methods can seem needlessly tedious. Yet sometimes such involved analysis is critically necessary for coaxing out surprising information. The three-dimensional structure of a sample can be determined from SAED

patterns conventionally used to probe two-dimensional symmetry. Core orbital excitation potentials can be measured at a scale two orders of magnitude smaller than the STEM beam that imaged them. Interatomic charge transfer can be detected using imaging modes thought to simply probe the mass-thickness and orientation of the specimen. Such findings have merely flowed from patient application of computational methods to strategic problems.

- Chapter 2 introduces the instruments and methods employed in my TEM studies: electron diffraction, ADF-STEM imaging, analytical STEM spectroscopy, and multislice simulation.

- Chapter 3 discusses the use of crystal tilt series to determine thickness for atomically thin hexagonal boron nitride, molybdenum disulfide, and tungsten disulfide. It is shown that employing SAED and HAADF-STEM characterization over the course of a tilt series allows unambiguous determination of thickness for crystals up to four atomic layers thick. It is also determined that tilt-series SAED fundamentally distinguishes truly two-dimensional crystals from quasi-two-dimensional crystals.

- Chapter 4 demonstrates the use of STEM-EDX mapping to distinguish and measure core-level electron orbitals in strontium titanate. It is shown that carefully processed high-precision STEM-EDX maps reveal differences in the width of atomic columns imaged using different characteristic X-ray edges. Furthermore, the effects of finite source size and beam propagation in the crystal are deconvolved from those maps to obtain measurements of the excitation potential and impact parameter associated with each core orbital.

- Chapter 5 examines the effect of including interatomic charge transfer in multislice simulations of ADF-STEM imaging. Conventional neutral atom simulations are compared both to those modeling the atoms as fully ionized and those modeling

atomic bonding by density functional theory. It is shown that bonding affects ADF-STEM image contrast in polar crystals by altering the propagation of the electron beam through the material. The strength of the bonding effect is found to scale directly with the degree of net interatomic charge transfer, and to be robust with respect to incident probe parameters, detector geometry, and temperature.

- Chapter 6 addresses the experimental testing of the ADF-STEM bonding effects predicted by simulation. Quantitatively calibrated high-precision experimental HAADF-STEM images of aluminum nitride and magnesium oxide are directly compared to multislice simulations employing each bonding model. It is found that, in agreement with simulation, bonding significantly affects image contrast at certain thicknesses while having negligible effect at others. The limited experimental results confirm the computationally predicted effect, but also illustrate critical limitations in reproducing experimental conditions in simulation.

Chapter 2

Methods

This chapter provides basic technical background to the findings presented in the following chapters. Because transmission electron microscopy (TEM) has been the unifying theme of my investigations, both computational and experimental, it is the unifying subject of the chapter. Surveys of the principles and techniques of TEM can be found in the classic texts by Williams and Carter [1] and by Reimer and Kohl. [2]

TEM has a short but rich history that can be traced back to the demonstration of electromagnetic lensing of charged particles by Hans Busch in 1926. The first functioning electron microscope was developed by the German researchers Ernst Ruska and Max Knoll soon after, a pioneering effort that eventually earned Ruska a Nobel Prize in Physics in 1987. That first microscope had a resolution worse than an optical microscope, but advances in electron sources, high-voltage electronics, and electron optical design rapidly pushed the resolution of TEM instruments to the angstrom scale. In the present day, instruments capable of sub-angstrom resolution are routinely manufactured for uses ranging from delicate fundamental physics research to "workhorse" microelectronic device characterization.

2.1 Conventional transmission electron microscopy

In conventional TEM (CTEM), the specimen is illuminated by a collimated, highly coherent electron beam which interacts with the sample and is collected on the transmitted side using an objective lens and a system of projection lenses. This is analogous to most modes of optical microscopy, where the whole field of view is illuminated in parallel and the corresponding image or diffraction pattern can be recorded in parallel. A conventional TEM, the operation of which is shown in Figure 2.1, [2] is comprised of an electron source, a condenser system to shape the illuminating beam, an objective system to form a diffraction pattern or image, and a projection system to adjust magnification.

2.1.1 Imaging in CTEM

Passage of the central spot through the objective aperture produces bright-field CTEM imaging. Use of a small objective aperture excluding diffracted beams produces mass-thickness contrast. Inclusion of diffracted beams produces mixed mass-thickness, diffraction, and phase contrast. Bright-field CTEM is the most widely used imaging mode for qualitative high-resolution imaging of both “hard” and “soft” materials.

Exclusion of the central spot by the objective aperture produces dark-field CTEM imaging that can include both mass-thickness and diffraction contrast contributions. Selection of a diffracted spot by the objective aperture allows sensitive diffraction-contrast imaging. Dark-field CTEM is especially valuable for grain mapping and defect characterization in hard materials.

2.1.2 Diffraction in CTEM

Diffraction patterns in the STEM provide information on local crystal structure. The selected area (SA) aperture, located in the first image plane below the specimen,

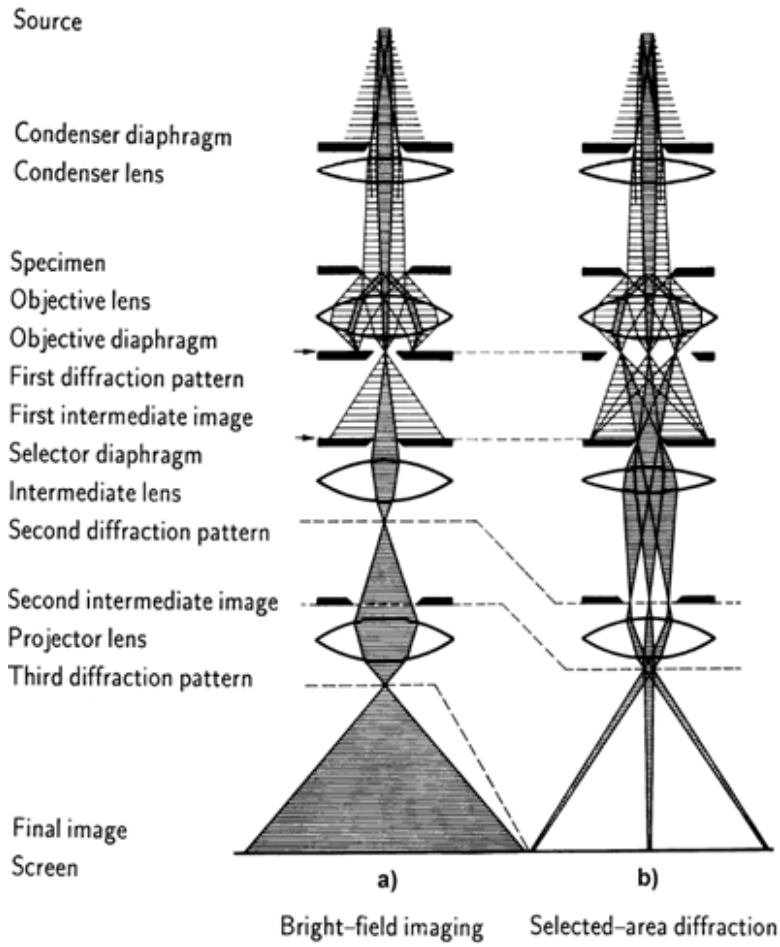

Figure 2.1: Schematics of CTEM operation in (a) bright-field image and (b) selected-area diffraction modes.

can be placed around a region of interest. The SA aperture largely excludes rays originating from regions outside the selected region, providing a diffraction pattern localized to approximately 100 nm in typical conditions. Owing to its simiplicity and similarity to X-ray diffraction, SA electron diffraction (SAED) is widely used for structural characterization of crystalline materials.

Convergent beam electron diffraction (CBED) can be employed to collect diffraction information that is more spatially localized. In CBED, the probe is converged on the sample and placed over a region of interest. Both central and diffracted spots are blurred into disks proportional to the convergence angle of the incident beam. Overlap between disks produces complex diffraction phase contrast that can be used for applications as diverse as three-dimensional structure determination, precise lattice strain measurements, and valence charge density reconstruction.

2.2 Scanning transmission electron microscopy

In scanning TEM (STEM) mode, depicted in Figure 2.2, condenser system optics focus the beam into a small, coherent probe with a half-maximum diameter on the order of one angstrom. Because the size of the incident probe serves as the lower bound on the spatial resolution of STEM, optimization of the illumination system for forming a small probe is critical. Although the image of the source is demagnified two or more times as it passes through the condenser system, starting with a bright electron source is necessary to form a small probe with substantial current (1 pA–1 nA).

In analogy to the scanning confocal optical microscopy method often used for biological imaging, images are formed serially by rastering the focused beam across the specimen, with image signals being collected independently for each point in the scan area. The most common signals analyzed include the central disk to form bright-field images, diffraction images, and electron-energy-loss spectrum images; low-angle-scattered electrons to form dark-field diffraction contrast images; high-angle-scattered electrons

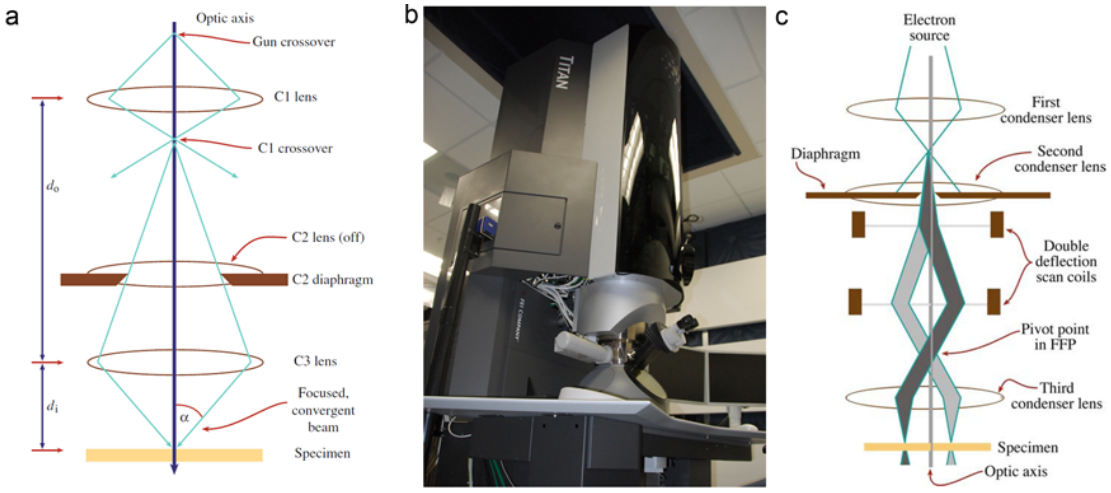

Figure 2.2: (a) Ray diagram of a (S)TEM operating as a scanning transmission electron microscope. (b) FEI Titan G2 60–300 (S)TEM at the University of Minnesota Characterization Facility. (c) Schematic of the probe scan coils of a STEM.

to form mass-thickness dark-field images; and secondary X-rays to produce X-ray spectrum images. A depiction of these and other signals generated under electron or ion illumination is illustrated below in Figure 2.3. [3]

2.2.1 Annular dark-field STEM

Annular dark-field (ADF-STEM) imaging utilizes a detector with an inner angle larger than the convergence angle, generating a dark-field image that can have both dynamical diffraction contrast and mass-thickness contrast contributions. Interpretation of ADF-STEM images is simplified by the fact that low-coherence dark-field scattering is not immune to contrast reversals except in the limit of extremely high mass-thickness. As a result, ADF-STEM images can be qualitatively interpreted without recourse to the simulations required to support most CTEM images.

If a low-angle ADF (LAADF) detector is used, then strong coherent Bragg scattering contributions enable mapping of strain, crystal orientation, and low-contrast point defects. [4, 5] High-angle ADF (HAADF) imaging utilizes a large inner angle so that

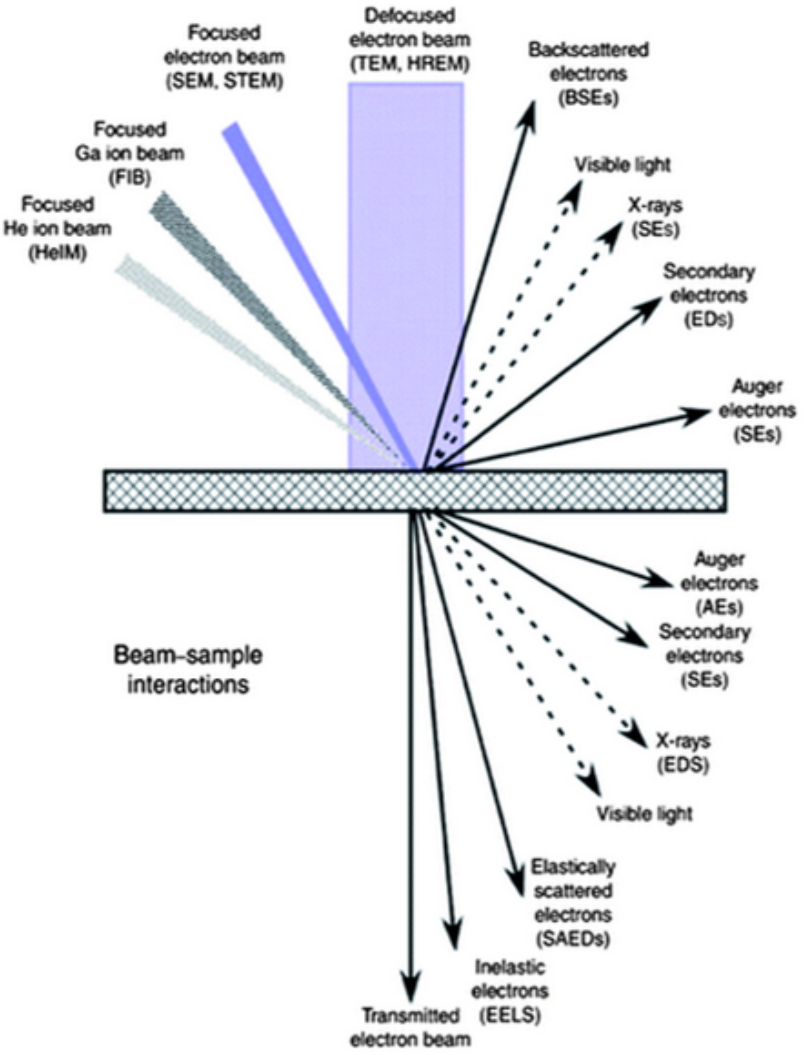

Figure 2.3: Schematic of electron-sample interaction under TEM illumination of a thin specimen.

predominantly incoherent elastic scattering is collected. The strength of Rutherford-type scattering of electrons by a screened nucleus is varies with the atomic number Z as $Z^{1.5}$–Z^2, providing "Z-contrast" imaging conditions. [6]

2.2.2 Electron energy-loss spectroscopy

As the high-energy TEM electrons pass through a specimen, they can excite various transitions in the specimen inelastically, with beam electrons losing energy equal to the difference in energies of the excited electron in its final and initial states, $\Delta E = E_f^e - E_i^e$. Electron-energy-loss spectroscopy (EELS) [7] disperses transmitted electrons with a magnetic prism which is then magnified and detected by a CCD. Inelastic collisions are strongly forward scattered, allowing ADF imaging and EELS to be performed simultaneously with high collection efficiencies [8] (Figure 2.4).

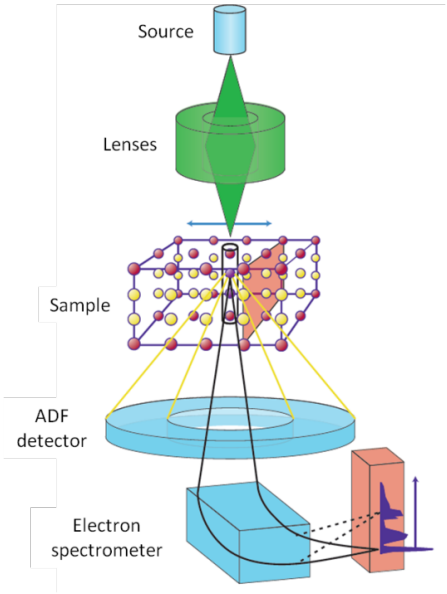

Figure 2.4: Schematic of parallel EELS and ADF imaging in STEM.

The zero loss peak (ZLP) contains primarily unscattered electrons and reflects the energy spread of the electron source. The low-loss spectrum, spanning energy losses 0–50 eV, is due to weakly bound outer-shell excitations, most prominently featuring

plasmon-loss and valence-to-conduction interband transitions. From this portion of the spectrum the local dielectric constant, band gap, and band structure can be derived, and the local thickness can be determined. [9] The core-loss spectrum, covering energy loss features above 50 eV, results from core electron excitations to available states above the Fermi level. These transitions are highly localized with energy-loss signatures that are element- and coordination-characteristic. Whereas the low-loss excitations are collective excitations of weakly-bound electrons, core-loss excitations are well-approximated by a single-electron transition in the local approximation. Coupling EEL spectra with modeling of allowed core-shell transitions can therefore identify composition and electronic structure.

2.2.3 X-ray energy-dispersive spectroscopy

Core-loss excitations ionize atoms, leaving inner-shell holes that can be relaxed by emission of Auger electrons or secondary X-rays. The energy of the electron or X-ray is characteristic of the energy level splitting of core orbitals for the ionized element, allowing elemental analysis of the imaged material. In X-ray energy-dispersive spectroscopy (XEDS), secondary X-rays are detected using reverse-biased p-i-n detectors, with high-speed signal processing electronics allowing efficient parallel detection of X-rays of energies up to 40 keV. As with EELS, XEDS can be performed position-by-position in parallel with ADF imaging. An example of XEDS spectrum imaging is shown in Figure 2.5.

2.3 Transmission electron microscope resolution

Understanding of the wave nature of of electrons revealed the fundamental diffraction limit to image resolution: waves with wavelength λ collected by an aperture subtending

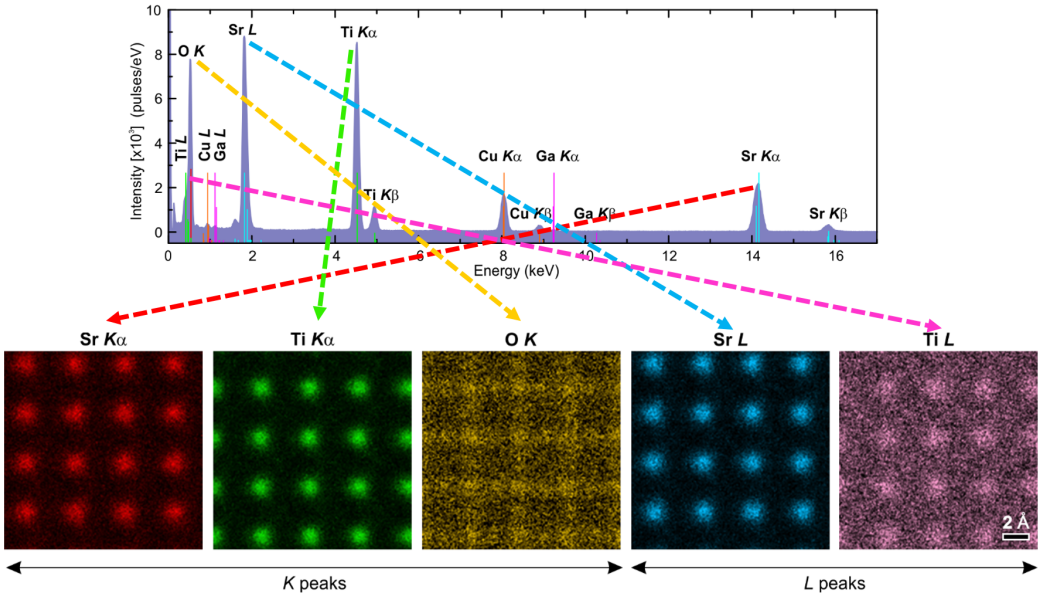

Figure 2.5: Example of different XEDS spectrum images of ⟨001⟩-oriented STO formed using each of five distinct characteristic X-ray peaks.

semi-angle α broaden a point in the object into a disk with half-maximum diameter d.

$$d = \frac{\lambda}{2sin\,(\alpha)} \approx 0.5\lambda/\alpha \tag{2.1}$$

Because two points separated by any smaller distance do not form two distinguishable maxima, for an optical system with wavelength λ and acceptance semi-angle α, the smallest spacing that can be resolved is approximately that diameter. For the high-energy relativistic electrons of a TEM, with wavelengths of 2–5 pm, this results in theoretically achievable resolution of less than 10 pm.

The inability of round electromagnetic lenses to focus rays of different axial positions to the same point causes a point object to be imaged as a disk of finite size, an effect known as spherical aberration that severely degrades resolution for large acceptance angles. Assuming optimal selection of acceptance semi-angle α, the practical achievable

resolution is then

$$d_{min} \approx 0.45 \left(C_s \lambda^3\right)^{1/4}. \tag{2.2}$$

In traditional electron microscopes, which exhibit significant spherical aberration, an optimal resolution of 150 pm or worse is obtained at a convergence angle of approximately 10 mrad.

The resolution of TEM has significantly improved in the last twenty years thanks to the development of spherical aberration correctors. In 1947 the use of multipole lenses to cancel the spherical aberration intrinsic to round lenses, was first proposed by Otto Scherzer. [10] It was not until the late 1990s, though, that electronics and signal processing had advanced to the point that the numerous lenses and correction algorithms could be integrated into a commercial instrument. Elegant proofs of concept [11, 12] have been followed by widespread commercial manufacture of correctors that allow diffraction-limited imaging out to convergence angles of 30 mrad and larger. As a result, subangstrom resolution is now routine, with resolution below 50 pm having been demonstrated in both CTEM and STEM imaging. An example of the effect of aberration-correction on HAADF-STEM resolution is presented in Figure 2.6 below.

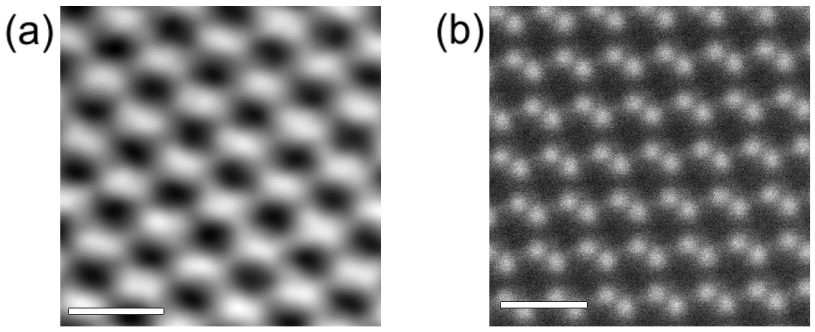

Figure 2.6: Comparison of HAADF-STEM imaging of ⟨110⟩-oriented Si using (a) an uncorrected TEM and (b) an aberration-corrected TEM. Scale bars are 0.5 nm in length, and the separation between nearest-neighboring columns is 0.136 nm.

2.4 Transmission electron microscopy simulation

Owing to the strong, complex interactions of electrons with matter, correct interpretation of TEM experiments often requires comparison to physically accurate simulations. While Bloch wave and single-electron Monte Carlo methods are sometimes used to model beam-specimen interaction, it is the multislice method [13] that has proven itself most robust for TEM simulation.

2.4.1 Multislice method

Multislice simulation treats the incident electron beam as a superposition of plane wave components (i.e., a "wavepacket"). A specimen of arbitrary structure is sectioned into many discrete "slices." At each slice, the projected atomic potentials of all atoms in the slice are superimposed to form a scattering potential. The scattering of the beam from the slice is then calculated in the weak-phase approximation followed by propagation of the beam to the next slice calculated as near-field diffraction. This algorithm can be efficiently implemented using fast Fourier transform operations, calculating scattering in real-space and propagation in reciprocal-space. Calculation of the beam interaction through the full thickness of the specimen simply proceeds iteratively slice-by-slice. This process is illustrated in Figure 2.7 below.

2.4.2 Simulating imaging and diffraction

CTEM images are calculated by taking the exit wavepacket, masking it by the objective aperture, calculating the phase shifts of each component by the aberration function of the objective lens, and then computing the square-modulus of the post-objective wavepacket in real-space. Diffraction patterns are calculated simply by computing the square-modulus of the exit wavepacket in reciprocal-space. STEM images are calculated by summing the section of the diffraction pattern falling on the detector, with the resultant intensity for each probe position being used to serially build up the image.

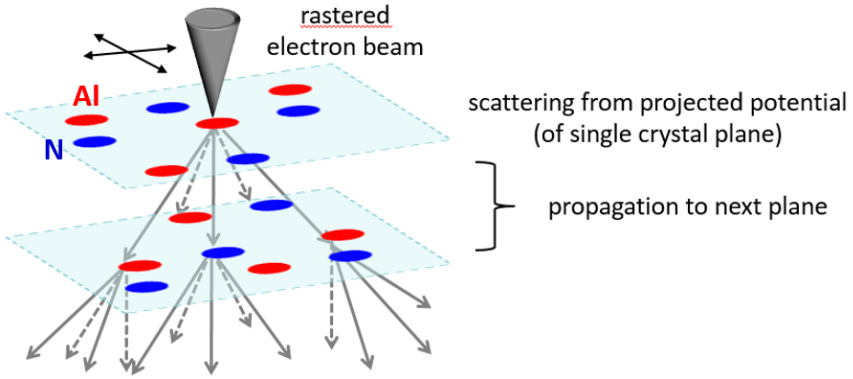

Figure 2.7: Schematic of multislice TEM simulation showing the scattering and propagation of a STEM probe through an AlN crystal.

2.5 Transmission electron microscopy resources at the University of Minnesota

The studies presented in this thesis depended critically upon shared user facilities for their completion. The valuable capabilities utilized are summarized below.

2.5.1 Characterization Facility

The University of Minnesota Characterization Facility FEI Titan G2 60–300 (S)TEM is equipped with a high-brightness X-FEG source, Wien monochromator, and 5th-order DCOR probe corrector. Detectors include a CCD camera, a BF-STEM detector, three ADF-STEM detectors, a large-solid-angle SuperX XEDS detector, and a Gatan Enfinium ER EELS spectrometer. The microscope is capable of operating at 60, 80, 200, and 300 keV, with a best demonstrated spatial resolution of ~60 pm at 300 keV.

The monochromator system integrated into the gun allows control over beam current without changing convergence angle or defocus, allowing sweeping of beam current over 10 pA–1 nA. The CEOS DCOR probe aberration corrector, capable of measuring and correcting aberrations up to 5th order, allows approximately diffraction-limited imaging with convergence semi-angles of 30 mrad or greater. When imaging with a low beam

current, quantitative high-resolution ADF-STEM imaging can be performed with the smallest-sized, slowest-damaging electron probes. When imaging with a high beam current, advanced EELS and XEDS detectors allow rapid, clear atomic-scale measurement of the composition and electronic structure of materials that complements ADF-STEM structural imaging.

2.5.2 Minnesota Supercomputing Institute

The Minnesota Supercomputing Institute provides a thoroughly supported UNIX platform for scientific computation. Resources include Itasca (1091 8-core CPU nodes with 24 GB of memory each) and Mesabi (616 24-core CPU nodes with 64 GB of memory each, 40 24-core GPU nodes with 128 GB of memory each), as well as hundreds of older CPU nodes available for small calculations.

Compilation of the TEMSIM [14] multislice suite, a family of open-source programs developed and maintained by Earl Kirkland of Cornell University, is readily done on MSI using optimized C compilers with support for the multithreading schemes OpenMP and OpenACC. These programs can be compiled both for interactive use as well as systematic batch scripting. Furthermore, the TEMSIM source could be modified to develop new functionality: parallelized STEM image simulation using exact projected potentials, parallelized STEM image simulation using custom-parameterized potentials, simulation of scattering with sub-atomic slicing, and full three-dimensional profiling of simulated beam intensity within a specimen.

Chapter 3

Measuring thicknesses of atomically thin layered crystals

Studies of hexagonal boron nitride are adapted with permission from Odlyzko and Mkhoyan, "Identifying hexagonal boron nitride monolayers by transmission electron microscopy" *Microscopy and Microanalysis* **18**, 558-567 (2012), copyright 2012 Cambridge University Press. Studies of molybdenum disulfide and tungsten disulfide are adapted with permission from Wu, Odlyzko, and Mkhoyan, "Determining the thickness of atomically thin MoS_2 and WS_2 in the TEM" *Ultramicroscopy* **147**, 8-20 (2014), copyright 2014 Elsevier.

3.1 Introduction

Two-dimensional (2D) materials [15] have been the subject of an immense research effort in recent years. Since the isolation of graphene and recognition of its potential [16], the scientific community has actively studied these atomically thin materials for applications in electronics, mechanics, and optics [17, 18]. Due to their structure of covalently bonded planes bound by comparatively weak interplanar attractions, layered materials such as graphite and hexagonal boron nitride (h-BN) are among a small

handful of materials that can form stable 2D sheet and tube structures, making them important platforms for novel condensed matter physics. And because of the exceptional electronic properties and potential for chemical functionalization associated with 2D materials, atomically thin graphite [19, 20] and h-BN [21, 22] both show promise for use in chemically sensitive devices and next-generation electronics.

Transition metal dichalcogenides (TMDs) [23] with formula MX_2, where M is a transition metal and X is a chalcogen, form a unique class of layered materials distinct from that of graphite and h-BN. Although the strong intraplanar covalent bonds coupled with weak interlayer van der Waals interactions that are characteristic of other 2D materials still persist, stable monolayers of TMDs do not exist as single atomic planes but as triplanar XMX stacked structures. This structural arrangement produces distinctive behavior in TMD monolayers, such as a band structure ranging from semiconducting for MoS_2 [24] and WS_2 [25] to metallic for $NbSe_2$ and $TaSe_2$. [26] This diversity opens a host of applications for TMDs and shows their promise as building blocks for future devices.

Numerous characterization methods [27–29] have been used to study the structure and properties of 2D materials. The TEM, in particular, has proven to be an excellent tool for characterizing nano- and sub-nano-sized samples. Scanning TEM (STEM), bright-field conventional TEM (BF-CTEM) and selected area electron diffraction (SAED) have been powerfully combined to study atomic structure [30–33], grain boundaries [34,35], point defects [36], edge reconstructions [37,38], and susceptibility to electron beam damage [39]. Many TEM studies of TMDs are supplemented by atomic force microscopy (AFM) to provide direct thickness measurements. However, the low throughput of AFM, potentially small lateral size of TMD flakes and the challenges of transferring the samples onto a TEM grid make direct TEM-based determination of specimen thickness highly desirable.

Meaningful TEM studies of 2D materials require reliable determination of sample thickness in the TEM, especially in distinguishing single sheets from thicker regions.

SAED [30,33,40], through-focal BF-CTEM imaging [31,41], on-axis ADF-STEM image intensities [32,42], and low-loss EELS [40,43] have all been experimentally demonstrated as methods for identifying monolayers of 2D materials. This study systematically analyzes the reliability of SAED and ADF-STEM imaging in determining the thicknesses of certain 2D materials (h-BN, MoS2, and WS_2 are considered, including all known polymorphs) up to four atomic layers thick through simulated TEM images and diffraction patterns. The effects of tilt off of the [0001] zone axis on ADF-STEM images and SAED patterns are examined in order to determine suitable methods for measuring thickness for freestanding samples of these 2D materials in the TEM.

3.2 Methods

ADF-STEM images and SAED patterns of were simulated using the multislice method [13] implemented with the code developed by Kirkland. [14] For all crystals, a tilt series beginning at the [0001] zone axis was simulated in steps of 10 mrad or larger, up to 500 mrad (around 30°) off-axis. The effects of crystal tilting were accounted for by tilting [0001]-oriented supercells using a rotation matrix applied to the original atomic coordinates.

All three materials exhibit layered hexagonal crystal structures: h-BN has lattice parameters $a = 0.250$ nm and $c = 0.666$ nm, MoS2 and WS_2 share lattice parameters $a = 0.317$ nm and $c = 0.614$ nm. For h-BN, sppecimen tilts are referenced to two families of high-symmetry directions in the lattice, as illustrated in Figure 3.1, x-tilts are defined as tilts about the y-axis (a $\langle 10\bar{1}0 \rangle$ direction) while y-tilts are defined as tilts about the orthogonal x-axis (a $\langle 11\bar{2}0 \rangle$ direction). Any arbitrary tilt off of the [0001] zone axis can be constructed as a superposition of tilts in these two directions.

The atomic structures of 2H and 1T MoS2/WS_2 are shown in Figure 3.2 along with the tilting conventions. The x- and y-tilts were performed as rotations around the y- and x-axis, respectively, or around the $[\bar{1}2\bar{1}0]$ and $[10\bar{1}0]$ directions in a hexagonal

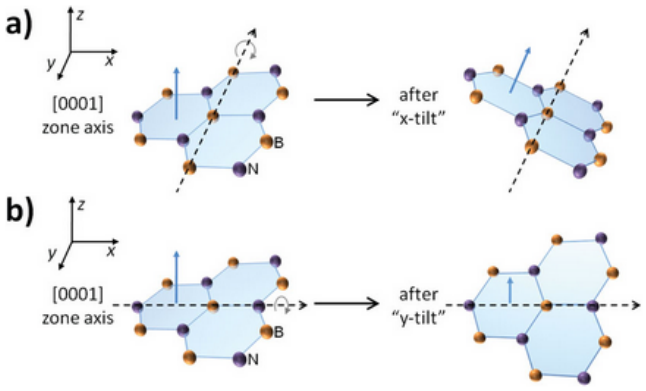

Figure 3.1: Tilt axis conventions; in each case, the blue vector indicates the [0001] zone axis. (a) Schematic illustrating an x-tilt performed on a h-BN monolayer. (b) Schematic illustrating a y-tilt performed on a h-BN monolayer.

lattice, respectively. As with h-BN, any arbitrary tilt direction can be represented as a superposition of tilts about these two axes.

Simulations of h-BN were performed for a beam energy of 100 keV, and those for MoS_2 and WS_2 were performed for a beam energy of 200 keV; these conditions corresponded to acceptable rates of beam damage observed in experiments. [33, 44, 45] Slice thickness was adaptively set as $c \times cos\left(\theta_t\right)/8$, where θ_t represents the tilt angle, to maintain a similar number of atoms in each slice and to preserve the real z-direction periodicity of the atoms throughout the tilt series. A high-angle ADF detector collected electrons scattered 54–340 mrad off of the optic axis to form the image. Effects of thermal displacements were simulated by averaging 10 frozen phonons configurations at 300 K for each image (additional simulations showed that higher phonon configurations affected negligibly the ADF-STEM image considered here). The in-plane root mean square (RMS) thermal displacement values for B and N atoms in h-BN were scaled from those of graphite [46] as 11.0 and 9.6 pm, respectively. Those used for TMD crystal simulations were 7.1 pm for S atoms and 4.5 pm for Mo atoms; [47] a displacement amplitude of 2.3 pm was estimated for W atoms (as scaled from Mo according to the ratio of their atomic masses).

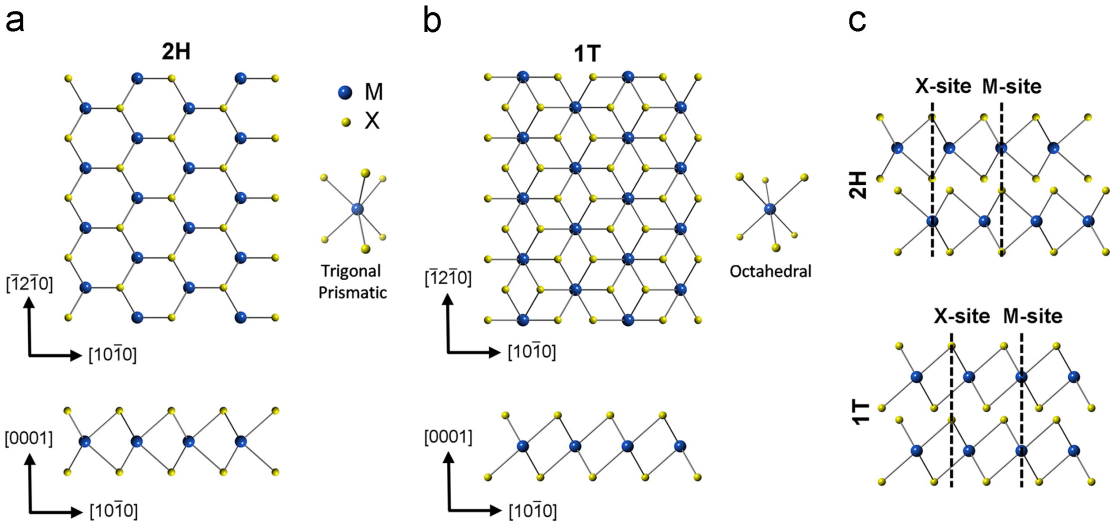

Figure 3.2: Structural models of single layer 2H and 1T MX_2 crystals, where M is a Mo or W site and X is a S site, and tilt conventions. (a): 2H MX_2 structure; (top) [0001] view and (bottom) $[\bar{1}2\bar{1}0]$ view. (b): 1T MX_2 structure; (top) [0001] view and (bottom) $[\bar{1}2\bar{1}0]$ view. X-tilt corresponds to a rotation around the $[\bar{1}2\bar{1}0]$ axis and y -tilt corresponds to a rotation around the $[10\bar{1}0]$ axis. (c) Illustration of the stacking of 2H and 1T MX_2 layers using the M- and X-site convention.

ADF-STEM image simulations were performed using aberration-corrected probes, employing supercells close to 3×3 nm^2 in size, using transmission and probe functions calculated at 1024×1024 pixelation. Probe parameters for h-BN were set as C_3 = 15 µm, C_5 = 10 mm, df = 3.0 nm, and α = 25 mrad, while those used for the TMD material simulations were C_3 = 40 µm, C_5 = 5 mm, df = 3.5 nm, and α = 20 mrad. These parameters were selected to reflect realistic probe characteristics at these electron beam energy, but without explicitly taking into account a finite source size or chromatic aberration of the microscope. The simulated beams each exhibited a FWHM of about 0.9 Å, which is comparable to resolution observed in experiments performed at these energies. [48]

SAED pattern simulations were performed employing supercells close to 25×25 nm^2 in size, using a slightly converged (2.0 mrad convergence for h-BN, 1.5 mrad for MoS_2 and WS_2) beam to improve pattern visibility. Both transmission and probe functions were calculated at 2048×2048 pixelation. Thermal vibration effects were neglected in these calculations since phonons only weakly dampen diffraction spots at 300 K for atomic vibrations with RMS values of 0.01 nm and smaller. [49] All SAED patterns are presented as being normalized to the most intense diffraction spot (saturating the central beam) and using linear intensity scaling in each individual pattern.

3.3 ADF-STEM imaging

3.3.1 Zone axis orientation

h-BN thickness determination

For h-BN samples aligned to the [0001] zone axis, there are quantitative differences in column contrast between samples one, two, three, and four layers thick (Figure 3.3). Columns with odd numbers of atoms have asymmetric ADF scattering intensities (column-to-column peak intensities differ by 40% and 15% for one and three

layers, respectively) while columns with even numbers of atoms have symmetric ADF scattering intensities.

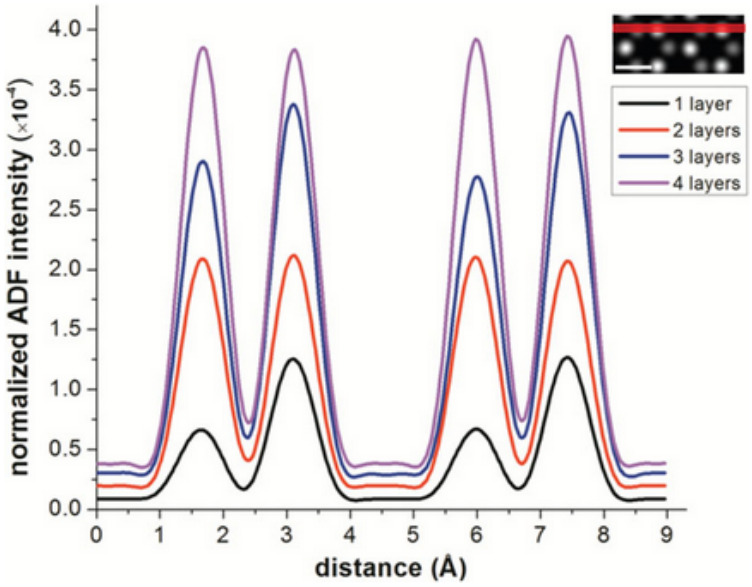

Figure 3.3: Line scans for [0001]-oriented samples of h-BN along a $[11\bar{2}0]$ direction; the red stripe indicates the six-pixel band of the image for which line scans were performed. ADF detector intensity, normalized to the incident beam current, is plotted on a linear scale.

The ADF-STEM simulation data presented above show that, in principle, different thicknesses of h-BN can be distinguished from one another using line scans on raw data and taking the ratio of peak column intensities. Due to the strong Z-dependence of high-angle, incoherent elastic scattering, only columns with equal numbers of B and N atoms will have equal intensities. In experiments, however, image noisiness and beam nonidealities may render it impractical to determine the thickness of different regions from relative column intensities, especially from raw unprocessed data. In the case of imaging with SNR improved by cross-correlation and detector response quantitatively calibrated relative to incident beam current, distinction between different thicknesses at zone axis is possible.

TMD phase determination

For TMD crystals at the exact [0001] zone axis (0 mrad tilt), two sites with distinct intensities can be identified: the M-site corresponds to a position where the incident beam contacts a M atom first, and the X-site to a position where the incident beam contacts a X atom first (recall Figure 3.2). Figure 3.4 shows the ADF intensity ratios of the peak intensity at the X-site to that at the M-site for each thickness. Despite the simulated beam having passed through the same number of M and X atoms at each site in even-layered samples, ADF intensity varies column-to-column, which differentiates the case of 2H MoS_2/WS_2 from that of h-BN. The X/M intensity ratio at the monolayer is smaller for WS_2 than MoS_2, which is expected from the atomic number (Z) dependence of incoherent high-angle scattering.

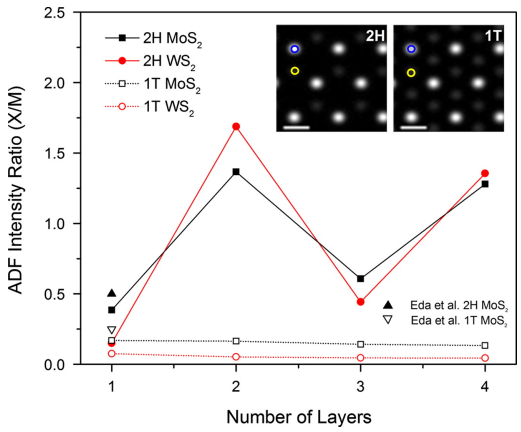

Figure 3.4: ADF-STEM intensity ratios of X-site to M-site at [0001] zone axis for 1–4 layers of 2H MX_2 and 1T MX_2. Yellow dots represent the X-site and blue dots the M-site. 2H configuration alternates the higher intensity site as a result of the ABA-BAB stacking, whereas in 1T configuration with ABA-ABA stacking it remains constant (see also Figure 3.2(c)). For comparison, experimental ADF-STEM image intensity ratios for 2H and 1T MoS_2 monolayers from Eda et al. are also shown.

The ADF-STEM simulations show distinct differences between the 2H and 1T MoS_2 images, as expected from their different atomic arrangements. These simulated images are consistent with the experimental findings of Eda et al. [50], identifying 2H MoS_2

monolayers at [0001] zone axis as a honeycomb populated by visible M- and X-sites and 1T MoS_2 monolayers as a larger hexagonal structure of M-sites surrounded by undetectable X-sites. The ADF intensity from a X-site in a 1T crystal is less than half that in a 2H crystal because the 1T polymorph does not contain pairs of S atoms vertically aligned at the [0001] zone axis Figure 3.2, leading to decreases in high-angle scattering. The results show that this distinction holds for all thicknesses of MoS_2. However, the intensity ratios of X- to M-sites in 1T at [0001] (see Figure 3.5) show that the X-site still displays 17% of the intensity of the M-site in MoS_2. Although noise in experimental ADF-STEM images may render the X-site undetectable, accurately processed images should in principle show the X-site since ADF scattering intensity from a single atom is detectable even for light atoms such as B, C, and N, and varies as $Z^{1.5}$–$Z^{1.7}$. [32, 51].

Although the same trends are observed for WS_2, X-site/M-site, ADF intensity ratios for 2H and 1T WS_2 monolayers are smaller in magnitude as ADF scattering from W ($Z = 74$) is far stronger than from Mo ($Z = 42$). For monolayers, the absolute difference between the ratios for the two polymorphs for WS_2 is less than 0.08 (or 8%) while for MoS_2 they differ by more than 0.2 (or 20%) (see Figure 3.4). Thus, WS_2 monolayer polymorphs cannot be easily distinguished (using a conservative distinguishing criteria of greater than 10%) with evaluation of the X-site/M-site ADF intensity ratios from images recorded at [0001] zone axis; the W atoms will be clearly visible while the S atoms will be nearly undetectable in either case. However, for 2 or more layers, 2H and 1T polymorphs of WS_2 can be distinguished. In the 2H polymorph, more comparable M-site and X-site ADF intensities are expected due to the additional W atoms in each atomic site.

In summary, for all thicknesses other than WS_2 monolayer, the high-intensity spots in the 2H polymorph are 0.18 nm apart while in the 1T they are 0.32 nm apart, a distinction easily observed in aberration-corrected STEMs.

TMD thickness determination

A notable observation of the ADF-STEM imaging results for all the studied materials, except the 2H WS_2 monolayer, is that the layer count in practice cannot be unambiguously determined from image contrast at the [0001] zone axis alone. In the 2H polymorph the monolayer displays a lower X-site/M-site ADF intensity ratio than the multilayers (see Figure 3.4), but since the brightest atomic column switches from M-site to X-site with odd and even number of layers, the distinction between thicknesses could still be ambiguous without additional support. This is in stark contrast to h-BN, where column-to-column intensity ratios can in principle be used to distinguish odd- and even-numbered layers. [32].

The X-site/M-site ADF intensity ratios shown also indicate that in even-numbered layers there are appreciable intensity asymmetries between the M- and X-sites despite the identical compositions for all atomic columns. This phenomenon can be attributed to beam channeling [52, 53]. As the beam propagates through the thin sample, each scattering center (atom) further focuses the beam. Since the high-angle scattering intensity from an atom depends on both its Z number and the incident beam intensity distribution, the X-site, where the beam contacts the X atom first, shows higher intensity as the M atom further in the z-direction scatters a more focused (or intense) beam than the M atom above it at an adjacent M-site. Odd-numbered layers always have higher M-site intensity because they contain more M atoms. The 1T configurations do not display this behavior because M- and X-sites contain only their respective atoms in an atomic column at [0001] zone axis regardless of thickness. Instead, 1T layers display a weakly decreasing X-site/M-site ratio with increasing thickness. Extrapolating the trends of Figure 3.5, it is expected at the bulk limit that M- and X-sites in 2H will be indistinguishable (X-site/M-site$\approx$1) while 1T will only display the M site (X-site/M-site$\ll$1).

Although relative intensities can be used for determining the number of layers of uniform sheets, situations may occur where an imaged area contains a step change in thickness. Because ADF intensity is sensitive to the atomic Z-number and the total number of atoms present in an atomic column, absolute intensities can be used to determine thickness provided that the ADF detector has been calibrated to measure the scattered electron current. [54, 55] Figure 3.5 shows ADF line intensity profiles for 2H and 1T MoS_2 and WS_2 samples simulated at [0001] zone axis. The intensities of both the M- and X-sites increase with thickness as additional atoms are added to each column. The different intensity jumps associated with adding an atom to the column at different depths can be attributed to beam channeling, as discussed in the previous section. Taking the highest intensity site as a reference, for both 2H and 1T polymorphs the number of layers can be discerned at least up to 4 layers. For example, for 2H MoS_2, the ADF intensity of the brighter site (which oscillates from M- to X-site and from X- to M-site with each additional layer) is: 0.01, 0.02, 0.03, and 0.05 for 1 to 4 layers respectively. This increase is roughly consistent with reported experimental results. [56] The intensity increase is greater for 2H WS_2: 0.02, 0.04, 0.08, and 0.11 for 1 to 4 layers. The 1T polymorph, which keeps a constant high intensity M-site at any thickness, experiences larger increases in intensity with increase of number of layers than the corresponding 2H materials. This thickness dependence of peak intensity would allow thickness determination as long as the ADF signal can be accurately quantified.

3.3.2 Tilt series

h-BN thickness determination

Tilt effects for ADF-STEM imaging of few-layer h-BN were examined for a 0–500 mrad range for each x-tilt (Figure 3.6) and y-tilt (Figure 3.7). For a one-layer-thick

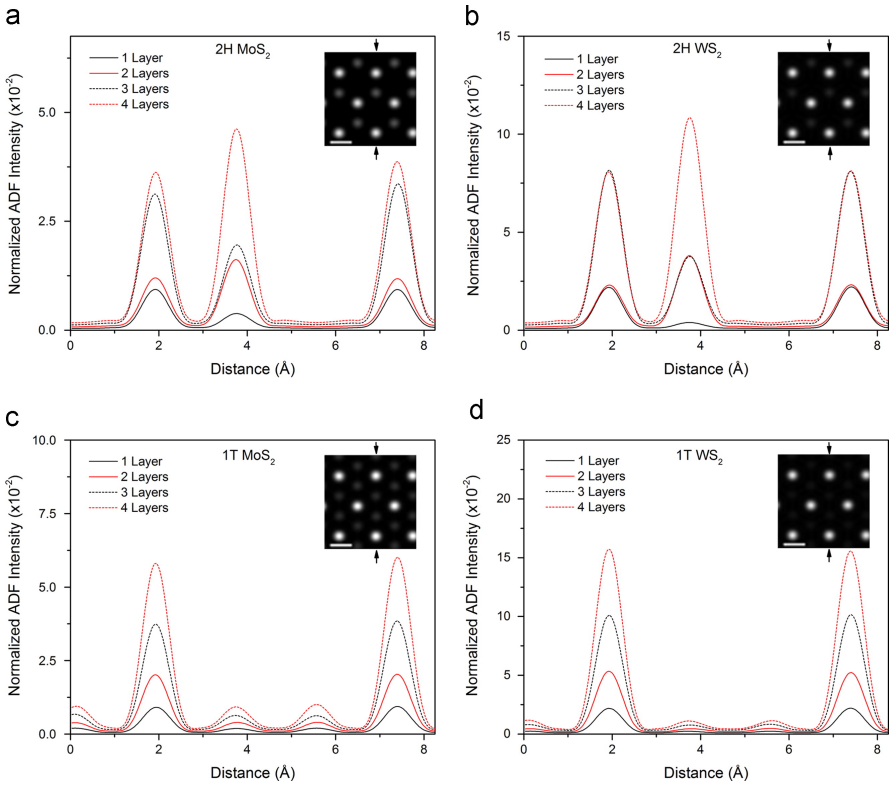

Figure 3.5: Simulated ADF-STEM intensity linescans at [0001] zone axis: (a) 2H MoS_2; (b) 2H-WS_2; (c) 1T MoS_2; (d) 1T WS_2. Each line profile is averaged over a strip 12 pixels (or 0.04 nm) wide. The insets are corresponding ADF-STEM images with arrows indicating directions of linescans. Intensities are normalized to the incident beam current.

sample, tilt only serves to produce a slightly distorted projection of the honeycomb-structured layer; for multiple-layer samples, tilting introduces distinctive complex streaking distortions to the images, with the tilt series for each thickness being clearly distinctive from the others. In all cases, as expected, distortions occur in the direction perpendicular to the tilt axis.

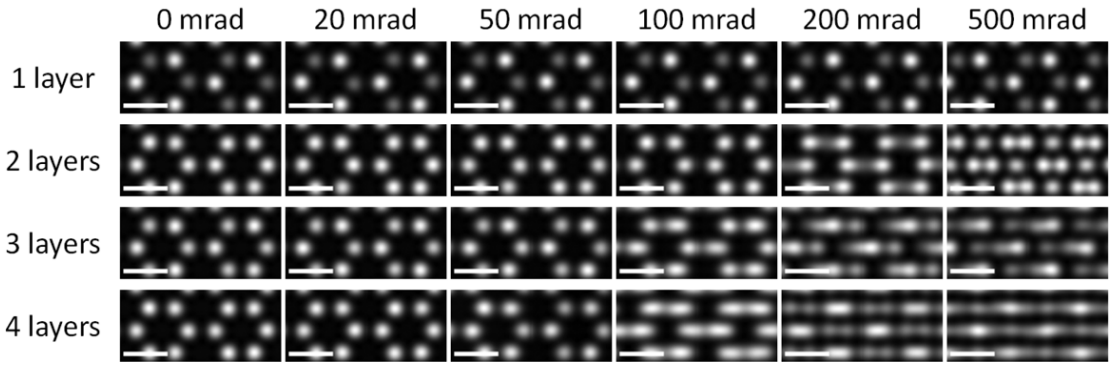

Figure 3.6: Series of simulated ADF-STEM images of atomically thin h-BN for an aberration-corrected 100 keV TEM, x-tilts. For a one-layer-thick region, tilt only serves to produce a distorted projection of the honeycomb-structured layer; for multiple-layer regions, tilting introduces distinctive complex distortions to the images, visible as streaking perpendicular to the y-axis. Linear intensity scale; scale bar = 0.2 nm.

ADF-STEM imaging over a tilt series permits unambiguous distinction of a single sheet from multilayered samples, and of multilayered samples of different thicknesses, by observing changes in ADF-STEM image contrast over a tilt series. Only a single sheet will not have image contrast change with tilts away from the [0001] zone axis, permitting straightforward identification of freestanding h-BN monolayers. Also, tilting through the 100–500 mrad range would permit distinction between sheets two, three, and four atomic layers thick based on distinctive differences in image contrast between the layers in this tilt range (although possibly only by post-processing of a series of several images acquired at different tilts). Though experimental implementation may be complicated by hysteretic drift of the stage over a tilt series and by the small depth-of-focus of an aberration-corrected STEM instrument, these results should lend themselves

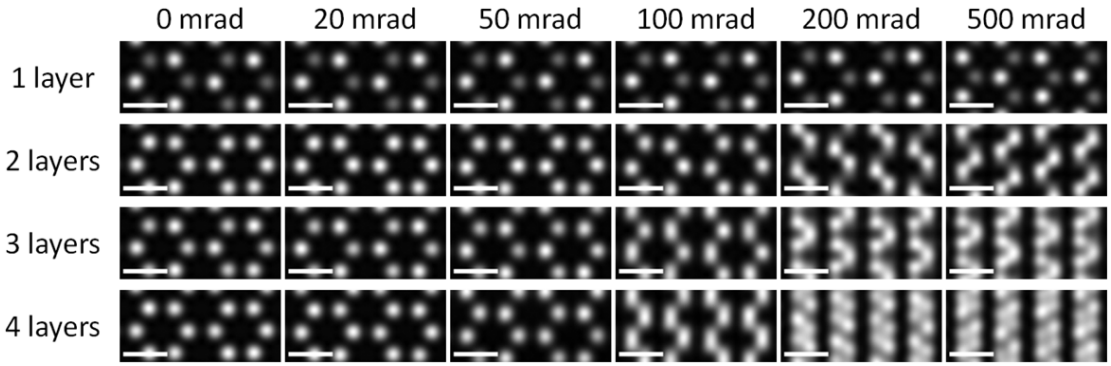

Figure 3.7: Series of simulated ADF-STEM images of atomically thin h-BN for an aberration-corrected 100 keV TEM, y-tilts. For a one-layer-thick region, tilt only serves to produce a distorted projection of the honeycomb-structured layer; for multiple-layer regions, tilting introduces distinctive complex distortions to the images, visible as streaking perpendicular to the y-axis. Linear intensity scale; scale bar = 0.2 nm.

to determining sample thickness of few-layer h-BN in aberration-corrected STEM studies (such as the study of defects and edges in atomically thin h-BN).

TMD thickness determination

The ADF-STEM image tilt series for 1 to 4 layers of 2H MoS_2 and 2H WS_2 are shown in Figure 3.8 and Figure 3.9, respectively. While the image contrast of monolayers is essentially independent of crystal tilt, tilting multilayers beyond 50 mrad (~3°) in either direction creates distortions in the direction perpendicular to the tilt axis; these distorted patterns are easily distinguishable.

Figure 3.10 and Figure 3.11 contain the simulated ADF-STEM images for 1T MoS_2 and 1T WS_2, respectively. Tilt effects in either direction begin to be distinguishable at 50 to 100 mrad, especially for the higher intensity M-sites. Additional tilt leads to complex effects such as M- and X-site overlaps for 24 layers, similar to the 2H configuration.

Using the contrast variation of ADF-STEM images, it may be possible to identify the layer count by observing tilt-series trends during an experiment. For example, for the

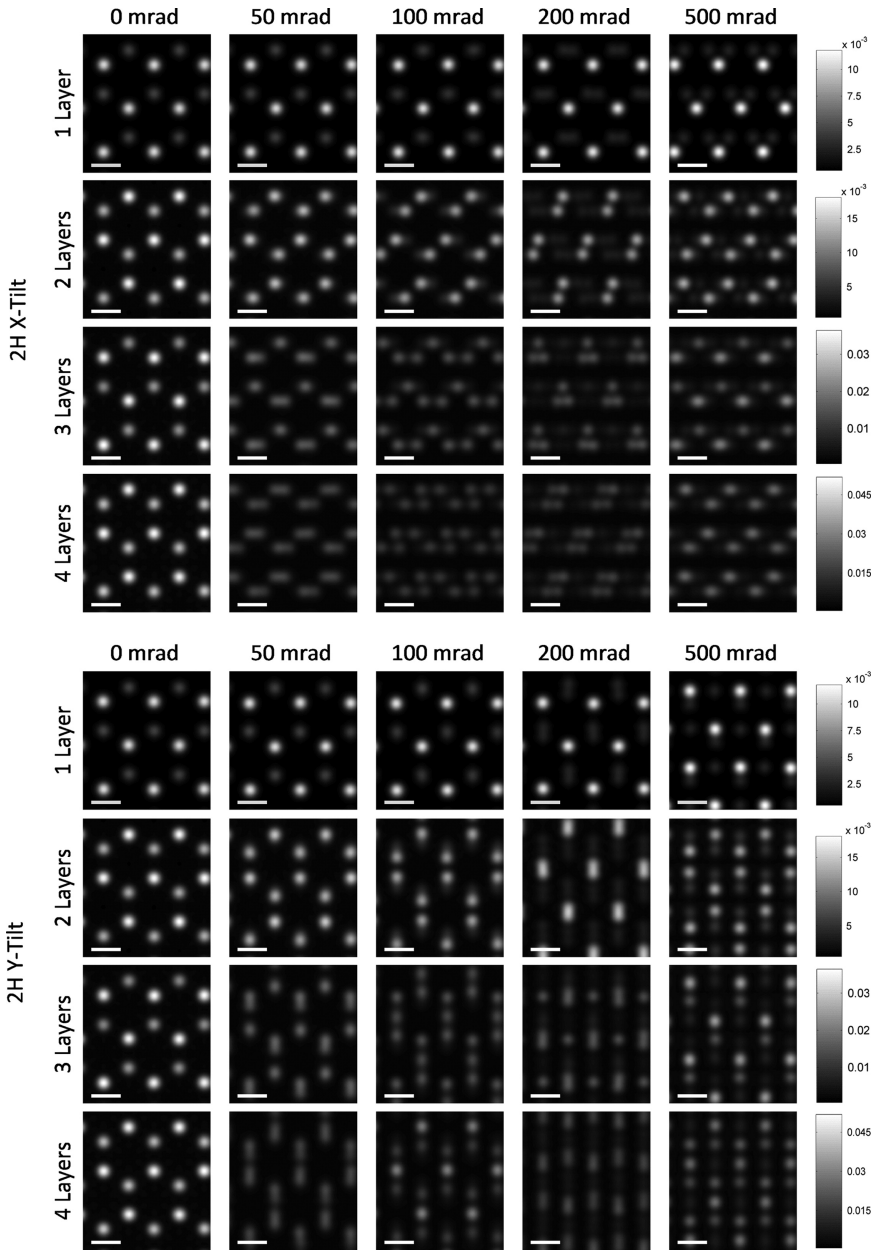

Figure 3.8: Simulated ADF-STEM images of 2H MoS_2 at various x- and y-tilt angles. Both tilt directions produce unique intensity patterns at all thicknesses as a result of overlapping of Mo and S atoms. Color bars are scaled to each row with intensities normalized to the incident beam; scale bars = 0.18 nm.

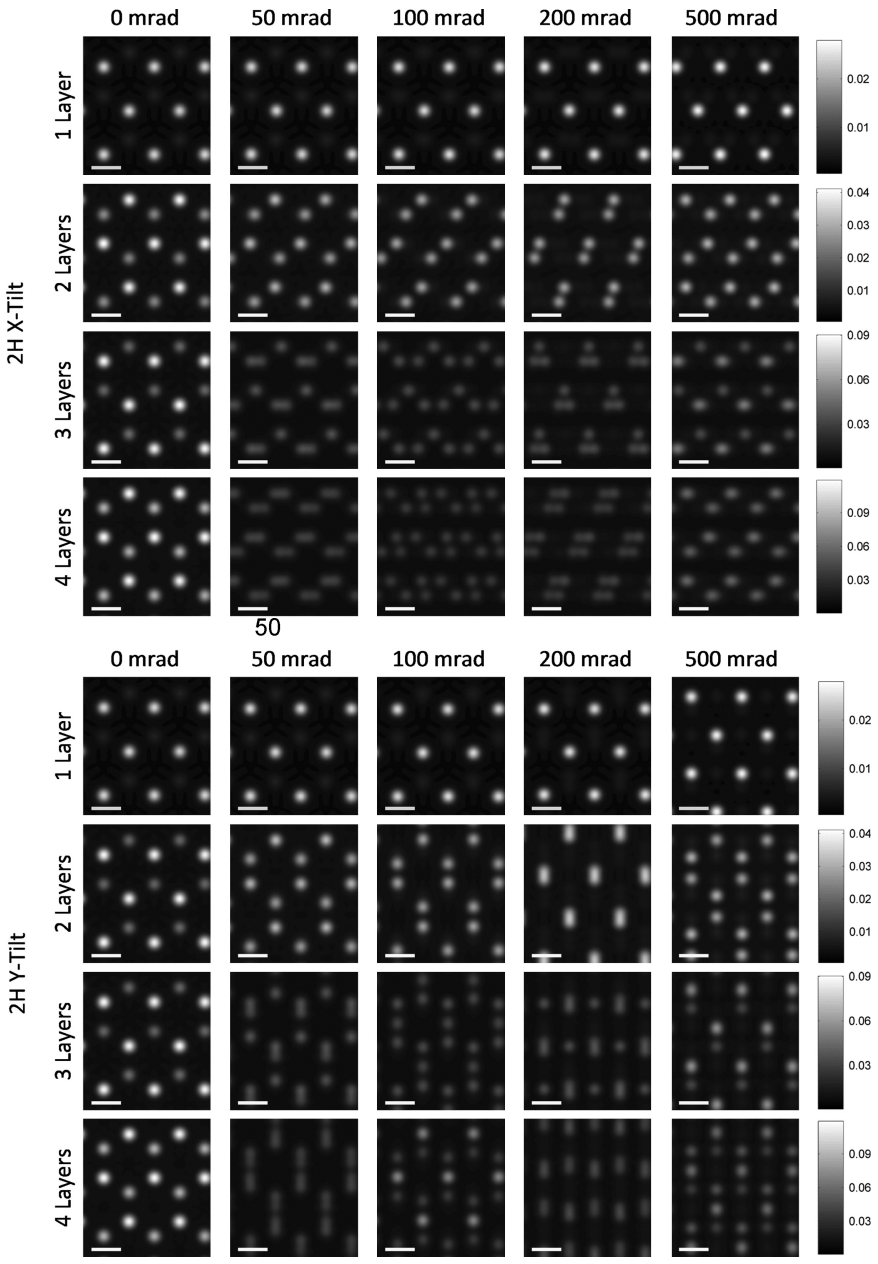

Figure 3.9: Simulated ADF-STEM images of 2H WS_2 at various x- and y-tilt angles. Both tilt directions produce unique intensity patterns at all thicknesses as a result of overlapping of W and S atoms. Color bars are scaled to each row with intensities normalized to the incident beam; scale bars = 0.18 nm.

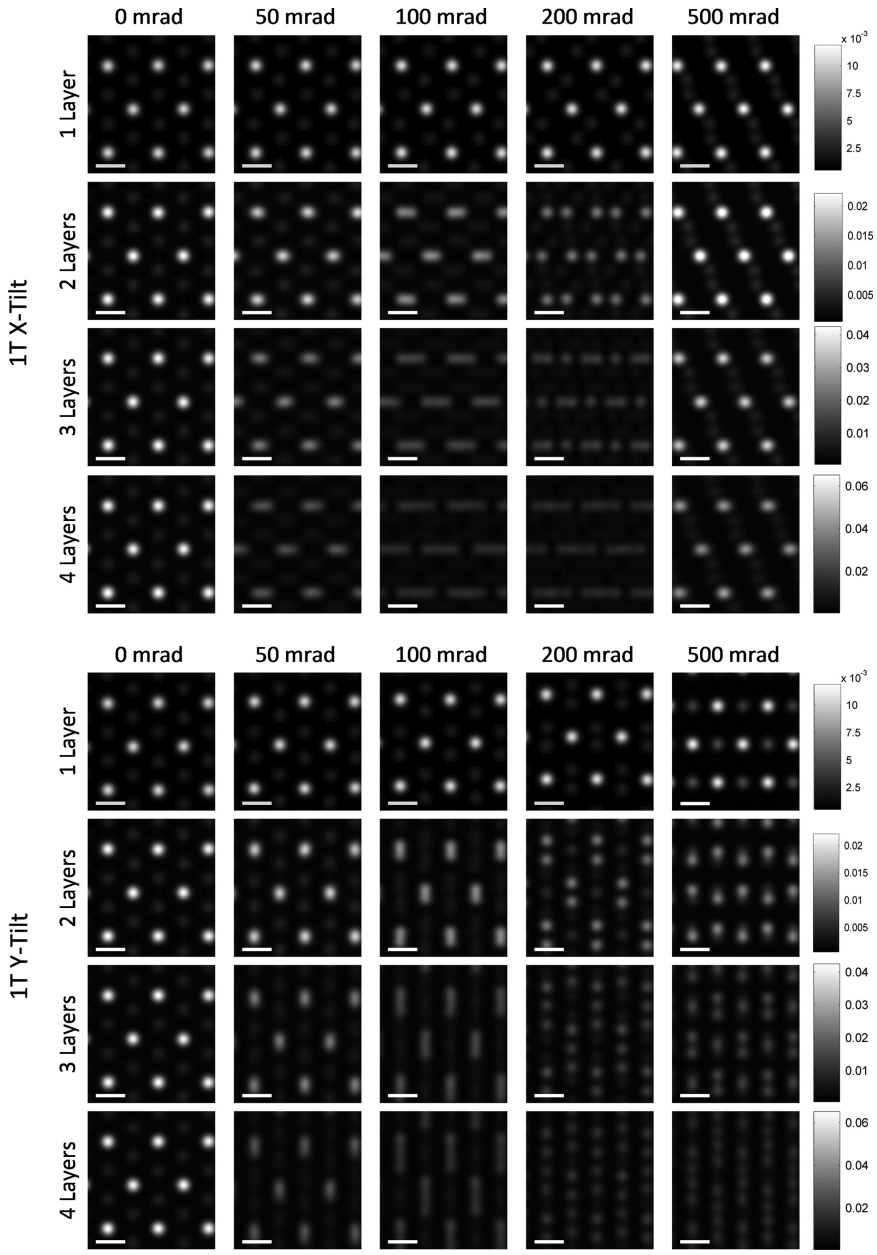

Figure 3.10: Simulated ADF-STEM images of 1T MoS_2 at various x- and y-tilt angles. Both tilt directions produce unique intensity patterns at all thicknesses as a result of overlapping of Mo and S atoms. Color bars are scaled to each row with intensities normalized to the incident beam; scale bars = 0.18 nm.

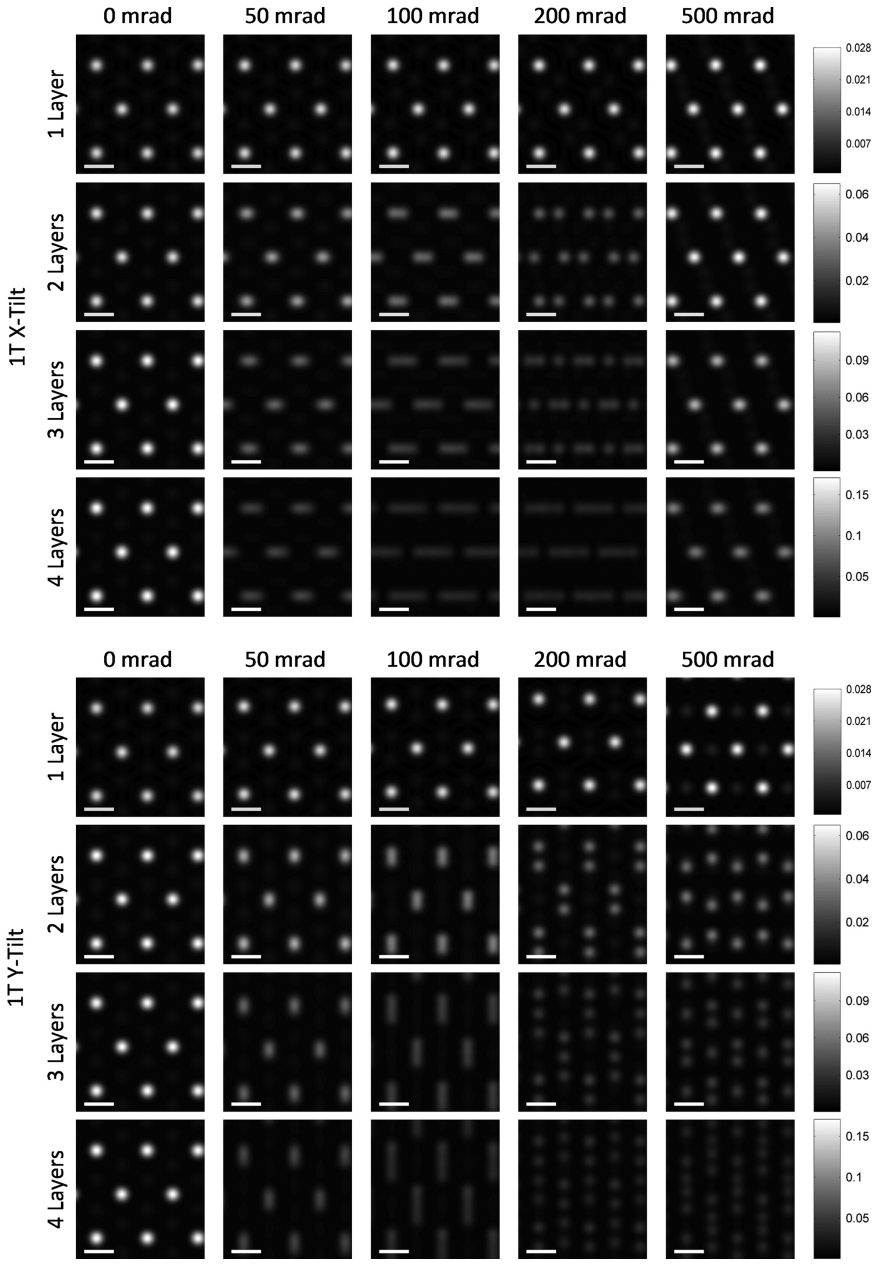

Figure 3.11: Simulated ADF-STEM images of 1T WS_2 at various x- and y-tilt angles. Both tilt directions produce unique intensity patterns at all thicknesses as a result of overlapping of Mo and S atoms. Color bars are scaled to each row with intensities normalized to the incident beam; scale bars = 0.18 nm.

2H polymorph, the shape of the higher intensity spots at 200 mrad x-tilt (or ~12°) can distinguish samples 1, 2, 3 and 4 layers thick as shown in Figure 3.10 and Figure 3.11. Near this tilt, the M (Mo or W) atoms are separated from each other in projection and are also separated from the X (S) atom clusters. A periodic array of M atom clusters are then projected in a shape that is dependent on the number of M atoms present, or hence, the number of layers. For a monolayer, only a single M atom is observed in each M cluster, for the bilayer, the 2M atoms appear as a dumbbell, and 3- and 4-layer-thick samples form a triangle and a rhombus, respectively. At this tilt angle, the distance between clusters is (or ∼0.25 nm) and is easily resolvable with little interference from X atom clusters. At five or more layers, it is difficult to resolve the shapes since M atoms overlap within each cluster in this projection.

Distinguishing the number of layers is contingent on the ability to resolve the dominating M atom clusters and the shape of the clusters. Although other tilt angles and directions also produce unique intensity contrasts for each thickness, 200 mrad x-tilt off of the [0001] zone axis appears as a projection with the least stringent imaging conditions for both 2H and 1T polymorphs. As simulation results indicate, it is indeed possible to unambiguously verify the thickness of 2H and 1T MoS_2 and WS_2 up to 4 layers using relative intensities in ADF-STEM images by analyzing the shapes created by overlapping M atoms at 200 mrad of tilt about the x-axis for 2H polymorph, and about any axis for the 1T polymorph.

3.3.3 Origin of ADF-STEM tilt series effects

Fundamentally, ADF-STEM imaging of tilted specimens allows distinction between different thicknesses of atomically thin layered materials because tilting produces unique projected atomic positions for each thickness. This is shown in Figure 3.12 for the 2H polymorph of TMDs. For very thin specimens (typically 1–3 layers thick) with small tilt angle (up to ~100 mrad or ~6°), when there is no overlap between adjacent columns, ADF-STEM images are roughly equivalent to projected structures of the crystal (with

intensities scaled by according to the Z of each atom) convoluted with the electron probe shape. However, when specimen thickness or tilt angle is large enough to cause overlap between atomic columns in projection, such simplification is not accurate anymore and detailed image simulations are needed even to predict qualitative image contrast. Even in such conditions, unique image contrast is observed for each thickness because the tilted structure is unique in each case.

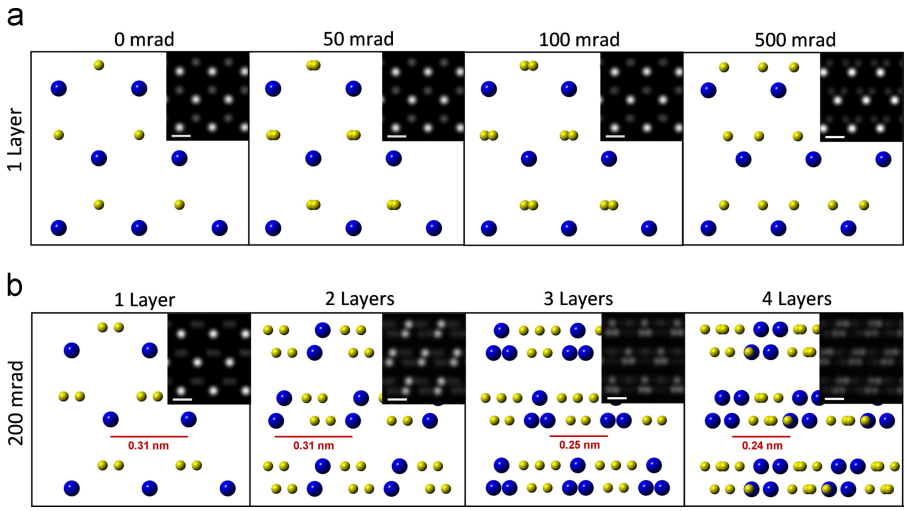

Figure 3.12: Crystal model of the 2H polymorph of MX_2: (a) Monolayer MX_2 in [0001] projection tilted at different angles of x-tilt, (b) 1 to 4 layers of MX_2 in [0001] projection tilted to 200 mrad of x-tilt. Corresponding simulated ADF-STEM images of 2H MoS_2 are presented as insets.

3.4 SAED characterization

3.4.1 Zone axis orientation

h-BN thickness determination

For samples aligned to the [0001] zone axis, changes in SAED pattern contrast between samples one, two, three, and four layers thick are practically indiscernible, at least with regard to the relative intensities of $\{10\bar{1}0\}$ and $\{11\bar{2}0\}$ spots. A comparison

of line scans through these two peaks in SAED patterns from h-BN samples 14 layers thick illustrates this (Figure 3.13). PACBED patterns, on the other hand, increase in contrast with increasing thickness (Figure 3.14) — the minimum of the central disc is 8.0% below the maximum for 1 layer, 15.1% for 2 layers, 21.6% for 3 layers, and 28.2% for 4 layers — but do not clearly differ in pattern symmetry.

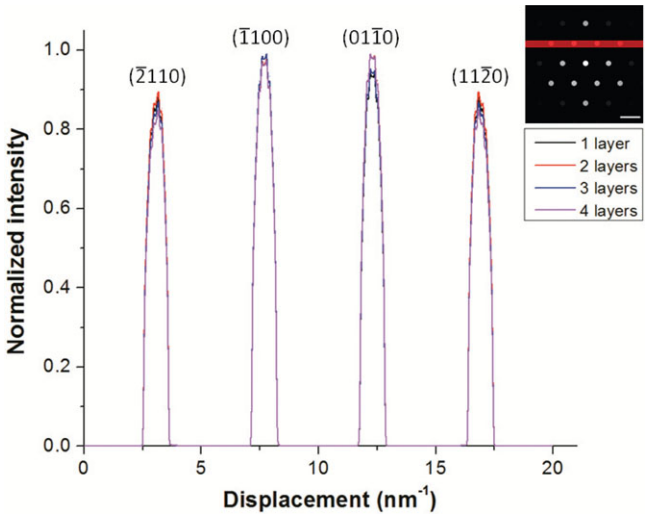

Figure 3.13: Line scans for [0001]-oriented samples of h-BN through $\{10\bar{1}0\}$ and $\{11\bar{2}0\}$ reflections; red stripe indicates the band of the diffraction pattern for which line scans were performed. Diffracted spot intensities are plotted on a linear intensity scale, with each line scan individually normalized to its maximum value.

SAED patterns from [0001]-oriented h-BN cannot easily be used to distinguish between different thicknesses of h-BN because, unlike for few-layer graphite [30], there is no significant variation in zone-axis SAED pattern contrast as a function of increasing sample thickness. PACBED patterns from [0001]-oriented h-BN do not show any clear differences in pattern symmetry between samples 14 layers thick, so they do not lend themselves to qualitative determination of sample thickness; different thicknesses may be distinguished by the intensity range within the central disc, but even then PACBED could still be impractical due to the presence of experimental noise and the risk of severe beam damage associated with applying the method to few-layer h-BN.

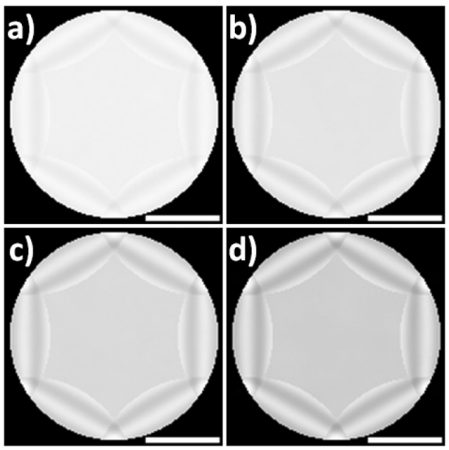

Figure 3.14: PACBED patterns for [0001]-oriented samples of h-BN (a) 1, (b) 2, (c) 3, and (d) 4 atomic layers thick. Linear intensity scale; scale bar = 2 nm^{1}.

TMD phase determination

SAED pattern simulations (presented in Figure 3.19 and Figure 3.20 below) show that the 2H and 1T polymorphs exhibit similar diffraction spot positions but different intensities at the [0001] zone axis. Figure 3.15 summarizes the ratios of the intensity of $\{10\bar{1}0\}$ spots to that of $\{11\bar{2}0\}$ spots for both materials and polymorphs at all four thicknesses. $\{10\bar{1}0\}$ spots in 2H polymorphs have ∼75% the intensity of $\{11\bar{2}0\}$ spots for all four thicknesses. On the other hand, in 1T polymorphs $\{10\bar{1}0\}$ spots have only ∼25% of the intensity of $\{11\bar{2}0\}$ spots, again for all four thicknesses. This factor of 3 difference between 2H and 1T intensity ratios that is observed for all four thicknesses can be used to distinguish the two polymorphs.

3.4.2 Tilt series

h-BN thickness determination

Tilt effects for SAED of few-layer h-BN were examined for a 0500 mrad range for each x-tilt (Figure 3.16) and y-tilt (Figure 3.17). For a one-layer-thick sample, SAED patterns are tilt-independent. However, for a multilayered sample, tilting produces changes in

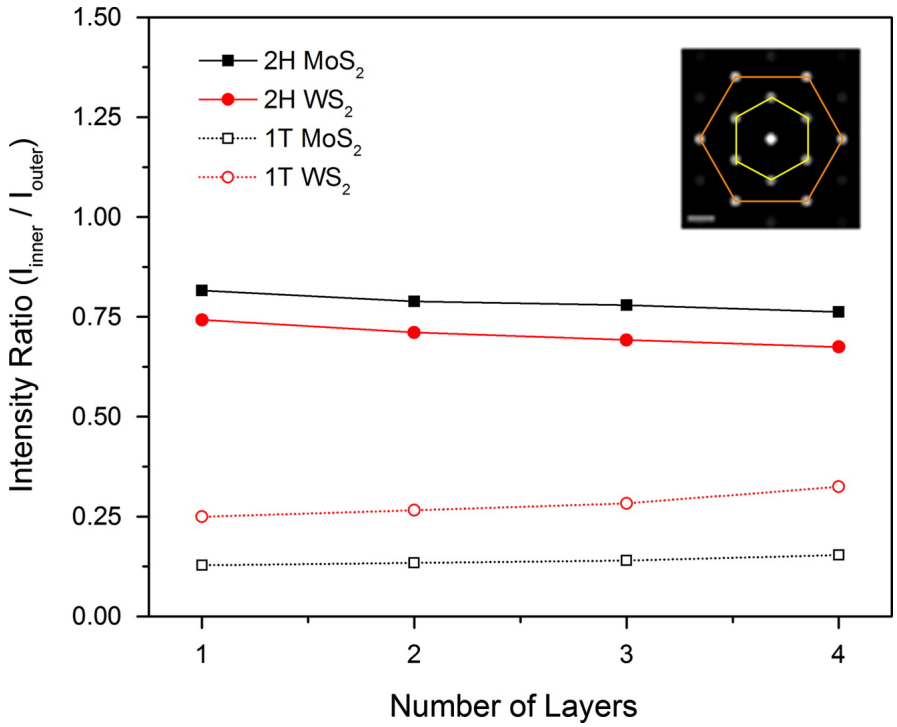

Figure 3.15: Intensity ratios of $\{10\bar{1}0\}$ to $\{11\bar{2}0\}$ spots of [0001] zone axis SAED pattern simulated for both materials and polymorphs. The yellow and orange hexagon traces in the inset diffraction pattern are the two sets of spots that were used to evaluate the average $I_{\{10\bar{1}0\}}$ and $I_{\{11\bar{2}0\}}$.

diffracted-spot intensity, with the tilt series for each thickness being distinguishable from the others. In all cases, spots appear and disappear in a band perpendicular to the tilt axis.

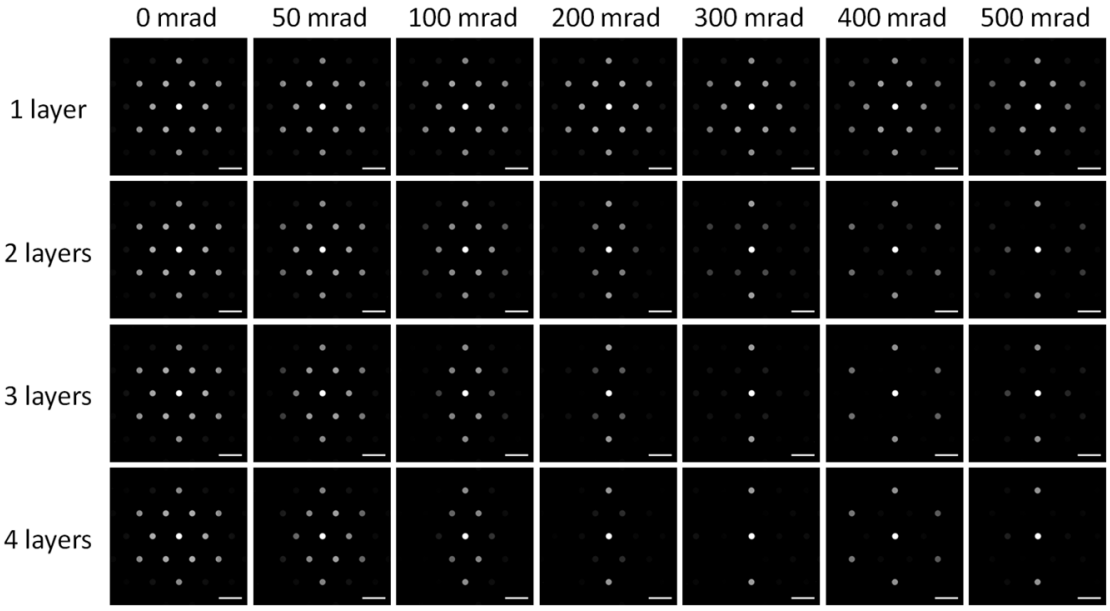

Figure 3.16: Series of simulated ADF-STEM images of atomically thin h-BN for an aberration-corrected 100 keV TEM, x-tilts. For a one-layer-thick region, tilt only serves to produce a distorted projection of the honeycomb-structured layer; for multiple-layer regions, tilting introduces distinctive complex distortions to the images, visible as streaking perpendicular to the y-axis. Linear intensity scale; scale bar = 0.2 nm.

To more precisely show the effect of sample tilt on different thicknesses of h-BN, the intensity of individual diffracted spots is plotted as a function of sample tilt in Figure 3.18; one $\{10\bar{1}0\}$ and one $\{11\bar{2}0\}$ spot is chosen for each tilt direction, all spots being chosen on account of their strong tilt-sensitivity for a given tilt series. These plots display the distinct thickness-dependent pattern of intensity maxima and minima over the course of a tilt series.

SAED characterization over a tilt series permits unambiguous distinction of a single sheet from multilayered samples, and of multilayered samples of different thicknesses from one another, by observing changes in SAED pattern contrast over a tilt series.

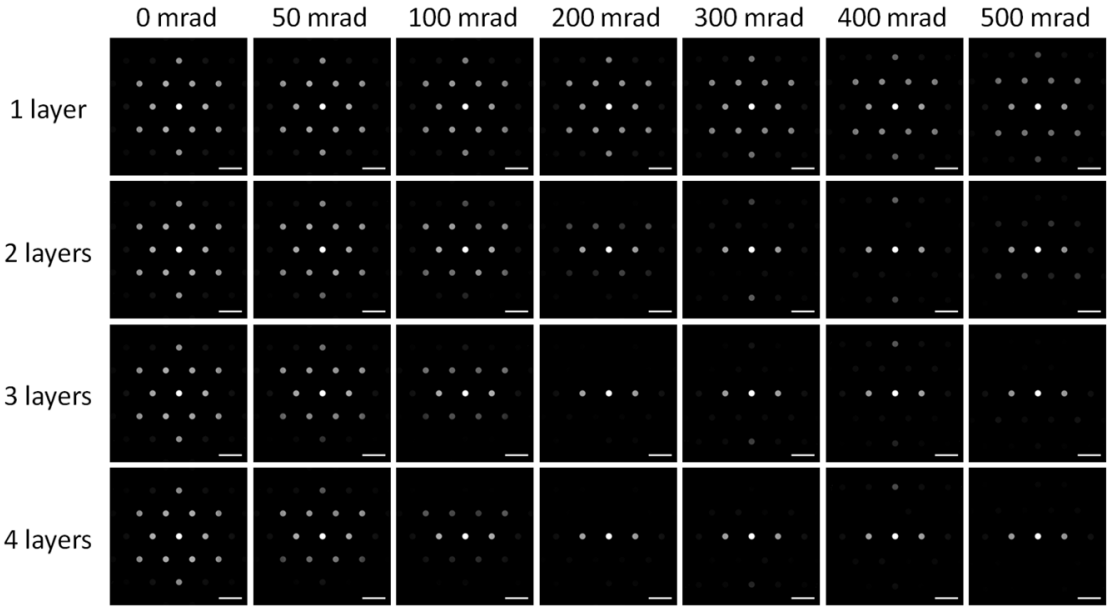

Figure 3.17: Series of simulated ADF-STEM images of atomically thin h-BN for an aberration-corrected 100 keV TEM, y-tilts. For a one-layer-thick region, tilt only serves to produce a distorted projection of the honeycomb-structured layer; for multiple-layer regions, tilting introduces distinctive complex distortions to the images, visible as streaking perpendicular to the y-axis. Linear intensity scale; scale bar = 0.2 nm.

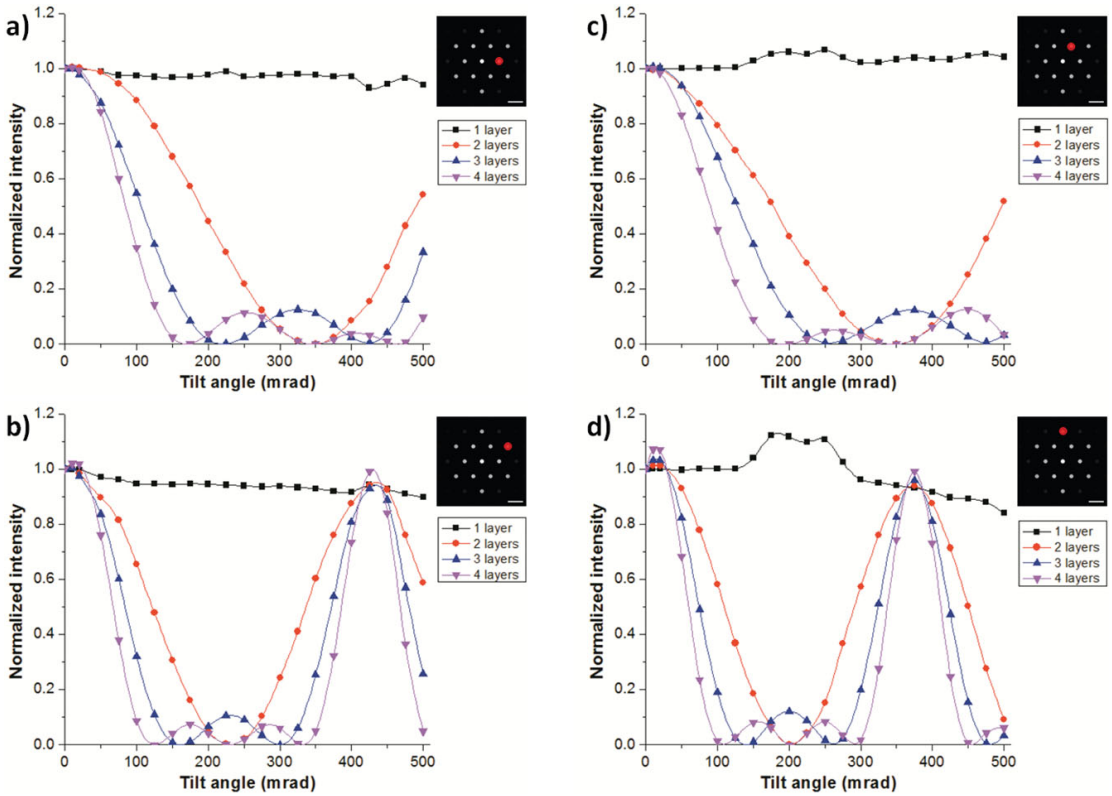

Figure 3.18: Intensity variation of diffracted spots as a function of tilt angle and sample thickness. For both x-tilt and y-tilt series, one $\{10\bar{1}0\}$ and one $\{11\bar{2}0\}$ reflection was chosen and then analyzed for samples 14 layers thick. (a) $(10\bar{1}0)$ over x-tilt series. (b) $(11\bar{2}0)$ over x-tilt series. (c) $(01\bar{1}0)$ over y-tilt series (d) $(\bar{1}2\bar{1}0)$ over y-tilt series. Each simulated data point is a 7×7 average of the pixels surrounding the center of that diffracted spot. Intensity values are normalized to the averaged value at the [0001] zone axis.

Only a single sheet will not have contrast change with tilts away from the [0001] zone axis, whereas diffracted spots strongly vary in intensity over the tilt series for samples two layers and thicker.

Also, tilting through the 100–500 mrad range may permit distinction between sheets two, three, and four atomic layers thick based on distinctive differences in SAED contrast between different sample thicknesses by measuring the angle at which the most tilt-sensitive $\{10\bar{1}0\}$ spot disappears and comparing against the different characteristic angles at which it would disappear for different thicknesses. It is noted, however, that successful experimental implementation of this thickness determination method would require areas of uniform thickness large enough to be exclusively selected by the SAED aperture or by the illumination of a moderately converged beam.

TMD thickness determination

The simulated SAED $\{10\bar{1}0\}$ spots at [0001] zone axis show comparable intensities at each thickness allowing easy identification of the honeycomb reciprocal lattice structure of 2H MoS_2 and WS_2 regardless of the number of layers. This is evident in the SAED simulations for 2H MoS_2 as shown in Figure 3.19. 2H WS_2 SAED tilt series (not presented here) showed no qualitative differences from the 2H MoS_2 results. SAED simulations also indicate that both the $\{10\bar{1}0\}$ and $\{11\bar{2}0\}$ spots are affected by x- and y-tilt for all four thicknesses including the monolayer.

Thickness identification of 1T structures through SAED pattern analysis becomes challenging as the intensities of diffraction spots vary non-intuitively with tilt off of [0001] at all thicknesses. Figure 3.20 shows the simulated SAED patterns for 1T MoS_2 and shows a hexagonal array of diffraction spots that oscillate asymmetrically about the y-axis during x-tilt, and oscillate symmetrically about the x-axis during y-tilt. This arises from the structure of $\{10\bar{1}0\}$ relrods, which are asymmetric about the center. At [0001] zone axis, the $\{11\bar{2}0\}$ planes scatter at higher intensity than the $\{10\bar{1}0\}$ planes.

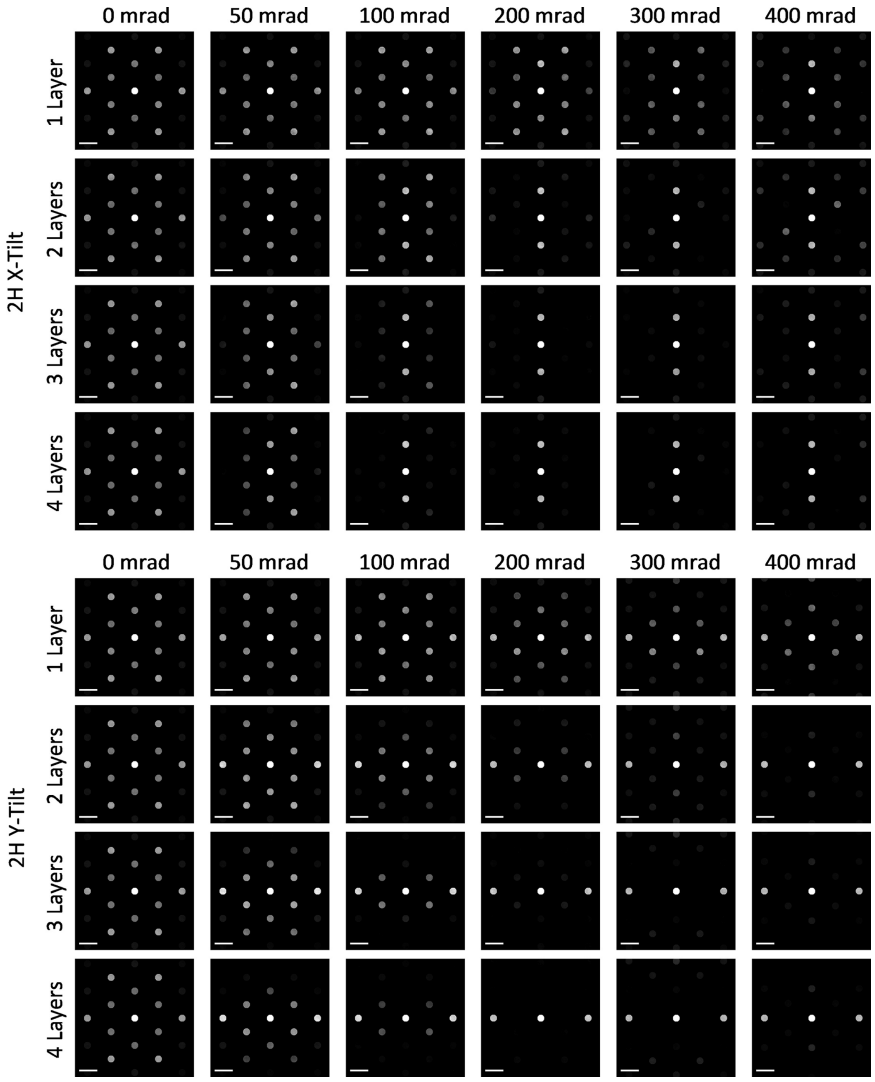

Figure 3.19: Simulated SAED patterns of 2H MoS_2 at various x- and y-tilt angles. Both monolayer and multi-layer patterns contain diffraction spots that vanish with tilt, primarily for the band of spots perpendicular to the tilt axis. Linear intensity scaling; scale bars = 2.4 $nm^{-}1$.

SAED tilt series for 1T WS_2 were also simulated and they appear very similar to 1T MoS_2, thus are not shown here.

The SAED simulations presented in Figure 3.19 and Figure 3.20 indicate that diffraction spots gain and lose intensity with tilt away from the [0001] zone axis in either direction for all thicknesses. By tracking the intensity of particular diffracted beams as a function of tilt angle as shown in Figure 3.21, it can be seen that at every thickness, these TMD materials produce diffracted beams with clear intensity maxima and minima over the course of the 0500 mrad tilt series. The fact that diffraction spots can vanish with sufficient tilt off of [0001] even for monolayers of MoS_2 and WS_2 distinguishes these TMD materials from truly planar graphene and h-BN monolayers. [40, 57]

Despite the fact that SAED pattern contrast is not tilt-invariant for TMD monolayers, a monolayer and multilayer sample can still be distinguished, as also experimentally demonstrated [33] on 2H MoS_2: the intensity at the $\left(10\bar{1}0\right)$ spot for the monolayer retains most of its intensity at ∼200 mrad tilt while for the bilayer it vanishes entirely. For 2H MoS_2 bilayer samples, the extinction of the $\left(10\bar{1}0\right)$ spot at 200 mrad of tilt paired with an intensity maximum around 300–350 mrad should permit unambiguous identification of this thickness. 3- and 4-layer samples exhibit barely identifiable extinction of the $\left(10\bar{1}0\right)$ spots at tilts of ∼150–175 mrad and ∼100125 mrad, respectively, followed by a second minimum in the 4-layer at 200–225 mrad. In addition, the $\left(10\bar{1}0\right)$ relrod is symmetric about the Bragg condition (s_z=0). Thus, tilting in either the positive or negative direction will result in the same extinction behaviors. Applying the kinematic model and dynamical simulations to WS_2 (results are not included) shows that the behavior of the 2H WS_2 $\left(10\bar{1}0\right)$ spot is similar to that of 2H MoS_2.

Based on SAED results in Figure 3.20, the same methods do not translate as well to 1T samples to discern the number of layers. One pair of $\left(10\bar{1}0\right)$ spots appear to begin with little intensity and gain intensity with tilt for all thicknesses, albeit interrupted by oscillations in intensity along the way to the 500 mrad peak value; this behavior is unique to 1T specimens and could be used to distinguish the two polymorphs from each

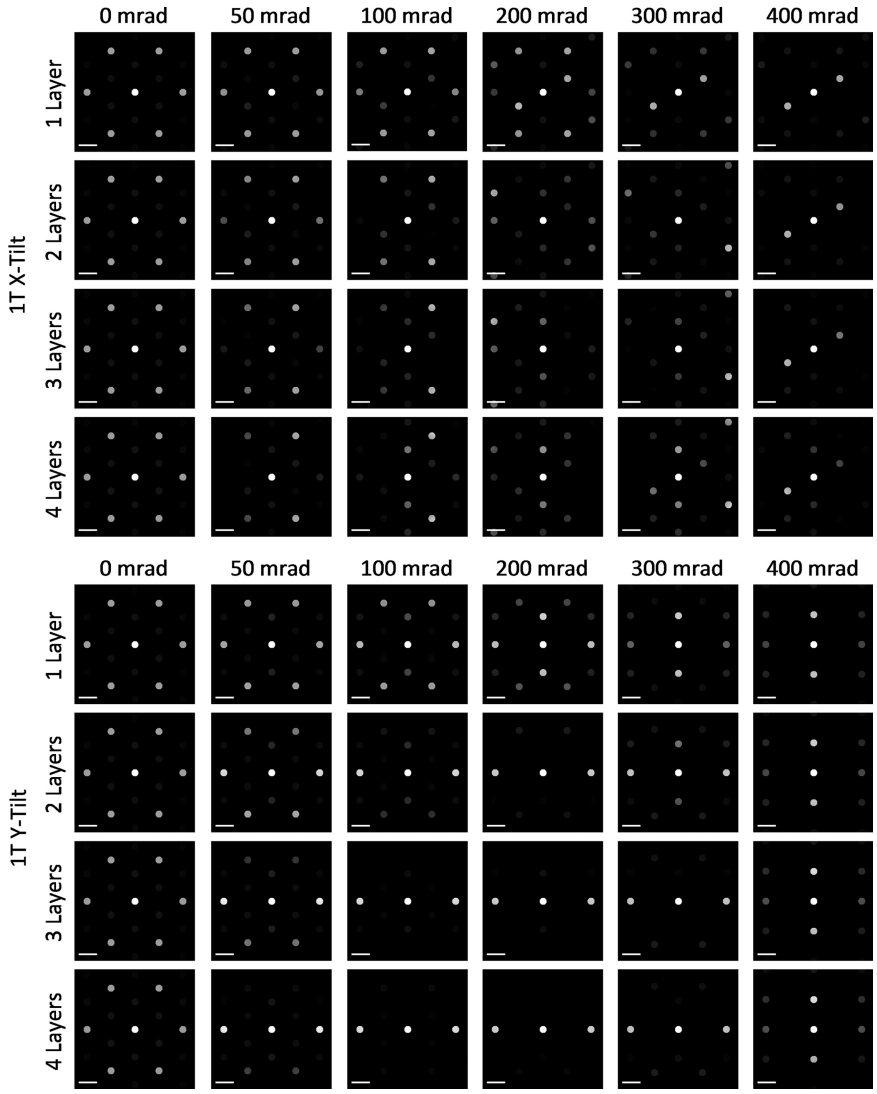

Figure 3.20: Simulated SAED patterns of 1T MoS_2 at various x- and y-tilt angles. Both monolayer and multi-layer patterns contain diffraction spots that vanish with tilt, primarily for the band of spots perpendicular to the tilt axis. Linear intensity scaling; scale bars = 2.4 $nm^{-}1$.

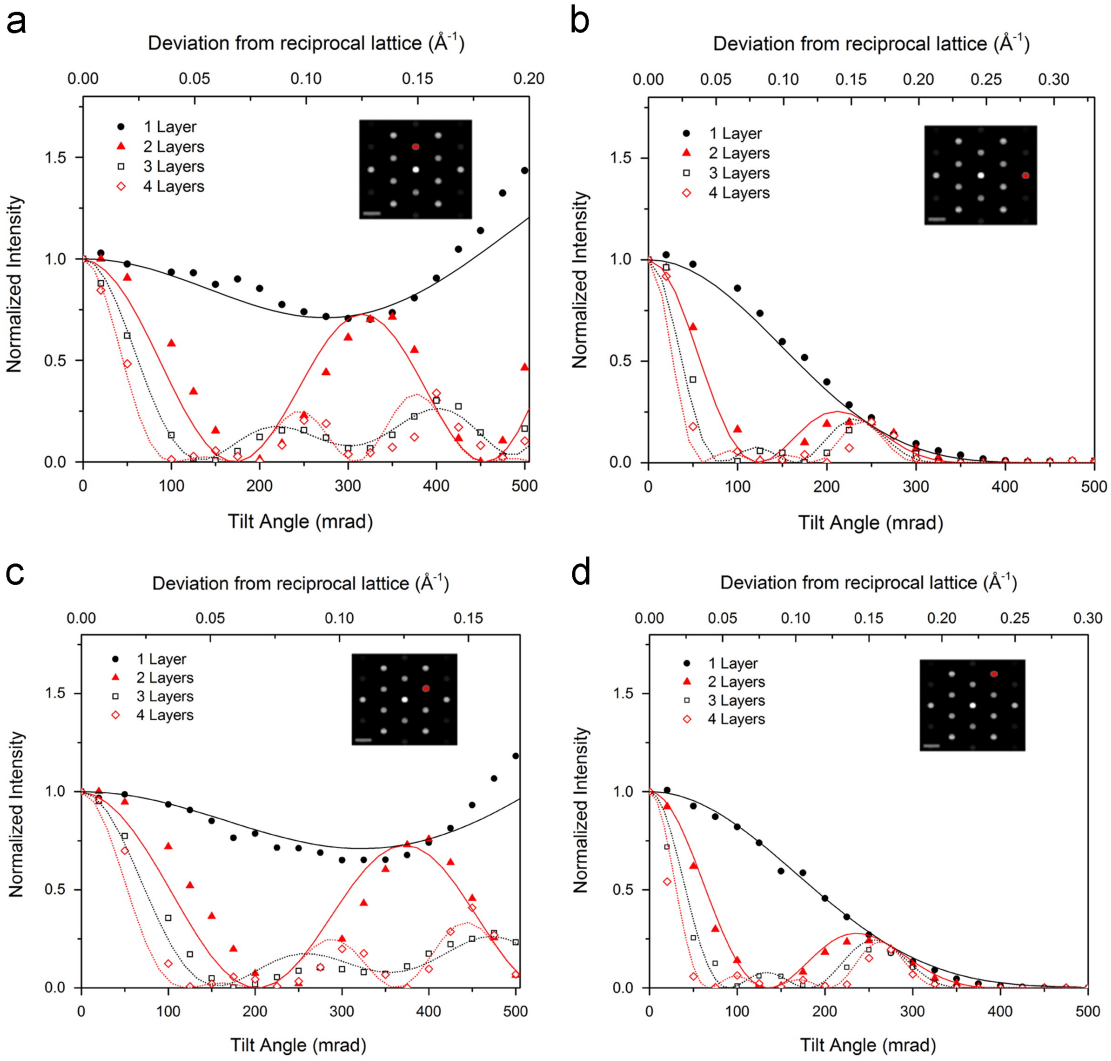

Figure 3.21: SAED spot intensity variations as a function of tilt angle for 1- to 4-layered 2H MoS_2. The spot tracked in each plot is highlighted in red in the sample diffraction pattern. Scattered points represent simulated multislice data; solid lines represent a kinematic diffraction calculation. (a) $(10\bar{1}0)$ over y-tilt series. (b) $(1\bar{2}10)$ over x-tilt series. (c) $(1\bar{1}00)$ over y-tilt series (d) $(2\bar{1}\bar{1}0)$ over x-tilt series. Each simulated data point is a $12 times 12$ average of the pixels surrounding the center of that diffracted spot. Intensity values are normalized to the averaged value at the [0001] zone axis.

other. For thickness determination, the high intensity of the $(10\bar{1}0)$ spot at 200 mrad y-tilt for the monolayer is a strong contrast from the almost vanishing behavior of the same spot for thicker samples, which is consistent with the intensity variations along the $(10\bar{1}0)$ and $(1\bar{2}10)$ relrods. The relrods also show that bilayer and thicker samples do exhibit characteristic intensity variations as a function of tilt (extrema in the intensity oscillations of the $(10\bar{1}0)$ spots that increase in intensity with tilt and tilt-dependent behavior of the $(1\bar{2}10)$ almost identical to that of 1T), which may not be obvious from the diffraction patterns of Figure 3.20.

Beyond distinguishing monolayers and bilayers from thicker samples, observing the relative tilt-series intensity in SAED does not seem to be a practical means for measuring the thickness of TMDs; although simulations reveal signature behavior of 3- and 4-layer samples, these intensity variations are small and may be difficult to detect conclusively relative to those from monolayers and bilayers. Furthermore, the intensity variations of 3- and 4-layer samples are similar which makes thickness determination ambiguous. Successful use of this method would require a large area of sample with uniform thickness or a moderately converged beam that requires short exposure time to limit beam damage, neither of which is trivial to ensure. The use of these computational results also requires relatively accurate determination of the [0001] zone axis and tilt axis during experimental application. Because of the nearly two-dimensional nature of MX_2 TMD materials, 1- to 4-layer-thick flakes with reasonable lateral dimensions will likely be initially positioned near the [0001] zone axis when deposited on a standard TEM grid.

3.4.3 Origin of SAED tilt series effects

Lattice amplitude approximation for h-BN

SAED characterization over a tilt series permits unambiguous distinction of a single sheet from multilayered samples, and of multilayered samples of different thicknesses

from one another, by observing changes in SAED pattern contrast over a tilt series. Only a single sheet will not have contrast change with tilts away from the [0001] zone axis, whereas diffracted spots strongly vary in intensity over the tilt series for samples two layers and thicker. This effect arises from the three-dimensional (3D) periodicity of the reciprocal lattice — which in turn places a 3D constraint on the Bragg reflection condition — for samples two layers and thicker. By exactly treating the lattice amplitude factor G for a sample of N atomic layers with interlayer spacing c, it can be shown that the intensity of the out-of-plane relrod, I, would be a simple function of the deviation from the reciprocal lattice s_z:

$$I(s_z) = |F_{cell}|^2 |G|^2 = I_{max} \times sin^2(\pi N c s_z) / sin^2(\pi c s_z) \tag{3.1}$$

This function is plotted, over one period for a sample with the same interplanar spacing as h-BN, in Figure 3.22. It is this thickness-dependent relrod structure that accounts for the variations in spot intensity as a function of tilt observed in Figure 3.18, although the difference in atomic structure between alternating layers of h-BN will modulate the relrods asymmetrically for some of the diffracted spots (e.g., in panels (a) and (c) of Figure 3.16).

Exact structure factor calculations for TMDs

To understand the origin of this difference between diffraction patterns of TMD and truly planar two-dimensional materials, the exact intensities of relrods for TMD materials were calculated. This begins by more precisely framing the h-BN results above. For a layered material with a two-dimensional unit cell defined in the xy plane (corresponding to a set of reciprocal lattice vectors $\boldsymbol{g} = g_x\hat{\boldsymbol{x}} + g_y\hat{\boldsymbol{y}}$), the intensity, I, of a relrod as a function of the deviation of the reciprocal lattice point (in the zero-order Laue zone) from the Ewald sphere s_z, scattering vector $\boldsymbol{q} = \boldsymbol{g} + \boldsymbol{s} = g_x\hat{\boldsymbol{x}} + g_y\hat{\boldsymbol{y}} + s_z\hat{\boldsymbol{z}}$, lattice amplitude factor G, and structure factor F, for an N-layer sample with z-spacing

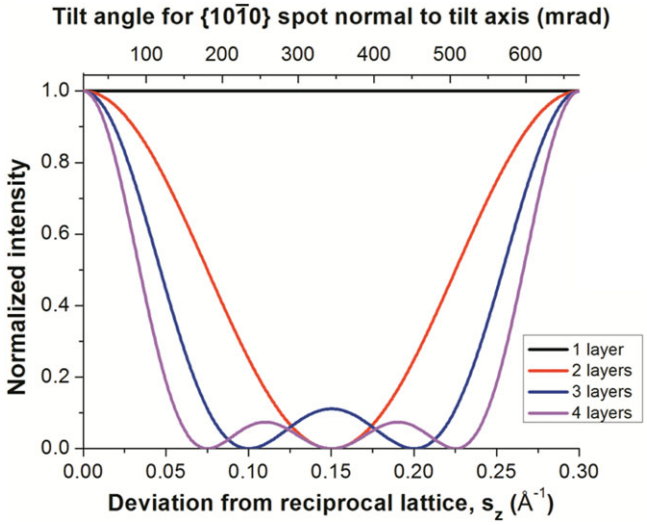

Figure 3.22: Single-period plot of the relrod intensity for identical atomic layers spaced 0.333 nm apart. If calculated using the scattering factors of B and N atoms with correct stacking order, these intensities would correspond to the exact out-of plane modulation of the relrods (the exact modulation is in fact mapped in the SAED tilt-effect simulations presented previously).

ct can be expressed as:

$$I\left(s_z\right)=\alpha|F\left(g_x,g_y,s_z\right)|^2|G\left(g_x,g_y,s_z\right)|^2=\frac{\alpha'\left(g_x,g_y\right)|F\left(g_x,g_y,s_z\right)|^2 sin^2\left(\pi N c s_z\right)}{sin^2\left(\pi c s_z\right)} \tag{3.2}$$

where α and α' are proportionality constants. In planar crystals such as graphene or monolayer h-BN the structure factor depends on s_z only due to the decrease of atomic scattering factor amplitudes with increasing q, corresponding to a slow decay of the diffracted spots with tilt away from zone axis but not any destructive interference extinctions. The variation in z position of the atoms in each TMD layer leads to an additional s_z dependence of structure factor due to the interference of the beams scattered from atoms within the layer. This accounts for why, even for TMD monolayers, $\{11\bar{2}0\}$ spots in 2H crystals and both $\{10\bar{1}0\}$ and $\{11\bar{2}0\}$ spots in 1T crystals disappear at sufficient tilt off of the [0001] zone axis.

Kinematic diffraction from TMD structures comprised of M and X atoms can be modeled by calculating the structure factor for electron scattering from a large-area TMD sheet. By treating the unit cell as three-dimensional rather than two-dimensional (the latter is inaccurate even for multilayers of graphene and h-BN due to the AB-type stacking of the atomic planes), and restricting the lattice amplitude G to solely treat tiling in the xy plane of an "effective unit cell" 14 layers thick in z, the intensity of electron scattering to a relrod intersecting the Ewald sphere with scattering vector $\boldsymbol{q}$ can be calculated as:

$$F\left(g_x, g_y, s_z\right) = F\left(\boldsymbol{q}\right) = \sum_i f_M\left(\boldsymbol{q}\right) exp\left[2\pi i\left(\boldsymbol{q}\cdot\boldsymbol{r_i}\right)\right] + \sum_j f_X\left(\boldsymbol{q}\right) exp\left[2\pi i\left(\boldsymbol{q}\cdot\boldsymbol{r_j}\right)\right] \quad (3.3)$$

$$I\left(g_x, g_y, s_z\right) = \alpha |F\left(g_x, g_y, s_z\right)|^2 |G\left(g_x, g_y\right)|^2 = \alpha'\left(g_x, g_y\right) |F\left(g_x, g_y, s_z\right)|^2 \quad (3.4)$$

In these equations, f_M and and f_X are the scattering factors for M and X atoms, respectively, and $\boldsymbol{r_i}$ and $\boldsymbol{r_j}$ are the real space atomic position vectors of those atoms within the unit cell. The calculated relrods are shown in Figure 3.23 for $\left(10\bar{1}0\right)$ and $\left(1\bar{2}10\right)$ diffraction spots for both 2H and 1T samples, using parameterized atomic scattering factors. [14]

The results of this model are also plotted alongside multislice results in Figure 3.21 above, being transformed into a function of tilt angle by accounting for the geometry of crystal tilt relative to the Ewald sphere. The kinematic model correlates well with the results of the dynamical simulation, both agreeing on the intensity oscillations of each tracked spot as a function of tilt angle and specimen thickness. Slight discrepancies arise due to approximations made by the multislice simulation: the z-component of elastic scattering is ignored and atomic positions are distorted by projecting them onto the nearest z-slice.

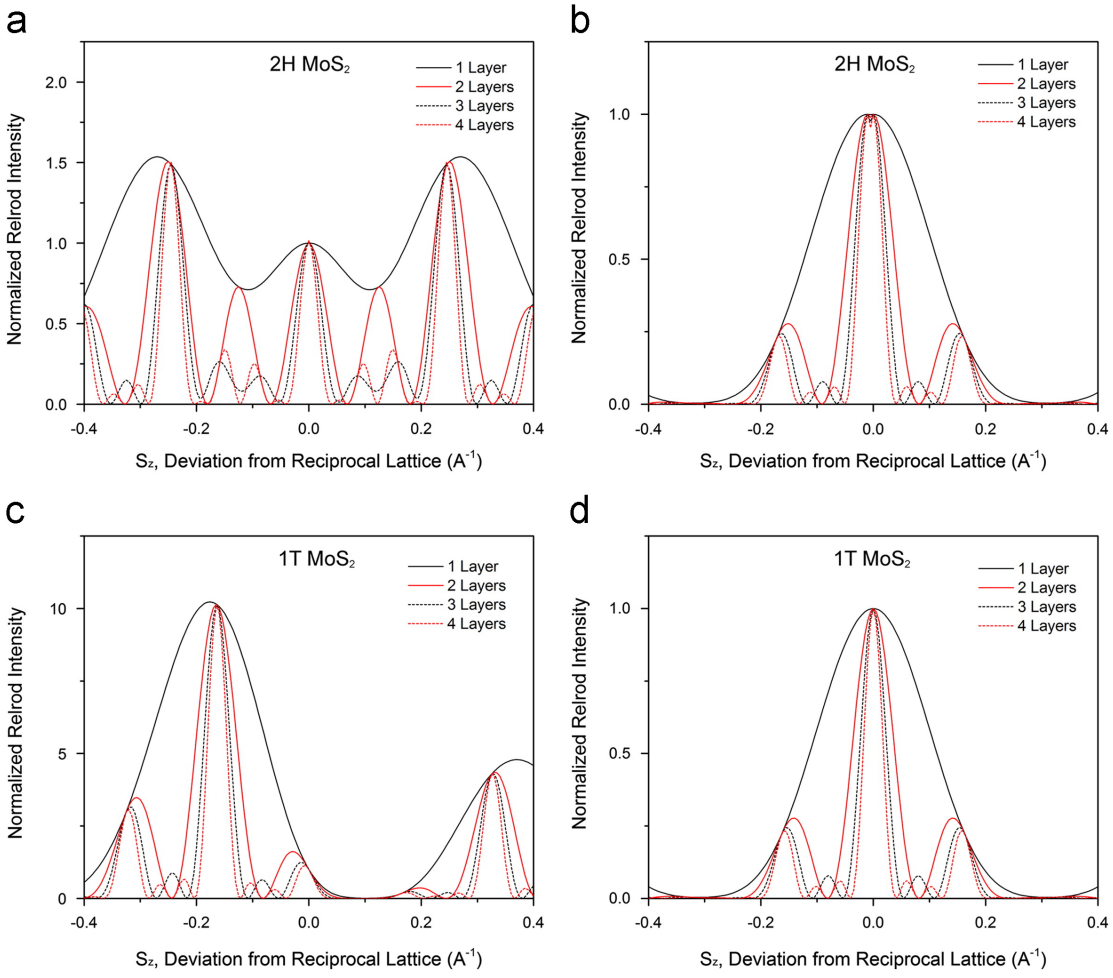

Figure 3.23: Intensity variation along reciprocal space lattice rod: (a) $(10\bar{1}0)$ spot, 2H MoS_2; (b) $(1\bar{2}10)$ spot, 2H MoS_2; (c) $(01\bar{2}0)$ spot, 1T MoS_2; (d) $(1\bar{2}10)$ spot, 1T MoS_2. Plots are constructed using the kinematic model of electron diffraction. Intensity values are normalized to the value at s_z=0.

3.5 Conclusion

Results from multislice simulations of h-BN indicate that both ADF-STEM imaging and SAED are both clearly tilt-sensitive, and that both can readily be employed to identify a freestanding h-BN monolayer. Although careful ADF-STEM imaging of [0001]-oriented h-BN (ideally including full quantitative calibration of an experimental image) can potentially be used to measure sample thickness, observing the evolution of an ADF-STEM image or SAED pattern with tilt is a clearer means of identifying h-BN monolayers from raw TEM data. Additionally, these simulation results indicate that ADF-STEM images and SAED patterns collected for a tilt series off of the [0001] zone axis could be used to identify regions two, three, or four atomic layers thick.

Simulations of TMD materials show that tilt effects are apparent when employing these same TEM techniques for both 2H and 1T polymorphs of MoS_2 and WS_2 samples, even at the monolayer thickness. Either SAED or ADF-STEM can be reliably used with tilting off of zone axis [0001] to distinguish monolayer samples from multilayers, and in some cases distinguish different-thickness multilayers from each other. It appears that neither technique can unambiguously identify layer count solely based on relative intensity contrast at zone axis [0001], with the exception of monolayer 2H WS_2; however, layer differentiation is possible at zone axis [0001] using absolute intensities in ADF-STEM if the ADF signal is accurately quantified and compared to an equivalent simulation. The results also clearly show that ADF-STEM and SAED can be used to distinguish the 2H and 1T polymorphs of MoS_2 and WS_2 from each other.

From a fundamental perspective, these studies clearly explain the origin of tilt-series thickness determination using either ADF-STEM images or SAED patterns. In the case of ADF-STEM imaging, thickness determination is possible due to the unique evolution of the projected atomic structure as a function of tilt for different thicknesses of these 2D materials. In the case of SAED, thickness determination is possible due to the unique changes in the reciprocal lattice relrod structure as a function of material

thickness. It has also been shown that tilt series SAED of true 2D monolayers and quasi-2D monolayers are fundamentally different due to differences in their reciprocal lattice structure; surprisingly, these differences amount to picoscale thickness measurement sensitivity for quasi-2D materials such as TMDs!

The thorough analysis of tilt-series SAED presented here helps to theoretically ground this method not only in truly planar layered materials such as graphite and h-BN, but also in more complex systems such as TMDs. Recent work by a coworker has confirmed the applicability of this method for thickness determination of zeolite nanosheets, which have still more complex crystal structure than TMDs, as well as extended tilt-series SAED as a means to characterize anisotropic wrinkling in layered materials. [58] The continued proliferation of SAED as a method of thickness determination for other atomically thin crystals (such as black phosphorus) is expected, as well as experimental demonstration of tilt-series ADF-STEM thickness determination.

Chapter 4

Probing core electron orbitals and measuring the delocalization of core-level excitations

4.1 Introduction

While all matter is comprised of atoms, our understanding of the electron orbitals that determine how those atoms behave is mostly based on theory or indirect evidence rather than on direct experimental measurements of electron density. Nevertheless, the mapping of electron densities in near-defect-free crystals has been demonstrated by structure factor determination for X-ray diffraction [59] and transmission electron microscopy (TEM) convergent beam electron diffraction. [60–62] Real-space characterization of the bonding electron orbitals of individual molecules and surface atoms has also been shown using atomic force microscopy [63, 64] and scanning tunneling microscopy. [65, 66] Going another level deeper and probing core-level electron orbitals, which are much smaller than bonding orbitals, presents a major experimental challenge. In this study, scanning transmission electron microscopy (STEM) was used in

conjunction with X-ray energy-dispersive spectroscopy (XEDS) to probe core-level electron orbitals in a $SrTiO_3$ crystal, and furthermore to measure the impact parameter for excitation of a given orbital. These results serve as a novel measurement of the sub-atomic structure of matter as well as a demonstration of the very fine resolution and precision of analytical STEM techniques. They pave the way for very precise STEM measurements of elemental composition, core-level electronic states, localization of beam-sample interactions, and other spectroscopic information.

For decades, STEM has proven an immensely powerful tool for imaging and chemically fingerprinting atoms. With the advent of aberration-correction, [11, 12] sub-angstrom STEM electron beams can be combined with XEDS or electron energy-loss spectroscopy (EELS) to rapidly map solids with crisp atomic resolution. While XEDS collects X-rays emitted by beam-excited atoms and EELS analyzes electrons that have inelastically scattered from the sample — each in parallel with annular dark-field (ADF) structural images — both mapping techniques have proved invaluable for visualizing the distribution of elements in a material all the way down to the atomic scale. [67–70] These capabilities have far-reaching ongoing impact in materials science. In this chapter, however, STEM-XEDS mapping is extended beyond elemental profiling of whole atoms to probe characteristics of core-level electron orbitals.

4.2 Methods

Single-crystal $SrTiO_3$ (STO) was chosen as a test material to demonstrate the method. Electron-transparent TEM specimens were prepared using combinations of mechanical wedge polishing (Allied MultiPrep), focused ion beam lift-out (FEI Quanta 200 3D), and Ar-ion milling (Fischione ion mill Model 1010 and Gatan PIPS). Three different specimens were used in three independent days of experiments, with specimen thicknesses estimated by low-loss EELS [7] using a mean-free-path for plasmon scattering of $\lambda_{STO} \approx 123$ nm. Measured thicknesses of the specimens for the Day I, II,

and III experiments were approximately 50, 60, and 35 nm, respectively. It should be noted that due to the presence of other strong inelastic features in low-loss EELS, the thickness values are likely slight overestimates.

There were several advantages to using STO, not least the availability of high-quality single crystals, its multi-element composition, and its high resistance to electron beam damage. Using a fifth-order aberration-corrected STEM operated at 300 keV and equipped with a high-efficiency XEDS system, X-ray maps were collected from ⟨001⟩-oriented STO specimens, including Sr K and L, Ti K and L, and O K signals. In these experiments X-ray maps were collected simultaneously along with high-angle ADF (HAADF) images. An example of one such data set is shown in Figure 4.1, where a combined map of Sr K, Ti K, and O K X-ray signals is shown along with a HAADF-STEM image; separate Sr K and Sr L maps are also presented. Similar XEDS maps of STO have been reported previously and can be routinely obtained using aberration-corrected STEMs. [70–72]

An aberration-corrected (CEOS DCOR probe corrector) FEI Titan G2 60-300 STEM equipped with a Schottky X-FEG monochromator gun was used in this study. The microscope was operated at 300 keV with spot size setting number 9. A standard high-contrast tuning specimen, a carbon diffraction grating replica coated with Au nanocrystals, was used for aberration measurement and correction. Once HAADF imaging resolution was deemed within a reasonable range, the STO specimen was inserted. The quality of imaging, both in corrector-tuning and XEDS mapping conditions, was documented, showing the spatial resolution of the microscope to be stable with respect to specimen exchange and increasing probe current (I_p) for XEDS mapping (Figure 4.2).

Multislice simulations [73,74] were performed to model the interaction of the STEM focused electron beam with the STO crystal. Using the TEMSIM multislice package, [14] incident aberration-corrected electron probes of various sizes were scanned over a ⟨001⟩-oriented STO supercell (1.56×1.56 nm^2 consisting of 4×4 unit cells). Both probe and transmission functions were calculated on a 1024×1024 pixel grid, which resulted in

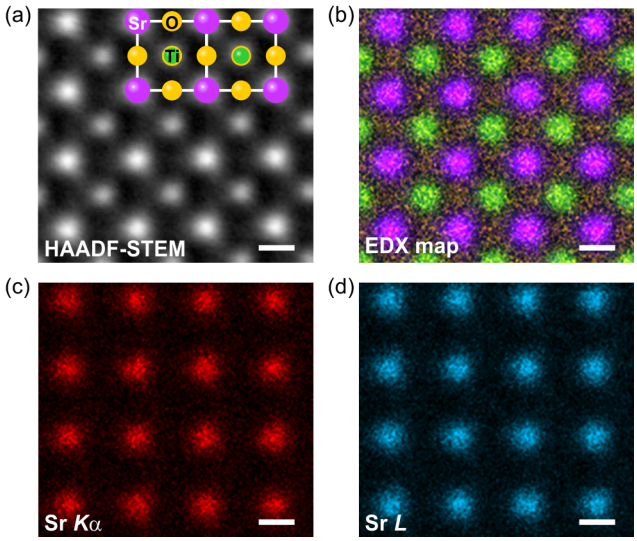

Figure 4.1: (a) HAADF-STEM image of STO viewed along a ⟨001⟩ crystallographic direction. A model of the atomic positions is overlaid on the image to clarify identification of atomic columns. (b) Composite STEM-XEDS map of STO, superposing combined Sr K and L (purple), Ti K (green), and O K (yellow) maps. Individual XEDS maps of Sr K (c) and Sr L (d) are also shown, demonstrating simultaneous atomic-resolution XEDS using two different characteristic X-ray types. The scale bar is 0.2 nm in length. XEDS maps were acquired simultaneously by collecting a full 0-20 keV XEDS spectrum at each probe position. The non-circular symmetry of the STEM probe tails produces slightly asymmetric shapes of the atomic columns in HAADF-STEM images and STEM-XEDS maps, a subtle effect that is largely invisible in data sets with lower signal-to-noise ratios.

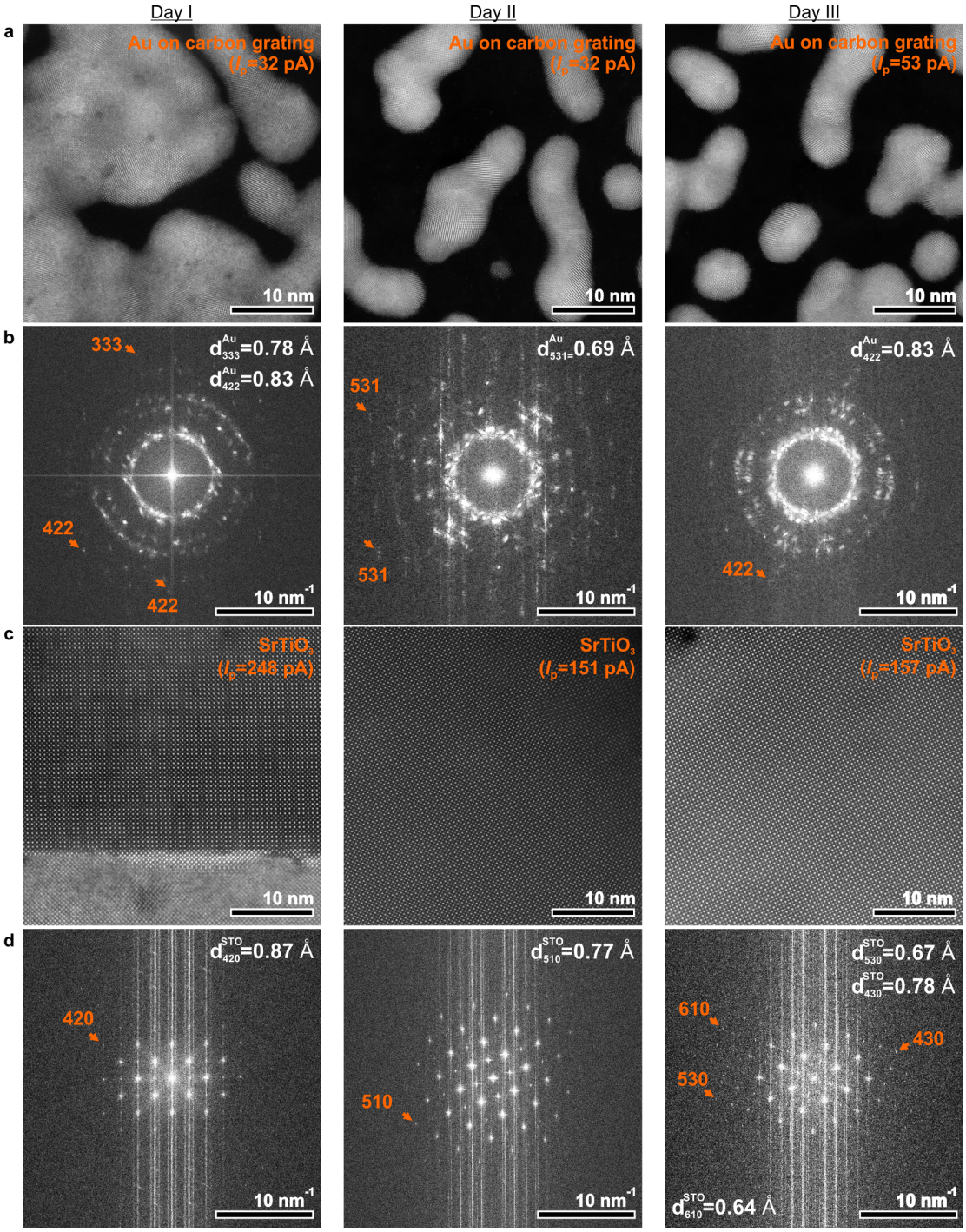

Figure 4.2: Resolution tests after probe correction and before XEDS acquisition from each days experiment: (a) and (b), high-resolution HAADF-STEM image from the Au specimen and its FFT; (c) and (d), high-resolution HAADF-STEM image from the STO specimen and its FFT. The probe currents (I_p) for the experiments were indicated on the HAADF-STEM images. Information limits and selected lattice spacings are indicated on the corresponding FFTs.

a real space pixel size of $\Delta x = \Delta y = 1.53$ pm and a reciprocal space pixel size of $\Delta k_x = \Delta k_y = 0.64$ nm^{-1}. Projected atomic potentials were calculated with a slice thickness commensurate with the crystal structure (Δz =0.195 nm). Frozen phonon configurations were calculated as isotropic random displacements of the atomic positions according to the Einstein model, [49] with root-mean-square displacements 4.9, 3.5, and 4.5 pm for O, Ti, and Sr, respectively. [75] HAADF-STEM image simulations were performed by forming 2D images at various sample depths using a detector spanning semi-angles 50200 mrad, and averaging many frozen phonon configurations at 300 K. Channeling simulations were performed with the beam intensity being tracked by saving a 2D intensity map at every z-slice for any given incident probe position.

4.3 Results and discussion

The method of orbital characterization described here relies on two basic concepts. First, because these X-rays are produced solely by filling empty states in core-level orbitals (1s and 2p orbitals for K and L X-rays, respectively), each X-ray map is really a spatially resolved measurement of core electron excitation probability for a specific orbital, also known as the transition potential. Second, when two different X-ray maps are collected simultaneously for the same element — such as both K and L from Sr atoms in Figure 4.1(c) and Figure 4.1(d) — it is possible to directly compare the two orbitals, as they are measured in exactly equivalent conditions: an identical incident beam (which is column-independent) undergoing identical propagation through the sample (which is column-specific). The ability to probe and record two different pairs of XEDS maps from two different atoms, all under the same STEM operational conditions, makes this study even more robust and minimally sensitive to instrument variability. Using extensive low-noise data sets, it also allows us to go beyond routine elemental analysis and confidently glean differences between the orbitals probed in these maps.

4.3.1 Experimental XEDS spectrum imaging

To increase the signal-to-noise ratio (SNR) of STEM-XEDS maps, many X-ray maps from identical atomic columns, all recorded in the same experiment, are cross-correlated and averaged together. Raw STEM-XEDS maps consisting of around 8×8 STO unit cells were cut into individual single-column images that include a single atomic column with an extra "buffer" region. The areas selected in an example raw Sr L XEDS map are shown in Figure 4.3(a), and the 49 individual images cut from Figure 4.3(a) are shown in Figure 4.3(b). The individual single-column images are then aligned to a reference image using the cross-correlation algorithm and then averaged to reduce statistical noise of the images. Figure 4.3(b) shows the reference image and the resulting improved-SNR image after this step. Because individual images are relatively noisy, none of these images can be used as a reliable reference (the cross-correlation algorithm is not stable for this level of noise). While any smooth 2D function with a somewhat similar shape will work, a 2D gaussian image was used as the reference image, where its FWHM was chosen to optimize the cross-correlation process.

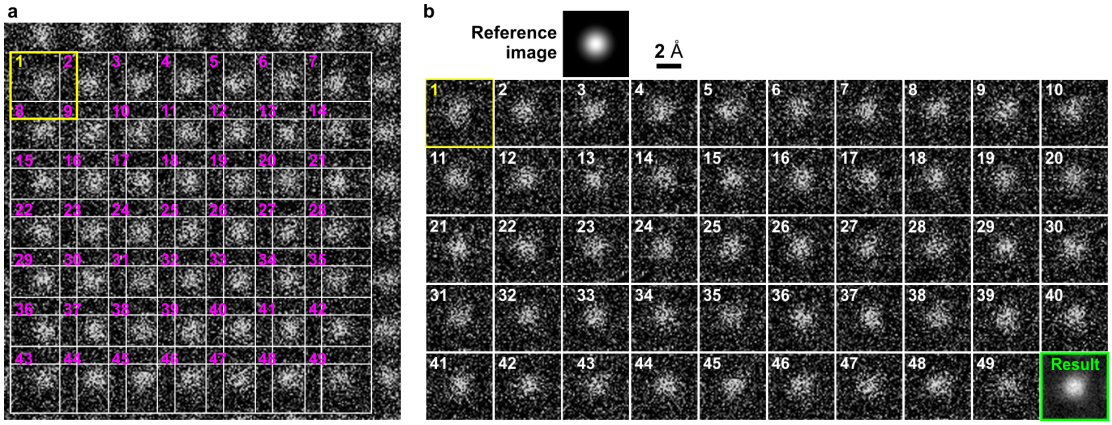

Figure 4.3: (a) Raw Sr L XEDS map of 600×600 pixel^2 image size, where 49 overlapping squares 101×101 pixel^2 in size are selected with each centered on a Sr atomic column. (b) 49 individual single-column images from (a). A reference image, a 2D gaussian with a FWHM of 0.148 nm, was used to align the 49 images by applying a cross-correlation algorithm before averaging them into a resulting final image.

The size of the 2D gaussian reference image plays an important role in the cross-correlation process. To determine the proper FWHM of the 2D gaussian reference image, experimental images were cross-correlated to two different 2D gaussian images, one known to be too wide and another known to be too narrow (in this case, FWHMs of 0.08 and 0.20 nm for narrow and wide, respectively), and then the resulting cross-correlated image was used as the new reference image for the next iteration. After 2–3 cycles of iterative cross-correlation, the measured FWHMs of the cross-correlated images converged to stable values. An illustration of this process for the Day II experiments is shown below in Figure 4.4, obtaining references for Sr K, Sr L, and Ti K spectrum images (owing to the high noise level of Ti L maps, the cross-correlation of Ti L data was synchronized to the Ti K cross-correlation alignment for each experiment).

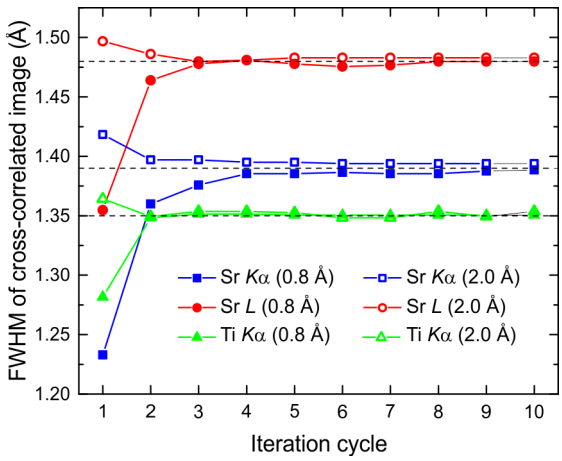

Figure 4.4: Iteration of cross-correlation process of experimental XEDS maps from Day II to determine a proper size of the reference image. The first cycle of each cross-correlation sequence was done using a 2D gaussian image with FHWM of 0.08 nm (solid) and 0.20 nm (open). Converged FWHM reference values are indicated by horizontal dotted lines for each case: Ti K (0.135 nm), Sr K (0.139 nm), and Sr L (0.148 nm) for the XEDS maps.

The resulting set of cross-correlated maps from each experiment is presented in Figure 4.5. Even at this stage, differences between K and L maps are visible, as for each element the L map is systematically wider than the K map. The subtle observed

differences between Sr K and L maps are novel. However, observations of the Ti L map exhibiting wider peaks than the Ti K in ⟨001⟩-oriented STO have independently been reported by others previously, [72] strengthening confidence in these observations.

As discussed previously, K and L XEDS maps from the same atom (whether Sr or Ti) differ because K emission results from excitations of 1s core-level electrons by the incident STEM probe to available states above the Fermi energy, whereas L emission results from excitations of 2p core-level electrons. These excitations are followed by X-ray-emitting electron relaxations to fill the newly available core-level states (2p to 1s and 3s/3d to 2p for K and L X-rays, respectively), with emission being isotropic. The localization of these orbital-characteristic X-rays is therefore constrained by the spatial extent of the core-level electron orbitals, with additional broadening due to the physics of coulombic beam-orbital interaction which is often termed as the impact parameter effect. [76] The complex nature of the beam-orbital interaction producing electronic excitations from core levels has been discussed in the literature [77–79] and is modeled in STEM-XEDS simulation software. [80] Since this quantum mechanical beam-orbital interaction is the actual experimental measurement, the imaging of orbitals by STEM-XEDS includes broadening due to the coulombic nature of this interaction.

4.3.2 Theoretical framework for XEDS spectrum imaging

Two factors should be taken into account to understand why distinction between 1s and 2p orbitals is possible in STEM-XEDS experiments with a scanning probe ~100 pm wide, when even with the thermal vibrations of atoms by phonon modes of the crystal (the 3D room temperature root-mean-square atomic displacements are 8 pm and 6 pm for Sr and Ti atoms, respectively [75]) the effective extent of the orbitals is only 20–50 pm. The first factor, which is non-obvious but critical, is the interaction of the STEM beam with the orbitals. As an electron beam propagates through a crystal, it channels along atomic columns. [52, 53] In addition to this well-known on-column channeling, when a focused STEM beam is placed slightly off of an atomic column,

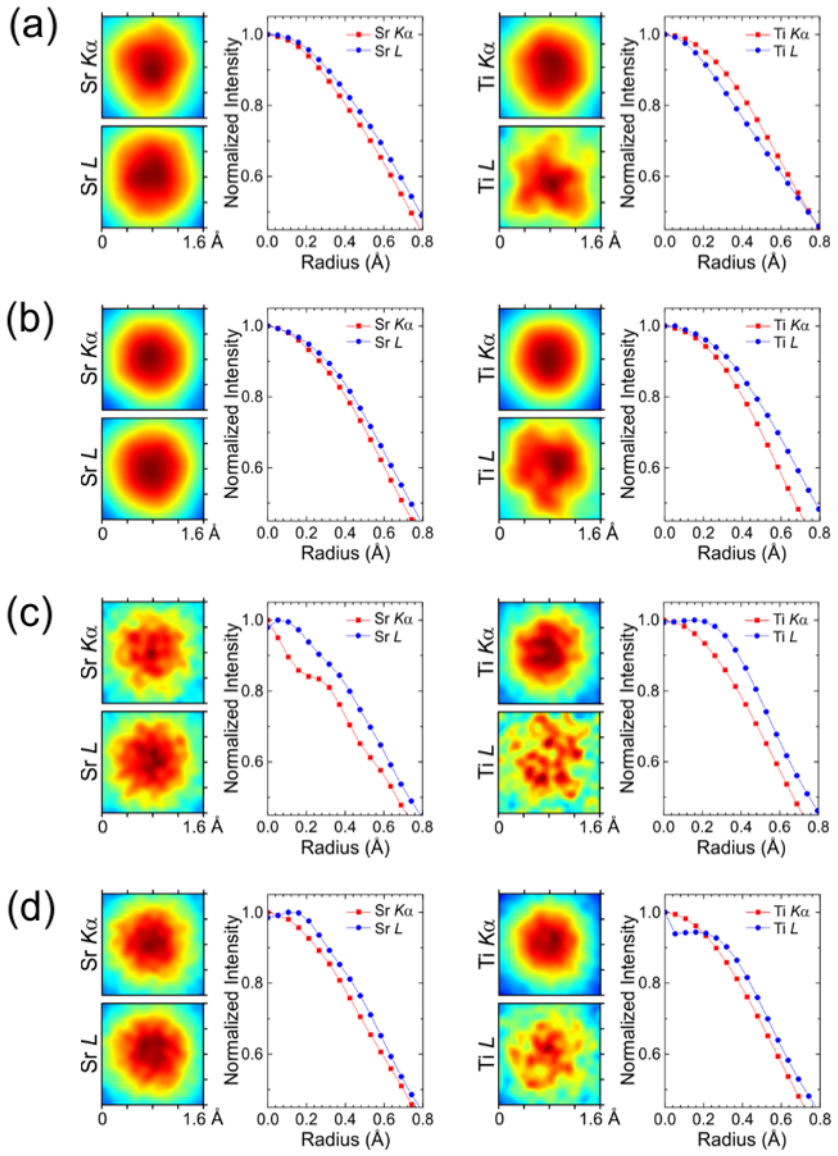

Figure 4.5: (Individual Sr K and L XEDS maps from the Sr column of STO viewed along a ⟨001⟩ crystallographic direction alongside individual Ti K and L XEDS maps from the Ti/O column of STO viewed along the same direction for four independent data sets: (a) Day I, (b) Day II-128, (c) Day II-256, and (d) Day III. Azimuthally averaged radial profiles presented at right show that for each atom the L map is wider than the K map. These maps constitute the cross-correlated average of data from approximately 300–600 identical atomic columns each, with all maps obtained simultaneously.

it propagates by first shifting into the atomic column and then channeling along the column. [81, 82] However, a closer look at the propagation of beams located just off of an atomic column shows that while they propagate along the atomic column, they oscillate back and forth within the dimension of the atom along the column. This strong localization of off-column beams prior to dechanneling is the main reason why electron beams initially positioned outside of the core-level orbital coverage area can still produce strong characteristic K and L X-ray signals. This beam behavior is illustrated for a Sr column in STO, showing snapshots of the depth-varying intensity of an aberration-corrected STEM probe placed 40 pm away from the column (Figure 4.6).

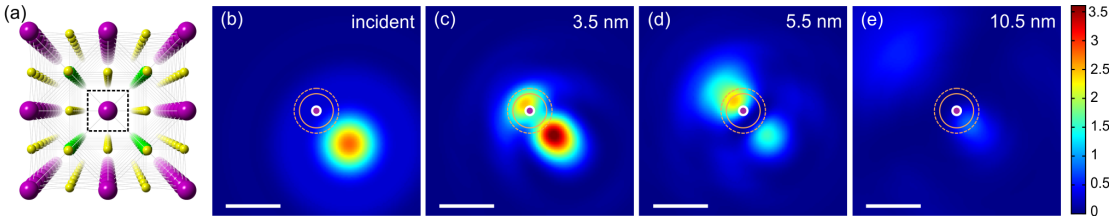

Figure 4.6: (a) Perspective rendering of a ball-and-stick atomic model of the STO crystal viewed along a ⟨001⟩ direction. Sr atoms are in purple, Ti are in green, and O are in yellow. The square box around the Sr atomic column drawn by the dashed line indicates the area considered in channeling simulations. (b)-(e) Simulated intensities of a STEM beam located 40 pm away from the Sr atomic column at depths of 0.0, 3.5, 5.5, and 10.5 nm in the crystal. The position of the Sr column is indicated by the purple dot and the extents of both 1s and 2p orbitals are highlighted by the solid and dashed orange circles, respectively. As the probe propagates through the crystal it is drawn onto the Sr atomic column and oscillates inside the column atoms, intensifying the overlap with core-level orbitals. The thermal vibrations of atoms are taken into account. The scale bar is 50 pm in length.

This is a general phenomenon that can be observed in any crystal around any atomic columns, regardless of incident beam size. However, the intensity and frequency of oscillations depends on crystal structure, atomic column composition, and STEM beam parameters. Examples of this occurring in STO with various beam sizes are also obtained (Figure 4.7); they show that STEM beams with different sizes differ quantitatively in their channeling behavior, but the overall effects are qualitatively the same. For each

of the three aberration-corrected STEM probes examined, similar channeling behavior was observed: (1) for probe positions within 20 pm of the column, the probe basically is on the column and stays on the column; (2) for probe positions 20–100 pm from the column the probe focuses to the column and laterally oscillates predominantly within the dimensions of the atom, producing subatomic channeling; and (3) for probe positions farther than 100 pm from the column, the probe does not sustain significant coupling to the column and spreads freely through the crystal. Since subatomic channeling primarily occurs in the first 20 nm of the STO crystal, the overall effect of sample thickness uncertainty is weak beyond this thickness.

The second factor that affects the visibility of the different orbitals is the aforementioned orbital excitation broadening due to coulombic beam-orbital interaction. Because the binding energies of the core-level orbitals examined in this study vary by more than an order of magnitude (from less than 0.5 keV for Ti 2p electrons to 16 keV for Sr 1s electrons), there is an additional broadening of orbitals in XEDS mapping that is inversely proportional to the electron binding energy of that orbital. This effect can be theoretically predicted from first-principles excitation calculations. [76, 78] For comparison, the first-principles excitation potential in the local approximation was calculated for 300 keV electrons using the Melbourne University μSTEM code, [80] and compared to projected charge densities calculated using the PBE-GGA functional [83] in the Quantum ESPRESSO software [84] in Figure 4.8.

4.3.3 Deconvolution of probe effects from XEDS spectrum images

In aberration-corrected STEM the incident electron beam is determined by the combined effects of diffraction, the geometrical and chromatic aberrations of the lenses, and the finite demagnified source size. Detailed analysis, based on measured values of aberration coefficients, indicates that experiment used probes had a FWHM of $d_p \approx 45$ pm; the effective source size in the specimen plane, the FWHM d_{ss} of a gaussian source

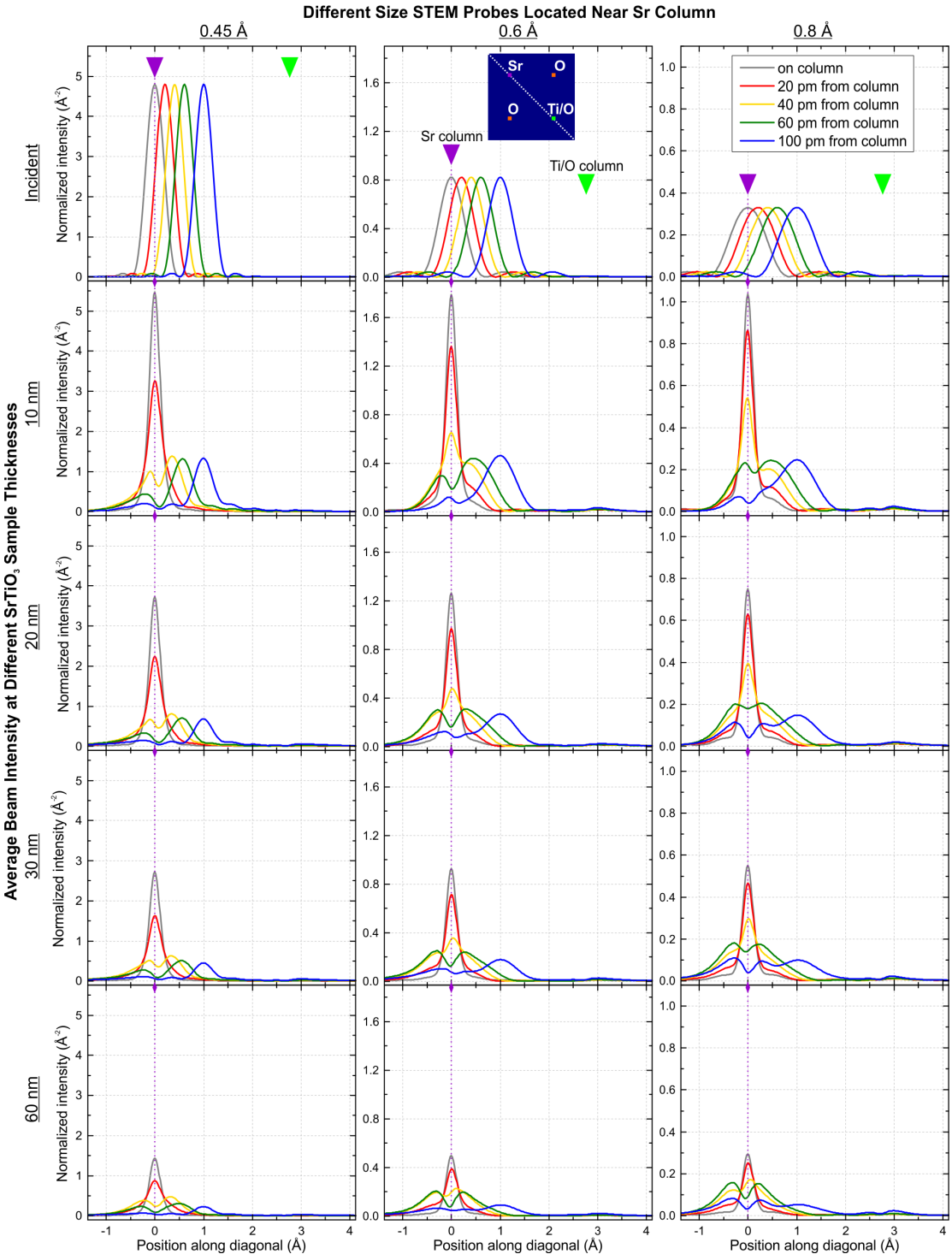

Figure 4.7: Linescans of the depth-averaged probe intensity for three STEM probes of varying size in the vicinity of the Sr column. The linescan direction within the STO crystal is indicated by a white dashed line in the inset.

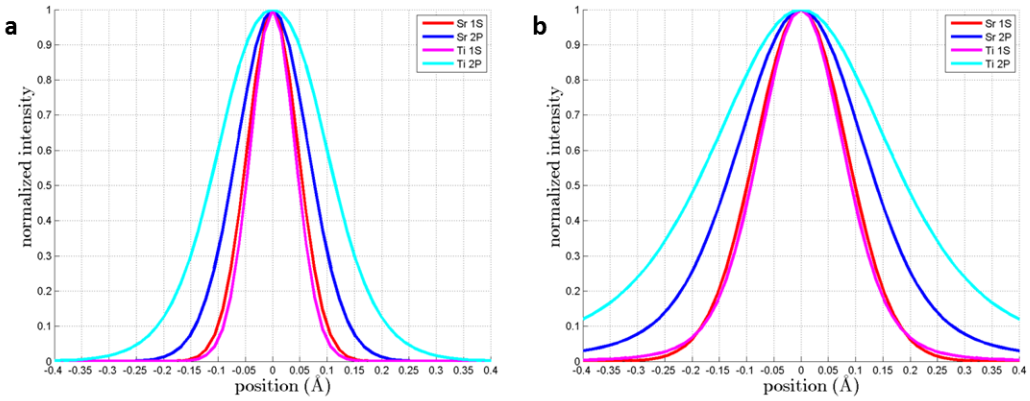

Figure 4.8: Comparison of Sr 1s, Sr 2p, Ti 1s, and Ti 2p orbitals. (a) Simple projected charge density approximation and (b) first-principles excitation potential in the local approximation for 300 keV incident electrons.

function, was inferred from comparing HAADF-STEM experimental images to multi-slice simulations as 110, 90, and 120 pm for Days I, II, and III, respectively. The effects of source size on STEM-XEDS maps and HAADF-STEM images can be taken into account as a simple convolution of the source distribution with the optical probe image, producing probes plotted in Figure 4.9.

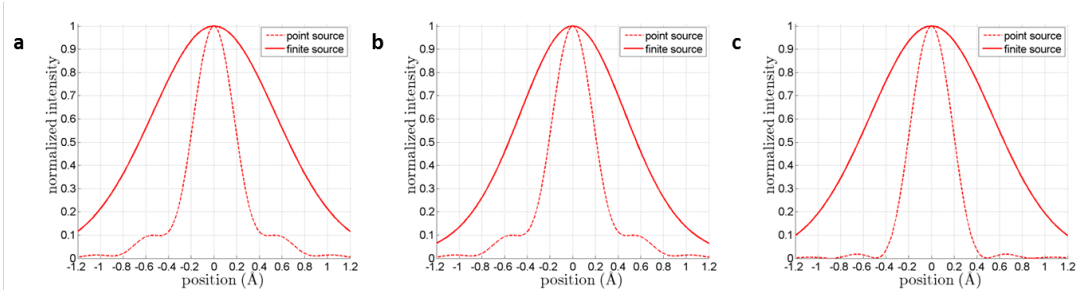

Figure 4.9: Linescans of probes with and without finite source size used to model each experiment. (a) Day I: $d_p = 45$ pm, $d_{ss} = 110$ pm, (b) Day II: $d_p = 45$ pm, $d_{ss} = 90$ pm, and (c) Day III: $d_p = 45$ pm, $d_{ss} = 120$ pm.

Deconvolution of estimated gaussian source distributions from experimental XEDS maps must be performed with care. Unlike standard FFT-based forward convolution,

numerically the inverse of the convolution operation (standard FFT-based deconvolution) is not stable here, necessitating use of the iterative Richardson-Lucy method. [85] Prior to deconvolution of the estimated source distribution, experimental spectra were blurred with a 2D gaussian function with FWHM 0.02 nm, interpolated to 256×256 points per unit cell, and low-pass-filtered to 20 nm^{-1}. Deconvolution of estimated source distributions was performed using an accelerated Richardson-Lucy algorithm [86] with damping [87], implemented in MATLAB (convergence to a solution occurred with a clear, well-behaved maximum within 500 iterations). Solutions were subsequently reconvolved (now using standard FFT-based forward convolution) with the source size to ensure correctness of the deconvolution result. Figure 4.10 illustrates the process of source size removal, source size restoration, and error-checking to confirm the correctness of the source deconvolution.

Simulations of beam behavior were performed using the best-fitting probe parameters, and XEDS mapping was performed by calculating the depth-integrated overlap of the probe intensity with the core-electron excitation potential corresponding to a given characteristic X-ray peak. [77] Simulated XEDS maps were calculated using a 32×32 sampling of probe positions across the cubic unit cell, being interpolated up to 256×256 points per unit cell using a cubic spline routine for all data processing and analysis. The source-deconvolved XEDS maps could be directly compared to the point-source simulations.

Experimental measurements of core-level excitation potentials can be determined by deconvolving channeled STEM probes from source-removed experimental XEDS maps, a notion that had previously been discussed by others. [88] The XEDS intensity for a given probe position can be evaluated as the convolution of depth-integrated channeling intensity for that probe position with the orbital excitation potential. In the case of beam propagation calculations for 32×32 probe positions across the unit cell, sampling both the object and depth-integrated probe intensity using 256×256 pixels per unit cell grid using multislice code. Deducing the excitation potentials producing XEDS maps

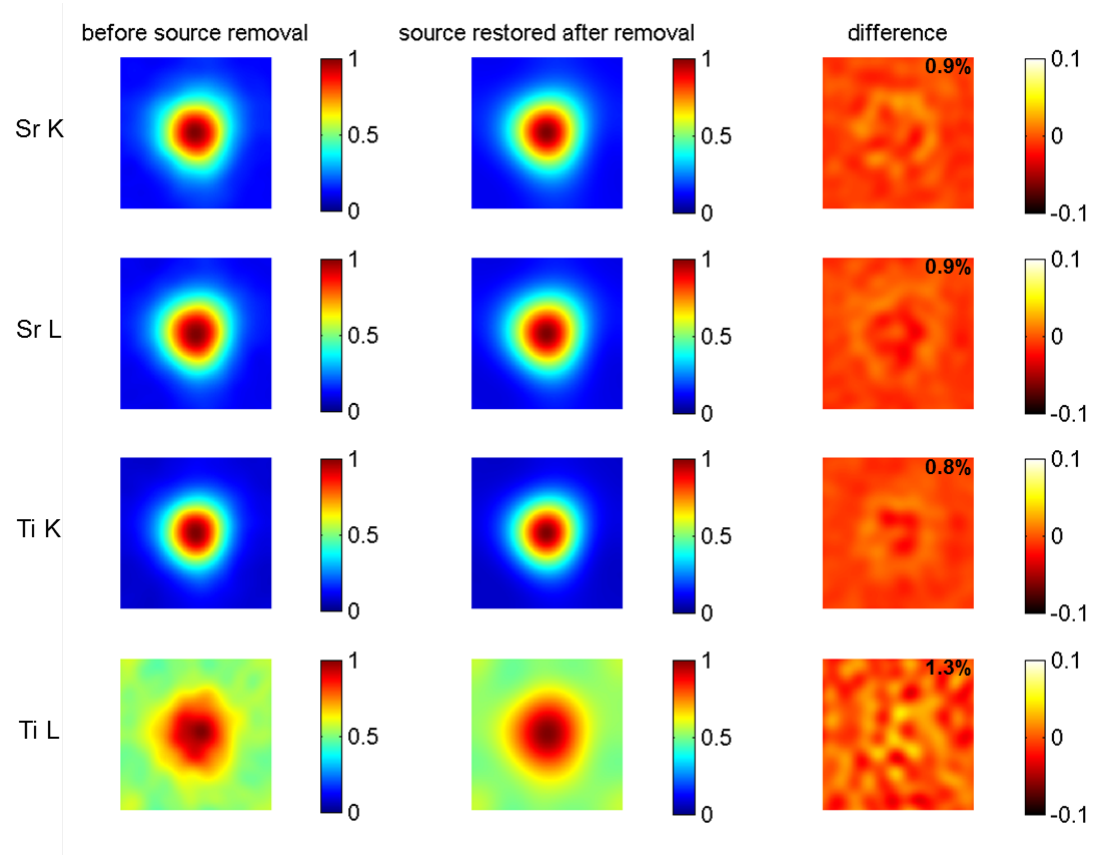

Figure 4.10: Source-size removal for Day II-128 images, left to right: experimental XEDS maps (processed as discussed), maps formed by restoring source distribution to source-removed data, and the difference between the two. Difference plots (root-mean-square difference given in top right corner of each difference map) illustrate successful source-size removal by the Richardson-Lucy method. All plots span 11 u.c.^{2} in area.

then requires solving the system of equations of Equation 4.1:

$$O(i,j) \otimes P(i,k,j,l) = X(k,l) \tag{4.1}$$

where $O(i,j)$ is the 2D orbital projection on the discrete unit cell grid (i,j), $P(i,k,j,l)$ is the 4D channeled probe array for a given thickness, and $X(k,l)$ is the experimentally measured source-removed XEDS map at each probe position (k,l). Here $\otimes$ denotes a 2D convolution operation over (i,j). In the conditions used in this study, this amounts to solving an underconstrained linear system: using simulated probe data $P(i,k,j,l)$ (known intensities depth-integrated at each of the 65536 sample points, for each of the 1024 probe positions) and known source-removed experimental spectrum image data (known intensities for each of the 1024 probe positions), the excitation potential for each orbital (unknown value for all of the 65536 sample points) can be determined.

This problem can be "unbiasedly" solved by inverting the system to solve for the potential using methods such as the Moore-Penrose pseudoinverse [89] or conjugate-gradient-type LSQR [90] algorithms. However, due to instability (i.e., non-convergence) of these solution types they were abandoned in favor of a simpler, if more overtly biased, approach: using trial solutions with a physically sensible form. Both projected orbitals and first-principles local excitation potentials can be approximated by lorentzian fits, so this is one form of trial solution that can be justifiably used. Similarly, both Moore-Penrose and LSQR methods yield lorentzian-like solutions at intermediate tolerance levels, motivating the examination of lorentzian trial solutions; because thermal vibrations in the solid have approximately gaussian distribution, trial solutions were lorentzians that were first convolved with gaussians corresponding to their RMS thermal vibrations to generate lorentzian-form trial solutions (e.g., a 10 pm lorentzian trial solution for the Sr column is a lorentzian with FWHM 10 pm convolved with a gaussian of standard deviation 4.5 pm).

As implied by the above discussion, the fitness of a solution is conventionally determined by the average square error, often represented as the root-mean-square error (RMSE). For any image $I(i,j)$ fitted by a function $F(i,j)$, both discretely sampled over a number of positions $n \times m$, the RMSE is defined in Equation 4.2:

$$RMSE = \sqrt{\frac{\sum_{i=1}^{n}\sum_{j=1}^{m}\left[F(i,j) - I(i,j)\right]^2}{n \times m}} \tag{4.2}$$

Minimizing RMSE, either in (a) comparing point-source reconstructed images to experimental source-removed images or (b) comparing finite-source reconstructed images to source-inclusive experimental images, is the most straightforward objective measure for a "best-fit" solution. Because any constant offset in experimental data vis-a-vis reconstructed image data can corrupt the RMSE minimum (i.e., due to systematic background in the data), all images were background-subtracted before comparison. Because RMSE between experimental and reconstructed images is more sensitive to object size for point-source than finite-source comparisons, best-fit determinations were made by comparing point-source reconstructed images to their source-removed, background-subtracted experimental counterparts.

Final best fits for all experiments are compared alongside theoretical predictions in Figure 4.11. Measured orbital sizes vary slightly across experiments, serving as a measure of significant experimental uncertainty due to uncertainty in the measured parameters of the STEM beam and unavoidable minor electron-beam-damage of specimen, and approximation-induced error in beam channeling simulations and theoretical calculations of excitation broadening.

Not only are the overall sizes of the experimentally measured transition potentials for each orbital in good agreement with predictions, but also those for 1s orbitals are systematically smaller in size than for 2p orbitals for both Sr and Ti atoms for all experiments. It should be noted that having a high signal-to-noise ratio in the original

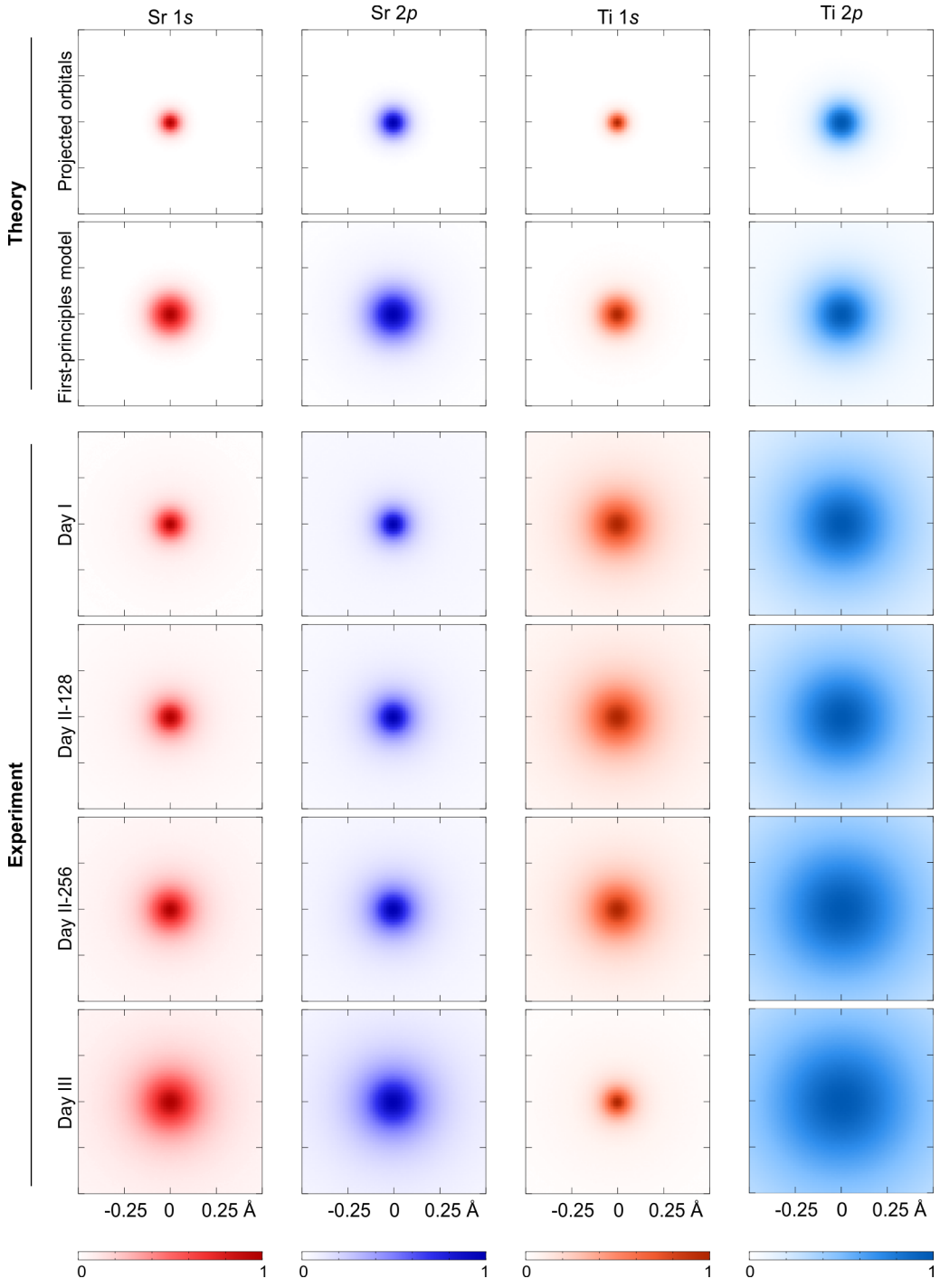

Figure 4.11: Comparison of projected orbital theory with best-fitting lorentzian trial solution determined from each experiment. All best fits were determined from background-subtracted point-source comparisons.

XEDS maps (which was substantially further improved by cross-correlation) is the essential factor allowing for distinction of small size differences between 1s and 2p orbitals (10 and 40 pm for Sr and Ti, respectively), going beyond the conventionally defined resolution of the STEM. Similar statistically driven enhancement of resolution is often practiced, and has been demonstrated for ADF-STEM imaging. [91]

4.3.4 Measurement of impact parameters using XEDS spectrum images

Taking the analysis one step further, these experimental results are used to measure impact parameters of the core level electronic excitations responsible for X-ray generation. The impact parameter, or delocalization of the excitations beyond the extent of the initial state, is determined by the range of non-vanishing values of the square of the electronic transition matrix element due to the coulombic beam-orbital interaction. The impact parameter effect can be seen in the plots of Figure 4.12, where both first-principles potential calculations and experimental potential measurements are broadened beyond the extent of the initial core orbital state.

The magnitude of the impact parameter can be estimated by evaluating differences between the radii of measured projected transition potentials $r_{potential}$ and those of the exact projected charge densities of core orbitals $r_{orbital}$: $\Delta = r_{potential} - r_{orbital}$. The analysis based on all four individual measurements is presented in Figure 4.13 and the results are compared to theoretical predictions. The data indicates that for core orbitals with a rather wide range of binding energies (0.4–16 keV) the electronic excitation impact parameter is $\leq$10 pm. For orbitals with binding energies smaller than 2 keV, impact parameters increase but are still smaller than 40 pm down to 0.4 keV. Due to unreliable separation of Ti L and O K XEDS signals, the latter measure is likely an extreme upper bound, as also suggested by the large gap between the experimental and first-principles impact parameters.

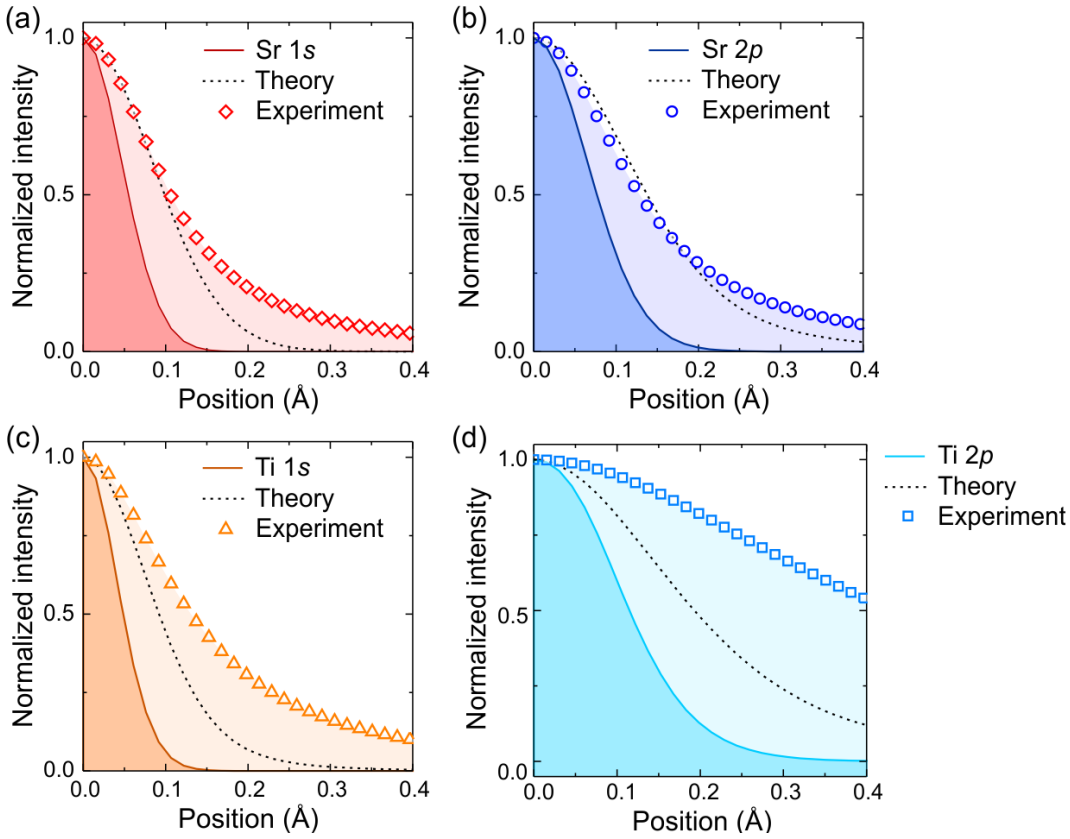

Figure 4.12: Comparison of the radial distribution of experimentally observed and calculated transition potentials, alongside calculated projected charge densities, for (a) Sr 1s, (b) Sr 2p, (c) Ti 1s, and (d) Ti 2p orbitals. All sets of theoretical calculations include the effects of atomic thermal vibrations. Calculations with excitation broadening are indicated by dashed black lines and those without excitation broadening by solid colored lines.

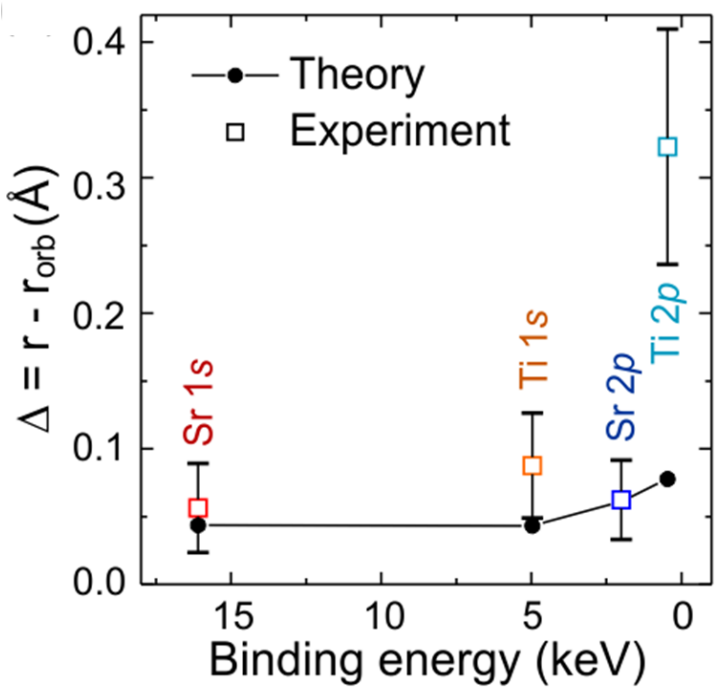

Figure 4.13: Comparison of experimentally measured and theoretically predicted impact parameters. Experimental measures correspond to the average of all four independent experiments, with error bars corresponding to one standard deviation of the data for each orbital.

4.4 Conclusion

It has been shown that by recording XEDS maps from crystalline specimens using an aberration-corrected STEM equipped with a high-efficiency X-ray detection system, it is ultimately possible to extract a broadened real-space measurement of core-level electron orbitals. In the case of STO both the 1s and 2p orbitals of Sr and Ti atoms are visualized; as expected, 1s orbitals are always smaller than 2p orbitals, and all orbitals are localized on their respective atomic columns. This method should be applicable to any atomic columns in any crystal, and it is limited only by uncertainties in experimental parameters, as well as by the rate of X-ray collection relative to electron-beam damage of the specimen. We also have shown that these experiments allow measurements of the electronic excitation impact parameters due to coulombic beam-orbital interaction, which at 300 keV were found to range from around 10 pm for deeply bound Sr 1s, Ti 1s, and Sr 2p orbitals, to less than 40 pm for more weakly bound Ti 2p core orbitals.

Availability of a STEM with a high-brightness gun and aberration correction is desirable for such experiments, because minimizing effective probe size optimizes the resolution and contrast of XEDS maps. Operation of a STEM at lower beam energies has potential to improve the method, as the probability of ionization will increase and knock-on damage can be reduced or eliminated; however, this comes at the cost of probe size increasing at lower beam energy, thinner specimens being required, and radiolytic damage rate increasing. As an extension of this work, it should be also possible to probe core-level electron orbitals and measure impact parameters using core-loss EELS mapping in an aberration-corrected STEM, provided that a large collection aperture is used (to ensure a well-localized transition potential) [79] and that the core-loss EELS signal is treated with reliable background-subtraction.

It can be anticipated that the results and approach presented here will prove useful in several different ways, two of which seem most straightforward. One way is in demonstrating a precision of electron-beam-based spectroscopy which is limited only

by the impact parameter of excitation. Another is by describing the means for improving the spatial localization of elemental composition measurements using STEM-XEDS, which should also be applicable for the analysis of any well-localized spectroscopy: if the elastic scattering behavior of the beam can be calculated with confidence, the effects of channeling and beam spreading can be inverted to produce a true map of chemical composition or electronic states.

Chapter 5

Computational predictions of bonding effects for ADF-STEM imaging

5.1 Introduction

Conventional implementations of multislice [13] transmission electron microscopy (TEM) image simulation [73, 74] model the electrostatic potential of a solid as that of a collection of unbonded neutral atoms; this approximation is known as the independent atom model (IAM). It is known that failure to account for bonding introduces significant errors in calculations of low-angle electron scattering, [92] accounting for the power of quantitative convergent-beam electron diffraction (CBED) for valence charge density determination.

Among these modes the high-angle ADF (HAADF) variant of ADF-STEM is especially interesting, being an approximately incoherent imaging mode wherein image intensity originates from the high-angle scattering of fast electrons from positively-charged atomic ion cores. [6, 93] The primary advantages of HAADF-STEM imaging are robust

direct proportionality between HAADF-STEM image intensity and the mass-thickness of the specimen, [94] as well as the possibility of efficient parallel electron-energy-loss spectroscopy (EELS) of the electrons transmitted past the detector. Advances in electron optics for aberration correction [11, 12] allow HAADF-STEM imaging with sub-angstrom resolution, readily resolving very narrowly spaced atomic columns. [95, 96] Such imaging is widely regarded as insensitive to bonding because valence charge redistribution should not alter the high-angle scattering of probe electrons.

For a STEM probe placed near an atomic column, beam intensity focuses onto the column and oscillates with depth, an effect known as channeling. [52, 53] Simulations show that on-column channeled intensity can be highly sensitive to atomic number (Z), crystal orientation, and imaging conditions. [97] Careful analysis of ADF-STEM image simulation further shows that both on-column channeling and inter-column beam spreading determine the thickness-dependent image contrast in zone-axis-oriented crystals. [98–100] Although challenging to measure, both on-column channeling [101] and inter-column beam spreading [82] have been characterized experimentally in zone-axis-oriented crystals. The coherent low-angle scattering that determines channeling and beam-spreading behavior is known to be bonding-sensitive, but this dependence has not been examined explicitly.

Including valence charge redistribution due to bonding may change both the propagation of a focused electron beam through the sample and the strength of high-angle scattering from individual atoms in the column, both of which ultimately affect ADF-STEM image contrast. To begin understanding the effect of bonding on the ADF-STEM imaging of crystals, this study surveys the effects of bonding model, atomic composition, incident probe, detector geometry, and thermal vibrations in bonding-inclusive multislice simulations. The results of the study not only refine the analysis of ADF-STEM imaging of perfect single crystals, but also point toward an approach for simulating imaging of defects that locally distort the bonding states of atoms, such as ordered point defects [102] and interfaces [103] in ceramic materials.

5.2 Methods

HAADF-STEM images of light-element single crystals were simulated using the multislice method as implemented by the TEMSIM code [14] developed by Earl Kirkland and coworkers. The crystals studied were diamond carbon (d-C), cubic boron nitride (c-BN), wurtzite boron nitride (w-BN), wurtzite aluminum nitride (AlN), wurtzite beryllium oxide (BeO), halite magnesium oxide (MgO), halite lithium fluoride (LiF), and halite sodium fluoride (NaF). These materials were chosen to compare bonding effects across differences in crystal structure, bond length, bond polarity, and bond valency, surveyed in Table 5.1.

PROPERTY	**d-C**	**c-BN**	**w-BN**	**AlN**	**BeO**	**MgO**	**LiF**	**NaF**
Crystal structure	diamond	zincblende	wurtzite	wurtzite	wurtzite	halite	halite	halite
Bond length (nm)	0.154	0.156	0.157	0.190	0.165	0.209	0.202	0.230
Pauling ΔX	0.00	1.00	1.00	1.43	1.87	2.13	3.00	3.05
Formal valency	0	+/3	+/3	+/3	+/2	+/2	+/1	+/1

Table 5.1: Comparison of the crystal structure, bond length, bond polarity, and bond valency of the crystals studied. Crystals increase in bond polarity from left to right.

To determine the effects of bonding using computational methods, three different bonding models were used: the independent atom model (IAM), the bonded crystal model (BCM), and the fully ionized model (FIM). In IAM, the charge density of the solid was calculated as the superposition of the charge densities of independent neutral atoms. In BCM, the charge density of the solid was calculated as the superposition of atomic ion-core charge densities with valence charge densities calculated by density functional theory (DFT). In FIM, the charge density of the solid was calculated as the superposition of the charge densities of independent full-valence-shell ions. The charge density and projected potential of each of the models is simplistically illustrated in Figure 5.1.

Although it is BCM that expressly emulates the bonding of real solids, it is instructive to compare it to the hypothetical extremes of non-existent (IAM) and complete (FIM) charge transfer. Consideration of these extremes is also motivated by the fact

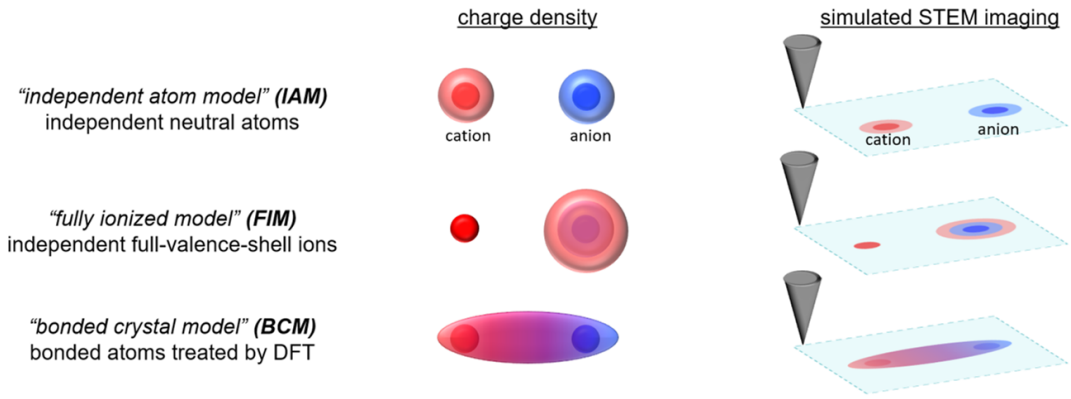

Figure 5.1: Schematics of image simulation using different bonding models. Dark-colored regions indicate contributions of atomic ion cores (nucleus plus all non-valence electrons). Light-colored volumes indicate contributions of the valence electrons of a neutral atom.

that the bonding at crystal defects may either increase or decrease the degree of bonding-induced charge transfer relative to the bulk, causing the bonding to locally veer away from bulk BCM character toward something more like either bulk FIM or bulk IAM. Because IAM is the standard mode of simulation, it has been treated as the reference against which the other models are compared.

All charge densities were calculated using the Quantum Espresso [84] DFT software package. Single-atom charge density calculations (used for core orbital charge densities of all models, as well as valence charge densities of both IAM and FIM) were performed on a 2000-point logarithmic radial grid out to 0.5 nm, using the PBE-GGA [83] functional. Valence charge density calculations for the BCM model were performed using the LDA [104] functional.

To produce inputs for multislice simulation, unit cell charge densities were transformed to electrostatic potentials using periodic boundary conditions, [105] sectioned into slices centered on atomic planes, and integrated over slice thickness to produce exact projected potentials that could serve as inputs for multislice simulations without thermal diffuse scattering (TDS); this method also allowed direct investigation of the

effects of slice thickness on the accuracy of beam propagation calculations (A). To perform TDS-inclusive calculations, the exact projected potentials were approximately parameterized as sums of radially symmetric gaussians and Bessel functions of the first kind, [14] allowing on-the-fly calculation of frozen-phonon configurations by TEMSIM for each bonding model. To ensure accurate TDS-inclusive simulations, RMS thermal vibration values were determined from the experimental diffraction literature.

Crystals were analyzed at zone axes with each column containing only one type of atom ($\langle 100 \rangle$ for diamond cubic crystals, $\langle 110 \rangle$ for halite cubic, and $\langle \bar{2}110 \rangle$ for wurtzite crystals). Probe and transmission functions were each calculated on a 1024×1024 pixel grid, with supercell edge lengths varying over 2.29–4.35 nm across all of the materials studied. Probe energies ranging 60–200 keV, convergence semi-angles ranging 15–35 mrad, ADF detector inner angles ranging 40–200 mrad (default HAADF detector geometry used a 60 mrad inner angle and 200 mrad outer angle, but other combinations of inner and outer angles were also studied), and material temperatures 0–300 K were all considered in examining the effects of bonding on ADF-STEM imaging. For reference, the diffraction-limited resolution of each simulated probe is listed in Table 5.2, calculated according to the Rayleigh criterion.

Beam Energy (keV)	**15 mrad (nm)**	**25 mrad (nm)**	**35 mrad (nm)**
60	0.198	0.119	0.085
100	0.151	0.091	0.065
200	0.102	0.062	0.044

Table 5.2: Rayleigh criterion diffraction-limited resolution of the STEM probes considered in this study. Each value corresponds to the radius of the central Airy disk formed in each condition, which is approximately equal to the full-width-at-half-maximum (FWHM) of an aberration-free probe.

Effects of finite source size were generally neglected, and when included were calculated as the convolution of a simulated image with a two-dimensional gaussian of specified FWHM. All image intensities are represented as scattered currents normalized to the incident beam current. Channeling and beam-spreading calculations are

calculated as normalized fluxes (i.e., beam current at that pixel divided by the product of incident beam current and the pixel area; neglecting attenuation of current due to absorption, the integral of the normalized flux over the supercell area at any slice is unity).

5.3 Results and Discussion

5.3.1 HAADF imaging

Owing to its predominant selection of incoherently scattered beams and optimal complementarity to core-loss EELS, HAADF-STEM imaging is a widely used imaging mode that approximately offers simple "Z-contrast." In reality, on-column channeling, beam spreading, and TDS all significantly affect HAADF-STEM image contrast in zone-axis-oriented crystals.

To isolate the essential effect of bonding on ADF-STEM imaging, we first consider this HAADF-STEM imaging mode (where bonding should be less influential than lower-inner-angle ADF-STEM modes, due to exclusion of coherent zero-order Laue zone scattering) in the absence of TDS effects. A very useful means for analyzing thickness-dependent HAADF-STEM imaging of crystals is plotting a HAADF intensity linescan as a function of depth (henceforth termed "x-z profiles"). Plotting x-z profiles for a 100 keV probe with 25 mrad convergence in $\langle\bar{2}110\rangle$-oriented AlN (Figure 5.2) shows that bonding produces differences in intensity as a function of depth, and that this depth-evolution varies with bonding model.

Quantitative comparison of those x-z profiles (Figure 5.3) reveals significant differences between IAM and BCM simulations, and still more pronounced differences between IAM and FIM; this is readily seen both when differences are taken on an absolute scale $\Delta = I_{bonded} - I_{IAM}$ (Figure 5.3(a)) and when they are normalized to the IAM intensity value and reported as the percentage $100 \times (I_{bonded} - I_{IAM}) / I_{IAM}$ (Figure 5.3(b)). The normalized differences highlight the effect of bonding in proportion to

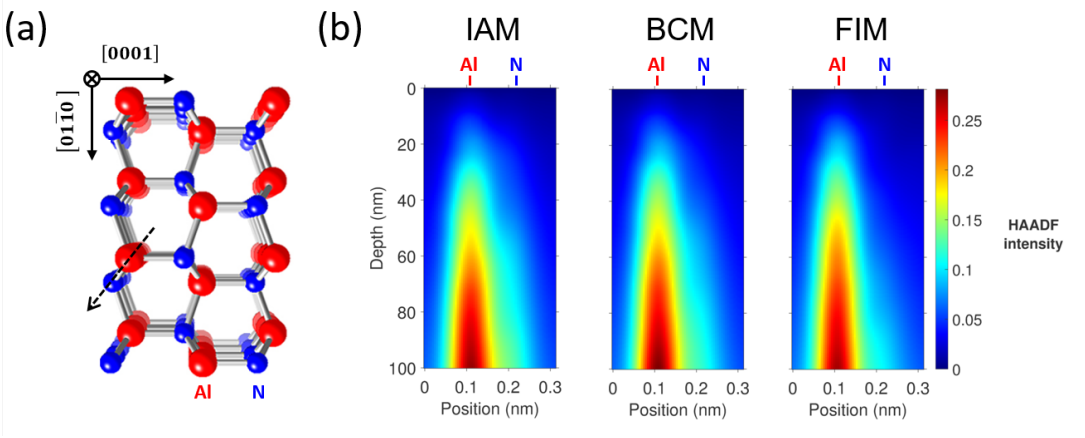

Figure 5.2: For an x-z profile of the HAADF signal along the indicated line in $\langle\bar{2}110\rangle$-oriented AlN (a), HAADF-STEM image simulations of a 25 mrad 100 keV probe using each bonding model (b) give slightly different depth-dependent contrast, most visible as a weakening of the N column shoulder as a function of increasing charge transfer.

the IAM image intensity at any thickness, and thus are used in all of the following x-z profile comparisons.

A systematic examination for a 100 keV probe with 25 mrad convergence shows clearly that both $\langle\bar{2}110\rangle$-oriented wurtzite crystals (Figure 5.4) and $\langle 110\rangle$-oriented halite crystals (Figure 5.5) have HAADF-STEM image contrast affected by polar bonding. Normalized differences are strongest in between neighboring columns but are also large on the columns themselves. In general, cation columns increase in intensity while anion columns decrease, although the B column in w-BN serves as an exception. In all cases, the magnitude of bonding effects is highly depth-sensitive. Cation signal increases were found to be as large as 10% and anion signal decreases as large as 15%, relative to IAM, for BCM models. For FIM models, the maximum changes relative to IAM were a 35% cation signal increase and a 40% anion signal decrease.

The critical effect of charge transfer on HAADF-STEM imaging can be seen more definitively by comparing BCM calculations with varying degrees of charge transfer between atoms. By artificially changing the electronic potential energy on Al in AlN,

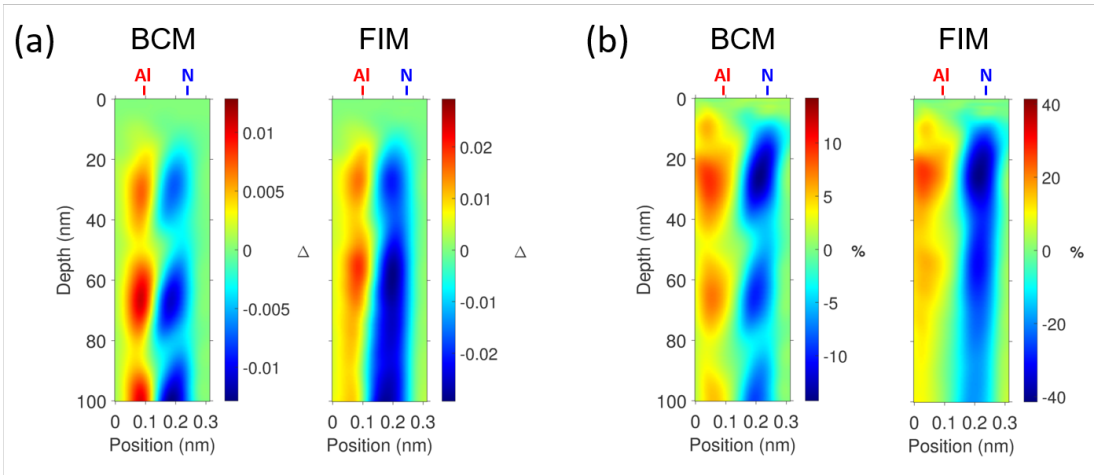

Figure 5.3: For an x-z profile of the HAADF signal along the indicated line in $\langle\bar{2}110\rangle$-oriented AlN (a), HAADF-STEM image simulations of a 25 mrad 100 keV probe using each bonding model (b) give slightly different depth-dependent contrast, most visible as a weakening of the N column shoulder as a function of increasing charge transfer.

the bond polarity can be tuned (increasing the electron potential energy on the cation increases polarity, reducing the energy reduces polarity). Normalized differences relative to the IAM reference (Figure 5.6) show that the magnitude of differences increases with increasing bond polarity, confirming that the strength of the bonding effect scales directly with the degree of net charge transfer.

For HAADF-STEM imaging, a useful parameter for characterizing depth-dependent imaging is the contrast signal as a function of depth, $C(z)$, defined here as the ratio of the HAADF intensity on a column with atomic number Z_1 to that on a column with atomic number Z_2 in a multi-element crystal with $Z_1 > Z_2$: $C(z) = I_{Z_1}(z)/I_{Z_2}(z)$. By utilizing quantitatively calibrated STEM imaging, this value can be used to analyze both computational and experimental imaging. By considering the contrast signal as a function of depth (Figure 5.7) for a 25 mrad 200 keV probe in AlN and NaF crystals, the effect of bonding model on HAADF images is captured simply.

As with x-z profiles, contrast signal comparisons benefit from normalization, showing the proportional effect of bonding relative to the IAM signal at any given depth as the

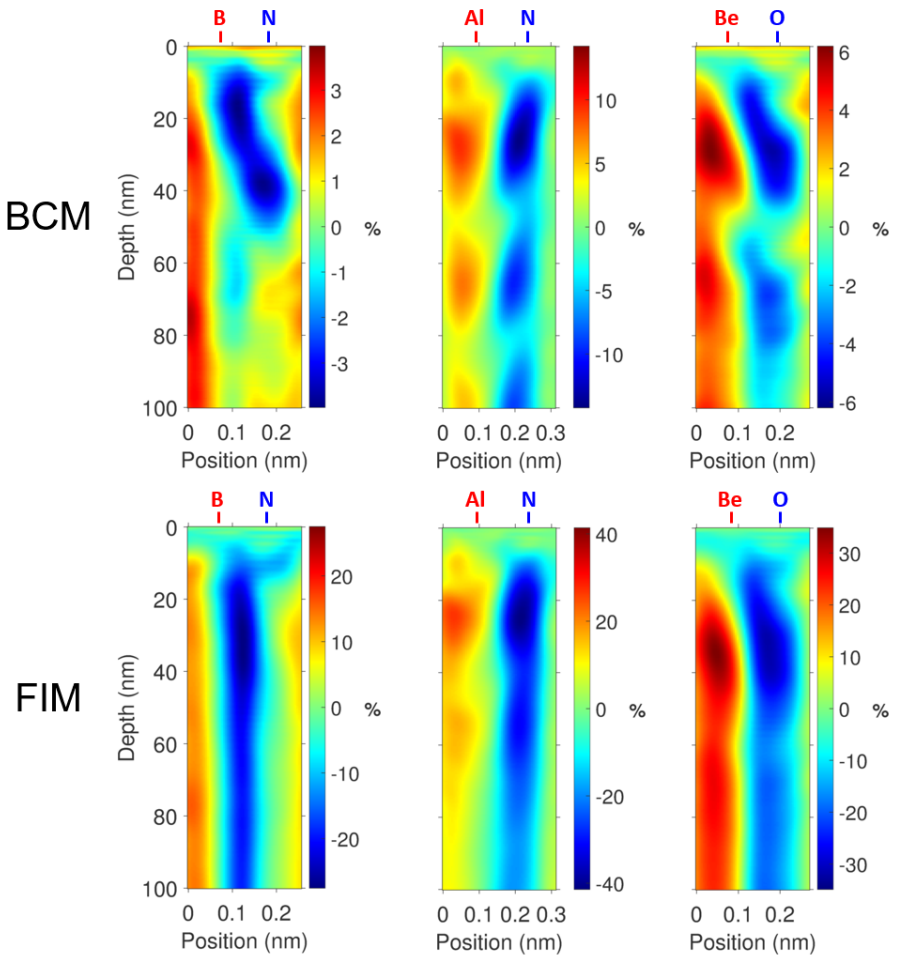

Figure 5.4: Normalized HAADF x-z profile differences of (a) BCM and (b) FIM bonding models relative to IAM reference, for $\langle\bar{2}110\rangle$-oriented wurtzite crystals. Crystals increase in polarity from left to right. BCM vs. IAM differences are weaker than FIM vs. IAM.

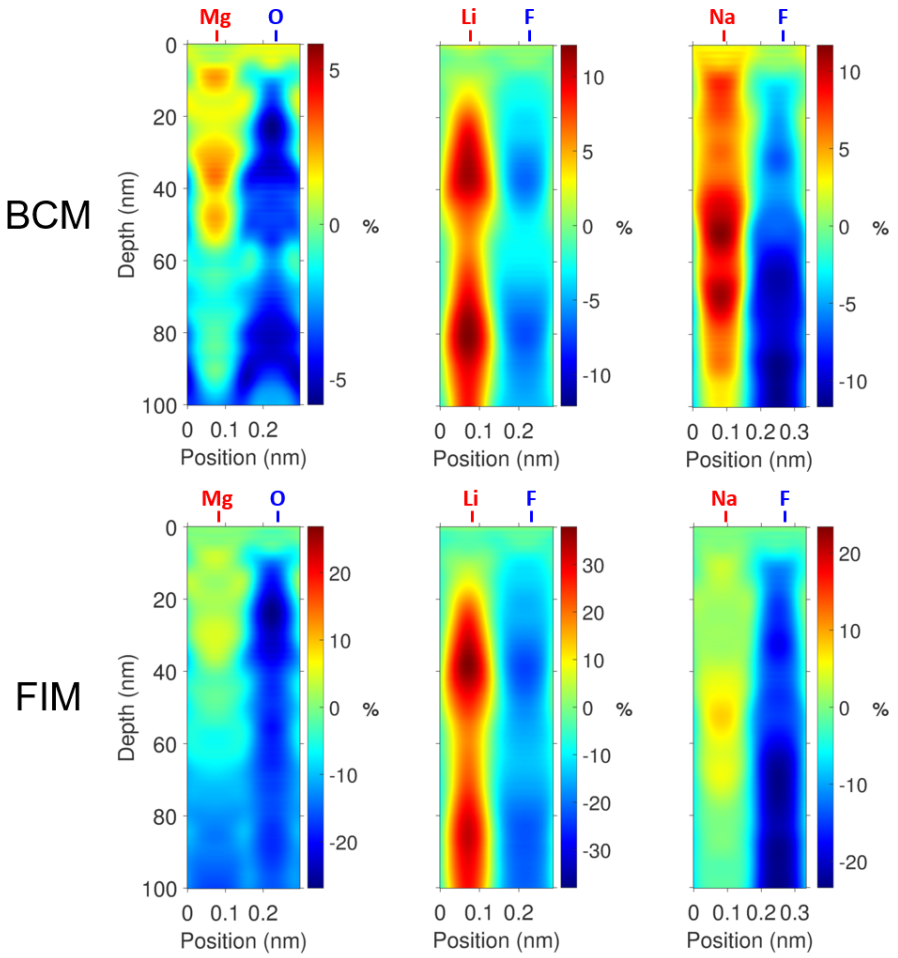

Figure 5.5: Normalized HAADF x-z profile differences of (a) BCM and (b) FIM bonding models relative to IAM reference, for ⟨110⟩-oriented halite crystals. Crystals increase in polarity from left to right. BCM vs. IAM differences are weaker than FIM vs. IAM.

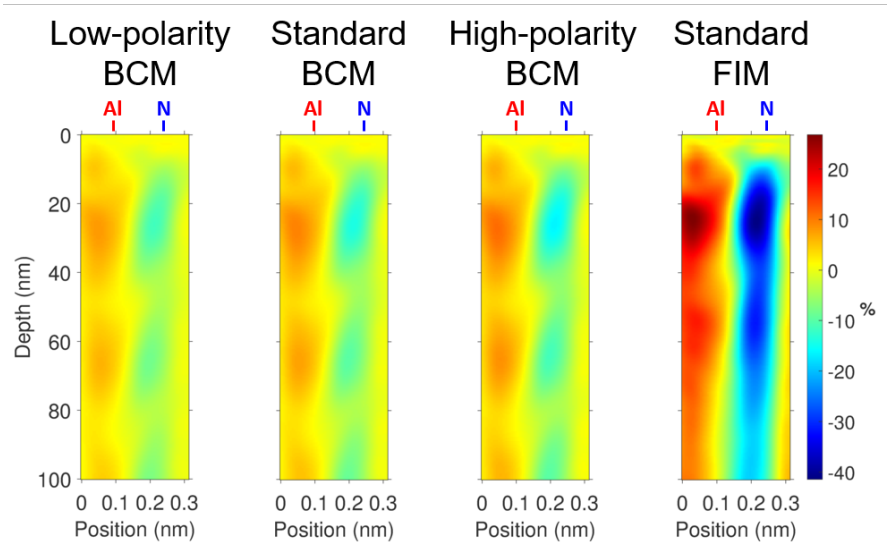

Figure 5.6: Normalized HAADF x-z profile differences for $\langle\bar{2}110\rangle$-oriented AlN with increasing charge transfer between Al and N from left to right: low polarity BCM model (electron potential energy on Al artificially lowered by 1 eV), standard BCM model, high-polarity BCM model (electron potential energy on Al artificially increased by 1 eV), and standard FIM model. As charge transfer between columns increases, normalized x-z profile differences for $\langle\bar{2}110\rangle$-oriented AlN reveal proportional strengthening of Al column intensity and weakening of N column intensity.

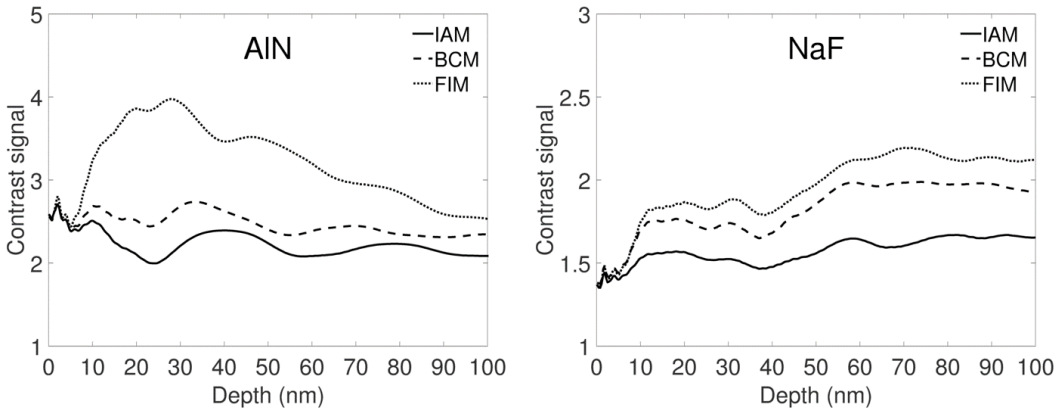

Figure 5.7: Contrast signal for a 100 keV probe with 25 mrad convergence in $\langle\bar{2}110\rangle$-oriented AlN and $\langle 110\rangle$-oriented NaF. The contrast signal varies both as a function of depth and bonding model. When the difference in Z is larger, the contrast signal is larger and varies more widely as a function of depth.

percentage $100 \times (C_{bonded} - C_{IAM})/C_{IAM}$. Normalized comparisons across six polar cystals (Figure 5.8) show that beyond a depth of 20 nm, differences of 5–25% relative to IAM are observed for BCM models, while differences range 5–90% for FIM models. The contrast signal decreases relative to the IAM model when the cation is lower in Z than the anion, whereas it increases when the cation is comparatively higher in Z. This is due to bonding-enhancement of cation column HAADF intensity and bonding-attenuation of anion column HAADF intensity.

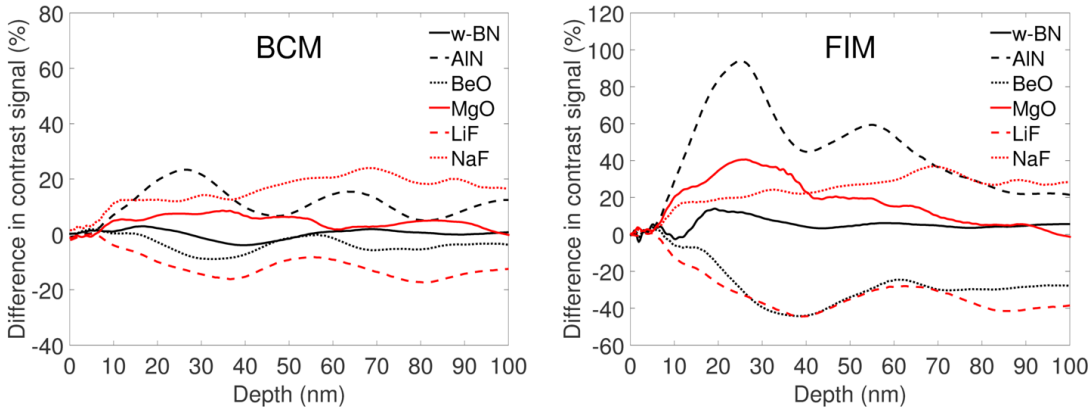

Figure 5.8: Change in HAADF contrast signal as a function of depth relative to IAM for a 100 keV probe with 25 mrad convergence. Effect of bonding on contrast is stronger for FIM model than for BCM, and in either case maximum changes in contrast ratio emerge at thicknesses of 20 nm or greater.

5.3.2 Beam propagation

In view of the depth-dependent bonding effects on HAADF-STEM imaging considered above, simulations of STEM beam propagation are informative for understanding the influence of channeling and beam spreading on image contrast. Examples of such simulations for a 100 keV probe with 25 mrad convergence centered on the N column in $\langle\bar{2}110\rangle$-oriented AlN are plotted in Figure 5.9. These plots simultaneously illustrate the fluctuation of intensity on the center N column and coupling of the beam to the

nearest-neighboring Al column 0.11 nm away. Use of a single colormap scaling highlights changes introduced by polar bonding: as charge transfer increases, the intensity on the anionic N column decreases, the interaction between N and Al columns weakens, and the frequency of intensity fluctuations between Al and N columns increases. This manner of charge-transfer-dependent interaction affects all modes of STEM imaging, including even the HAADF-STEM mode discussed above.

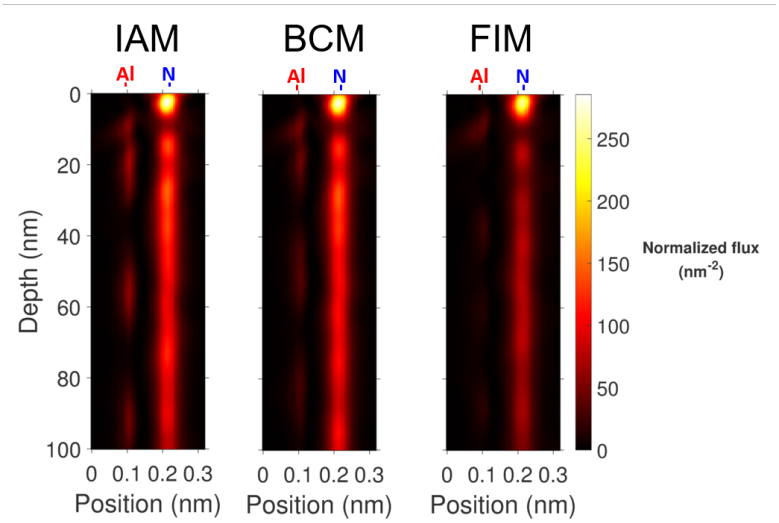

Figure 5.9: Intensity along line between nearest-neighboring columns in $\langle\bar{2}110\rangle$-oriented AlN as a function of depth, with incident 25 mrad 100 keV probe centered on the N column. Intensity fluctuates with thickness on the N column, but also couples to the neighboring Al column. Beam propagation visibly changes with bonding model.

When the probe is centered on a given atomic column, tracking the intensity on that column and its nearest neighboring columns reveals the origin of high-angle-scattered image intensity as a function of depth. [100,106] A systematic examination for a 100 keV probe with 25 mrad convergence show that $\langle\bar{2}110\rangle$-oriented wurtzite crystals (Figure 5.10), $\langle 110\rangle$-oriented halite crystals (Figure 5.11), and $\langle 100\rangle$-oriented diamond and zinc blende crystals (Figure 5.12) all have both on-column channeling behavior and inter-column beam spreading affected by polar bonding. As charge transfer increases,

all cationic columns except Be increase the frequency and strength of on-column channeling while all anionic columns decrease the frequency and strength of on-column channeling; this contributes to the change in HAADF contrast signal, with HAADF intensity increasing on cation columns and decreasing on anion columns.

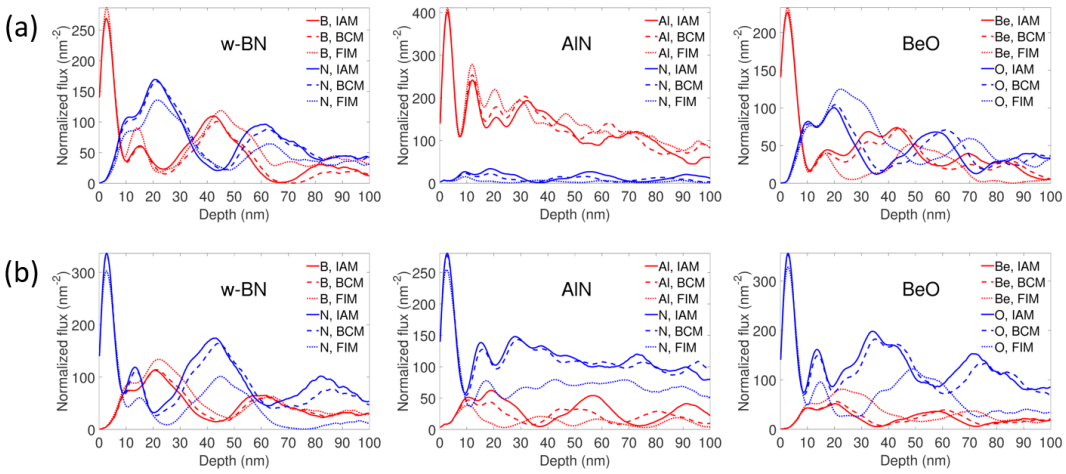

Figure 5.10: Probe intensity incident on atomic columns as a function of depth for $\langle\bar{2}110\rangle$-oriented wurtzite crystals, with incident probe centered on the (a) cation column and (b) anion column. Bond polarity increases from left to right. Intensity is tracked on incident columns, first-nearest-neighboring columns, and second-nearest-neighboring columns.

The coupling between incident and neighboring columns is strengthened by bonding for crystals with cation lower in Z than the corresponding anion; the same coupling is weakened by bonding when the cation is higher in Z than the anion. Inter-column coupling has an especially strong effect on HAADF-STEM contrast for columns close (or far smaller) in Z than their neighbors, being so pronounced in some cases that the total intensity on neighboring columns is greater than that on the column where the probe was initially centered (e.g., centered on Li in LiF, Be in BeO, and either B or N in either phase of BN); with sufficient difference in Z this merely causes standard Z-contrast between the columns to be weakened, but in principle this can cause HAADF contrast reversals with two columns barely differing in Z. In polar crystals where this

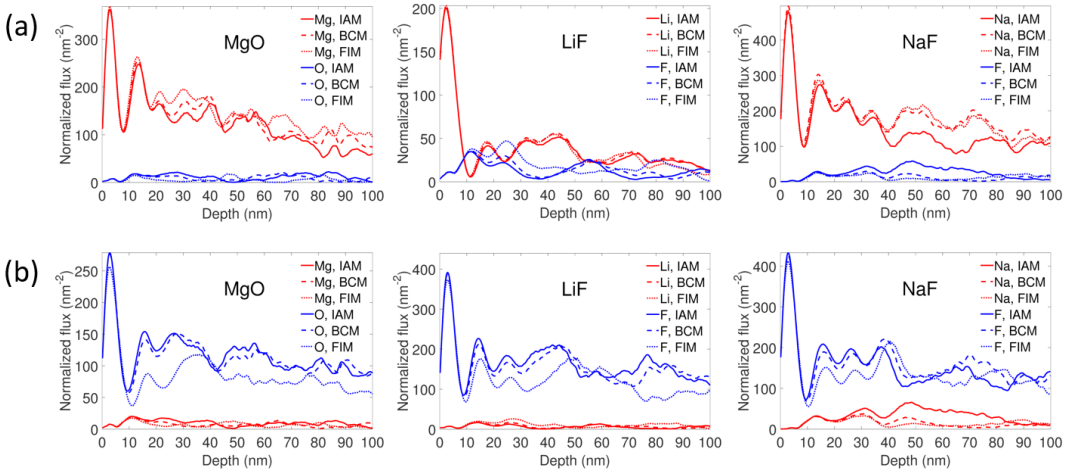

Figure 5.11: Probe intensity incident on atomic columns as a function of depth for ⟨110⟩-oriented halite crystals, with incident probe centered on the (a) cation columns and (b) anion column. Bond polarity increases from left to right. Intensity is tracked on incident columns, first-nearest-neighboring columns, and second-nearest-neighboring columns.

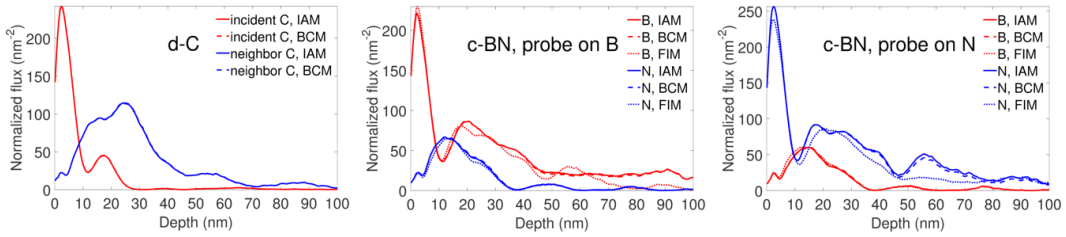

Figure 5.12: Probe intensity incident on atomic columns as a function of depth for ⟨100⟩-oriented cubic crystals, with incident probe centered on the (a) C column in d-C, (b) B column in c-BN, and (c) N column in c-BN. Bond polarity increases from left to right. Intensity is tracked on incident columns, first-nearest-neighboring columns, second-nearest-neighboring columns, and third-nearest-neighboring columns.

is an important consideration, this is the primary cause of bonding-dependent contrast changes: as inter-column coupling decreases in strength due to bonding, contrast will either strongly increase (cation higher in Z than anion) or decrease (anion lower in Z than cation). In crystals with completely non-polar bonding like d-C, including bonding does not meaningfully affect either on-column channeling or beam-spreading behavior, and thus does not affect HAADF-STEM imaging.

5.3.3 Incident probe effects

Many parameters of the incident electron probe may be varied while maintaining atomic resolution ADF imaging. Even with aberration-correction effectively canceling coherent aberrations to create a diffraction-limited probe, the probe energy, convergence angle, and finite source distribution all affect the beam-specimen interaction. Altered beam-specimen interaction, in turn, may alter the strength of bonding effects in ADF imaging.

By maintaining fixed convergence angle and changing beam energy, the effect of incident electron energy can be isolated. An example of beam energy effects is shown in Figure 5.13 for HAADF imaging using 25 mrad probes for $\langle\bar{2}110\rangle$-oriented AlN, where increasing beam energy weakens the contrast change due to bonding and increases the period of depth-varying contrast fluctuations. Increasing electron energy reduces the wavelength of the electrons (reducing the probe size and "depth of focus" for a given convergence angle) and the phase shift due to elastic scattering. The finer probe size decreases inter-column coupling strength and therefore the magnitude of contrast changes due to bonding; the smaller phase shift at higher energies reduces the frequency of inter-column intensity oscillations, in turn reducing the frequency of contrast fluctuations. These results show that the depth-dependence of bonding effects is critically sensitive to beam energy, and that even though bonding effects are slightly stronger at lower beam energies they are robustly present across a wide range.

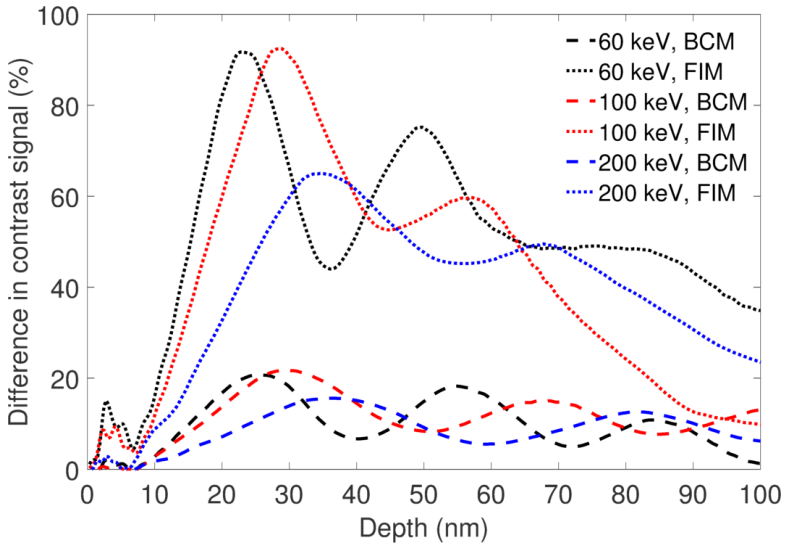

Figure 5.13: Change in contrast signal relative to IAM for 25 mrad probes imaging $\langle\bar{2}110\rangle$-oriented AlN, plotted as a function of depth, bonding model, and electron energy. With convergence angle fixed, the magnitude of contrast change decreases as probe energy increases. Also, the period of depth-dependent fluctuations in the contrast difference increases as probe energy increases.

By maintaining fixed beam energy and changing convergence angle, the effect of changing convergence angle can likewise be isolated. An example of convergence angle effects is shown in Figure 5.14 for HAADF imaging using 200 keV probes for $\langle\bar{2}110\rangle$-oriented AlN, where increasing convergence slightly weakens the contrast change due to bonding but does not alter the period of depth-varying contrast fluctuations. Increasing convergence angle reduces the probe size and "depth of focus" (for a given electron energy). The finer probe size decreases inter-column coupling strength and therefore the magnitude of contrast changes due to bonding; because the phase shift due to elastic scattering remains the same, the frequency of contrast fluctuations is sensitive to bonding model but not convergence angle. This example shows that bonding effects are robustly observable over a wide range of convergence angles, and that this parameter would not need to be finely tuned to observe the effect experimentally.

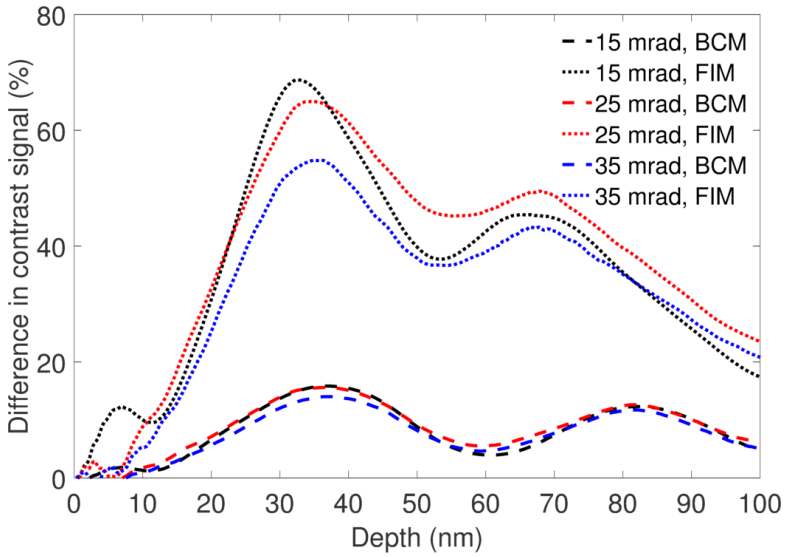

Figure 5.14: Change in contrast signal relative to IAM for 200 keV probes imaging $\langle\bar{2}110\rangle$-oriented AlN, plotted as a function of depth, bonding model, and convergence angle. With beam energy fixed, the magnitude of contrast change decreases as convergence angle increases. The period of depth-dependent fluctuations in the contrast difference does not change with convergence angle, only with bonding model.

A final critical factor to consider is that of finite source size, wherein the ideal diffraction-limited probe is incoherently blurred by the demagnified image of the source at the specimen. An example of finite source effects is shown in Figure 14 for HAADF imaging using a 35 mrad 200 keV probe for $\langle\bar{2}110\rangle$-oriented AlN, where increasing the source size from a point source (effective probe FWHM 0.044 nm) to a gaussian with FWHM 0.05 nm (effective probe FWHM 0.067 nm) to a gaussian with FWHM 0.10 nm (effective probe FWHM 0.109 nm) weakens the contrast change due to bonding. Because the incoherent source contribution solely serves to blur the image, intensities are "flattened out" and contrast changes are reduced, but without contrast changes being altogether eliminated. This example demonstrates the benefit of imaging with highly bright sources and low beam currents to enable very fine demagnified source distributions at the specimen plane: the finer the source distribution, the stronger the change in contrast signal due to bonding. Also, because the quantitative effect

of bonding on image contrast is very sensitive to the effective source distribution, it is critical to precisely determine the source distribution in any experiment seeking to measure the effect of bonding on ADF-STEM imaging.

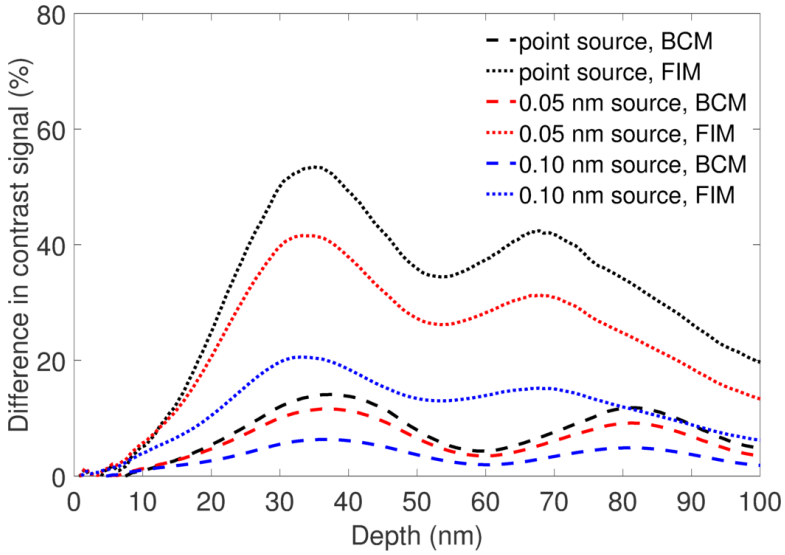

Figure 5.15: Change in contrast signal relative to IAM for 35 mrad 200 keV probes imaging $\langle\bar{2}110\rangle$-oriented AlN, plotted as a function of depth, bonding model, and source size. With convergence angle fixed, the magnitude of contrast change decreases as source size increases. The period of depth-dependent fluctuations in the contrast difference does not change with source size, only with bonding model.

5.3.4 Detector geometry effects

Although the focus thus far has been on "conventional" HAADF-STEM imaging — excluding any strong zero-order Laue zone scattering but collecting all higher-angle scattering including higher-order Laue zone rings — other modes of ADF-STEM imaging are also used for characterizing zone-axis-oriented crystals. Low-angle ADF (LAADF) STEM imaging, which excludes the central disk but allows strong zero-order Laue zone scattering, is highly sensitive to strain fields in crystals and also allows for higher-efficiency (and thus lower-dose) imaging of thin, light-element crystals. Also, due to

the complicating contributions of dynamical higher-order Laue zone diffraction in conventional HAADF-STEM imaging, it is instructive to consider "ultra-high-angle" ADF (UHAADF) STEM imaging that excludes first-order Laue zone rings to give purer Z-contrast.

For electron probes with 35 mrad convergence imaging $\langle\bar{2}110\rangle$-oriented AlN at multiple beam energies, the effects of detector geometry are surveyed in Figure 15 for LAADF (40-200 mrad detector), HAADF (60-200 mrad detector), and UHAADF (200–500 mrad for 60 keV, 200–300 mrad for 100 keV, 150–200 mrad for 200 keV) geometries. The well-established effects of charge transfer, causing stronger contrast changes relative to IAM in the FIM model than the BCM model, are readily apparent for all detector geometries. Also, because coherent contributions to image intensity (zero-order and higher-order Laue zone scattering) do not depend strongly on channeling and beam spreading, contrast changes due to bonding increase from LAADF to HAADF to UHAADF detector geometries. It is interesting to note that the degree of splitting between LAADF, HAADF, and UHAADF contrast fluctuations depends on the beam energy, reflecting the complex effects of dynamical elastic scattering. The implications of these results is that detecting bonding effects is most readily done in highly incoherent ADF-STEM imaging modes, but can also be extended to LAADF-STEM.

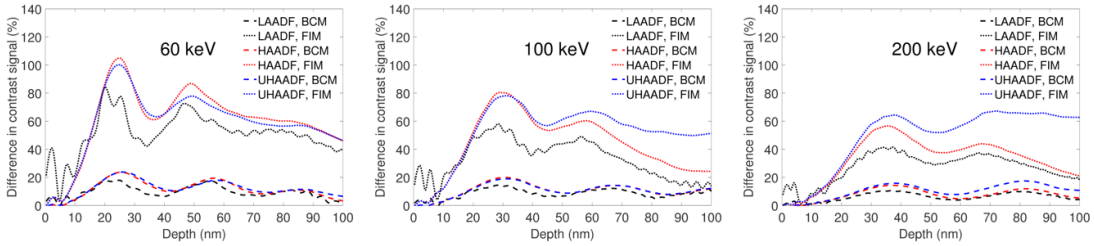

Figure 5.16: Change in contrast ratio relative to IAM for 35 mrad probes imaging $\langle\bar{2}110\rangle$-oriented AlN, plotted as a function of depth, bonding model, and detector geometry for (a) 60 keV, (b) 100 keV, and (c) 200 keV. Although all detectors collect high-angle-scattered electrons, decreasing the contribution of coherent beams from LAADF to HAADF to UHAADF settings strengthens the contrast fluctuations due to channeling and beam spreading effects.

As noted previously for HAADF imaging, due to the weakening of elastic scattering (and thus also channeling effect magnitude) with the increase of beam energy, the magnitude of contrast changes decrease with increasing beam energy for all ADF geometries. Also, due to the decrease in the phase shift due to elastic scattering with the increase of beam energy, the depth frequency of contrast change fluctuations decreases with increasing beam energy, again for all ADF geometries. This demonstrates that bonding effects in ADF-STEM imaging are robust relative to changes in accelerating voltage, even though both the magnitude and frequency of bonding-induced contrast fluctuations depends on all details of the incident STEM probe and the detector geometry.

5.3.5 Thermal vibration effects

As alluded previously, TDS [107] — a term encompassing the effects of atomic vibrations on the scattering of the TEM beam — makes an important contribution to ADF-STEM contrast in typical imaging conditions. [108] Although other prominent TDS algorithms [100, 108–110] exist, the following simulation results employ the frozen phonon [49] method, wherein images simulated using multiple thermally perturbed atomic configurations are incoherently averaged together. Owing to its robust treatment of both elastic scattering and dynamical TDS effects, the frozen phonon method has shown excellent agreement with experiment. [111] As is standard practice, atomic displacements were approximated by an isotropic Einstein model, neglecting the true anisotropy of phonon modes in crystals; including anisotropic phonon effects [112, 113] would further improve the accuracy of bonding-inclusive multislice simulations, albeit to an unknown degree.

As explained in the methods, the TDS-inclusive simulations rely on a parameterized fitting of exact bonding-inclusive projected potentials; however, this adaptation causes these simulations to differ quantitatively from those used in the earlier sections of this study. The parameterized TDS-free (0 K) simulations presented here are in principle

equivalent to the exact simulations discussed in previous sections, but do not exhibit the same quantitative differences relative to IAM data as in the case of the exact projected potential inputs (e.g., for a 100 keV probe with 25 mrad convergence, the magnitude of maximum contrast signal difference for AlN is just over 20% and that for LiF is just under 20% in Figure 5.8, but closer to 15% and 30%, respectively, Figure 5.17(a)). This may reflect inaccuracies in the fitting of the projected potentials, but also contains a contribution from the truncation of the potentials (maximum possible value of the projected potential is that at a half-pixel distance from the projected atomic position, with sub-pixel precision in the positioning of each randomly displaced atom) in the routine that calculates the projected potentials for each frozen phonon configuration using the fitting parameters. The calculation of exact projected potential inputs contained no such truncation and centered atoms exactly on pixels. The differences observed between results calculated with exact projected potential inputs and those calculated with TDS-free parameterized inputs indicate that great care is required in adapting frozen phonon simulations to include bonding.

TDS serves to increase the overall intensity of an ADF-STEM image, introducing an increased background level and thus a decreased contrast signal (Figure Figure 5.17(a). This seems to show that the strongest, most distinct effects of bonding are visible in crystals with no thermal vibrations. However, the differences in contrast signal for BCM relative to IAM (Figure 5.17b) are very much preserved at 300 K, and remain comparable in magnitude to those in a 0 K simulation. These results show that bonding effects are not negated by thermal vibrations and may be detected at room temperature; however, they also corroborate the necessity of including TDS for comparing simulations to room temperature experiments.

When the strength of TDS is increased, changing the configuration of atoms from fixed equilibrium positions at 0 K to moderate RMS displacements at liquid nitrogen temperatures (77 K) to double those RMS displacements at room temperature (300 K), contrast fluctuations for ADF-STEM imaging of $\langle\bar{2}110\rangle$-oriented AlN with a 25 mrad

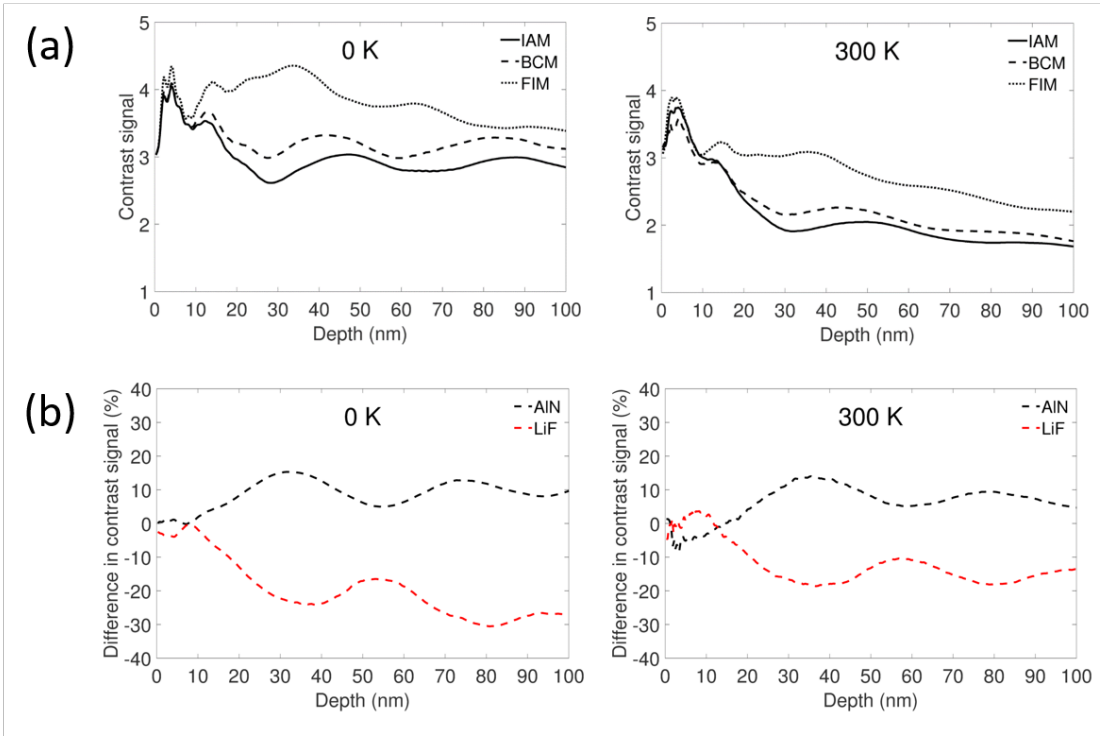

Figure 5.17: Examples of temperature effects on contrast, 100 keV probe with 25 mrad convergence: (a) contrast signal plots for $\langle\bar{2}110\rangle$-oriented AlN with and without thermal vibrations, (b) differences in BCM vs. IAM contrast signal for $\langle\bar{2}110\rangle$-oriented AlN and $\langle 110\rangle$-oriented LiF. TDS effects decrease image contrast for all bonding models, as well as perturb the contrast changes due to bonding.

probe at 100 keV are only weakly influenced by temperature across detector geometries (Figure 5.18). In this case, TDS actually increases the magnitude of contrast changes; this can be explained because TDS reduces the baseline contrast level, but since the strength of bonding effects is essentially unchanged by TDS the magnitude of normalized contrast fluctuations increases slightly. This example shows that, at least within this conventional temperature window, TDS only serves as a minor perturbation on the robust depth-dependent bonding effect, even serving to "enhance" it in some cases. Thus experiments do not have to be performed at low temperatures to examine bonding effects, but can be performed at room temperature also.

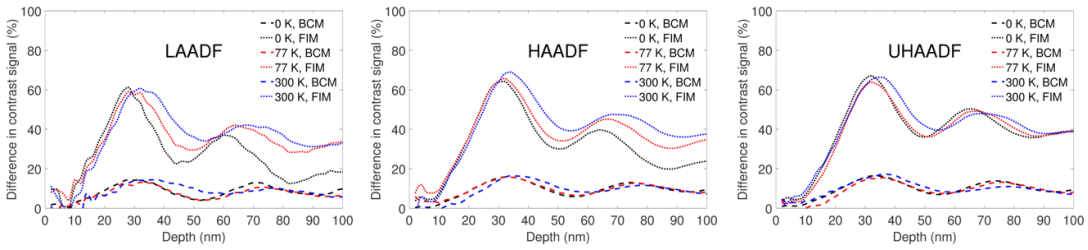

Figure 5.18: Examples of temperature effects on contrast: 100 keV probe with 25 mrad convergence for LAADF, HAADF, and UHAADF detectors. TDS effects slightly increase the magnitude of contrast fluctuations relative to IAM and slightly increase the period of these fluctuations.

5.4 Conclusions

Versatile methods for adapting multislice simulations to include bonding have been presented. Exact transformation of charge densities calculated using each bonding model allows fundamental examination of bonding effects apart from thermal vibrations. The approximate fitting of the exact projected potentials removes some of the symmetry of bonding effects but preserves charge transfer effects, allowing for physically realistic simulation of crystals including TDS effects represented by a frozen phonon

model. These methods serve as reasonable means to perform multislice simulations without being constrained by the IAM approximation.

A survey of initial bonding-inclusive simulations reveals that polar bonding alters the channeling and beam spreading of focused STEM probes, which in turn alters the ADF-STEM imaging for any combination of incident probe, detector geometry, and material temperature; this is true even of the HAADF imaging mode, where coherent scattering contributions to detected intensity are minimized. Although effects of finite demagnified source size strongly dampen the effects of bonding on ADF-STEM image contrast, they do not erase it. These results suggest that ADF-STEM bonding effects should be experimentally measurable in a thoroughly characterized microscope. The effect on ADF image contrast should be most pronounced in crystals with large net charge transfer, under illumination with a very fine effective source size at the specimen.

In principle, the accuracy of ADF image and EELS analysis in polar crystals is improved by including bonding; in practice, the effect may often be too subtle to matter, overwhelmed by typical uncertainties in thickness, surface damage effects, effective source distribution, defocus, and low-order aberrations. Nevertheless, in addition to refining the analysis of ideal single crystals, the inclusion of bonding effects may prove important for systems containing highly charged defects such as ordered point defects, dislocation cores, and polar interfaces.

Chapter 6

Experimental testing of bonding effects for ADF-STEM imaging

6.1 Introduction

Conventional implementations of transmission electron microscopy (TEM) image simulation, both multislice [73, 74] and Bloch wave, [114] model the electrostatic potential of a solid as that of a collection of unbonded neutral atoms; this approximation is known as the independent atom model (IAM). The preceding chapter considered the sensitivity of annular dark field (ADF) scanning TEM (STEM) imaging to valence charge distribution by comparing IAM simulations against charge-transfer-inclusive simulations; extensive computational studies found that light-element single crystals with net interatomic charge transfer exhibited significant differences in ADF-STEM image contrast relative to IAM images. These depth-dependent differences were found to arise because polar bonding alters the channeling [52,53] and beam spreading [98–100,106] of focused STEM probes, which in turn alters the ADF-STEM imaging for any combination of incident probe, detector geometry, and material temperature; this applied even

to the high-angle ADF (HAADF) imaging mode, where bonding effects on coherent scattering into the detector are minimized.

The significance of such computational predictions is uncertain in the context of the aberration corrected [11,12] STEM era, where sub-angstrom resolution HAADF-STEM imaging, [95, 96] electron energy-loss spectroscopy (EELS), [67, 68] and X-ray energy-dispersive spectroscopy (XEDS) [70,115] are routinely performed and found to qualitatively agree with IAM simulations. [100, 106, 116] Furthermore, an extensive literature showing convincing quantitative agreement between IAM simulation and quantitatively calibrated experimental imaging has emerged: atomic resolution HAADF-STEM [117] and BF-STEM [111] imaging of $SrTiO_3$, compositional HAADF-STEM imaging of III-V alloys, [118] atomic resolution imaging of heavy-element ceramics $PbWO_4$ [119] and LaB6, [120] atomic-resolution HAADF-STEM and EELS imaging of $DyScO_3$, [121] atomic resolution thickness measurement of AlN, [122] and three-dimensional dopant location in $SrTiO_3$ [123] and AlN, [124] to name some prominent examples. All of the preceding studies involve systems with highly polar bonding and found good agreement between experimental ADF-STEM images and IAM frozen-phonon multislice simulations.

Of these systems, only AlN has been examined systematically in the companion study, predicting a subtle but measureable effect of bonding on image contrast. Because chemical bonding essentially alters the symmetry of the valence charge distribution of a solid, and in special cases of polar bonding also alters the net charge on each atom, it may have vanishing significance for the ADF-STEM imaging of most crystals: where there is little or no fractional change in the electronic charge on an atom, there should be minimal or no effect on the scattering of fast electrons from those screened atomic nuclei. This may account for the robust adequacy of IAM simulation in most materials systems, but this hypothesis is presently set aside for future testing.

In this study, attentions are rather focused on systems that seem most promising for exhibiting experimentally measureable bonding-sensitivity, namely light-element crystals with highly polar bonding that have already been analyzed in the companion study. By attempting a complete characterization of quantitative HAADF-STEM imaging of the polar crystals AlN and MgO, these images can be compared very precisely to simulations employing various bonding models to examine possible bonding effects. Insofar as significant bonding effects can be ascertained, this may encourage the application of bonding-inclusive simulation not only in analyzing ADF-STEM imaging of perfect single crystals, but also in characterizing important defect systems in polar materials, such as ordered point defects [102] and epitaxial interfaces. [103]

6.2 Methods

AlN and MgO single crystals, materials examined in the computational studies of the preceding chapter, were determined to be suitable subjects for experimental study. Both materials can be grown as high-quality single crystals and are employed as substrates for epitaxial thin film growth. Important properties of crystal structure and chemical bonding are summarize below in Table 6.1.

Property	**AlN**	**MgO**
Crystal structure	wurtzite	halite
Bond length (nm)	0.190	0.209
Inter-column spacing (nm)	0.109	0.148
Pauling ΔX	1.43	2.13
Formal valency	+/3	+/2
Band gap (eV)	6.0	7.8

Table 6.1: Comparison of key properties of AlN and MgO crystals. Both materials are insulators with large net charge transfer.

Observation of bonding-dependent image contrast requires imaging these crystals at zone axes where the columns are spaced sufficiently far apart to be resolved by an aberration-corrected electron probe, with each column being composed entirely of one

type of atom (e.g., Al in separate columns from N in AlN). These conditions are satisfied by the $\langle\bar{2}110\rangle$ orientation of AlN and by the $\langle 110\rangle$ orientation of MgO (Figure 6.1).

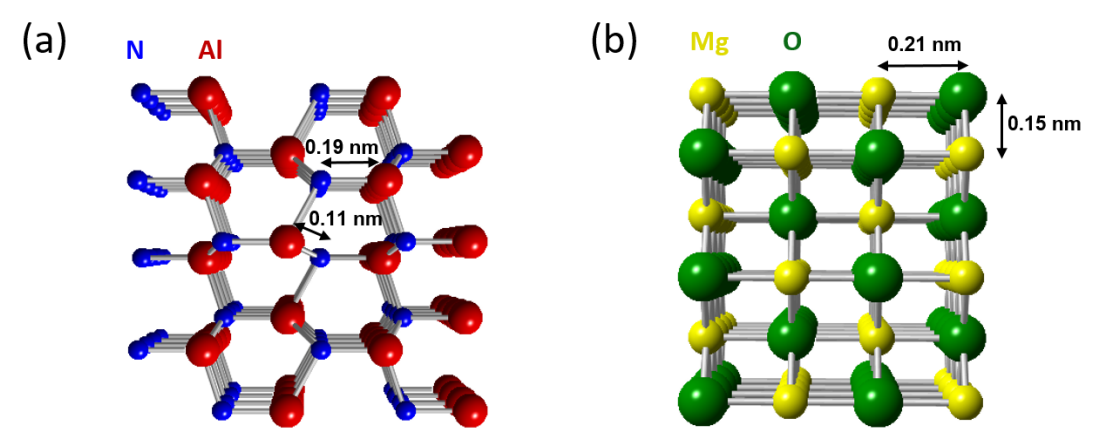

Figure 6.1: Perspective crystal structure renderings of (a) $\langle\bar{2}110\rangle$-oriented AlN and (b) $\langle 110\rangle$-oriented MgO. Both nearest-neighbor and second-nearest-neighbor inter-column spacings are indicated; in each case, the nearest-neighboring column is 0.6–0.7× the bond length.

AlN was prepared for STEM imaging by mechanical wedge polishing of a (0001) wafer grown by physical vapor transport, provided by Nitride Crystals, Inc. Subsequent treatments included etching in a dilute HF acid solution to remove the surface damage layer, deposition of a colloidal silver coating to produce better conductive contact to the washer, and Ar/O2 plasma cleaning to remove hydrocarbon contaminants. A (100)-grown MgO single crystal substrate was prepared by crushing in isopropanol, followed by drop-casting onto a TEM grid with a holey carbon support film; a final treatment of heating at 150°C under ultra-high-vacuum conditions immediately preceded transfer into the TEM.

STEM imaging was performed using a FEI Titan G2 60–300 equipped with a CEOS DCOR probe corrector, high-brightness Schottky field emission gun, Fischione 2100 HAADF detector, Gatan BM-Ultrascan CCD camera, and Gatan Enfinium ER parallel EELS spectrometer. The microscope was operated at 200 keV in low-dose-rate (a 10.0

pA beam current as measured from calibrated fluorescent screen intensity, with dwell times of 1–6 µs per pixel) conditions and a large convergence semi-angle of 30 mrad, conditions producing extremely high spatial resolution (up to 15 nm^{-1} information transfer) while maintaining acceptable levels of image noise, specimen drift, and charging. Projection lens settings used for very thin specimens of AlN corresponded to a 55 mrad HAADF inner semi-angle and 11 mrad EELS semi-aperture, while those used in all other conditions corresponded to a 68 mrad HAADF inner semi-angle and 13 mrad EELS semi-aperture. Effective HAADF outer angle was not determined experimentally, but rather taken as 200 mrad, as estimated by FEI and used to good quantitative agreement in another study. [121] EELS spectra were acquired with a dispersion of 0.05 eV/channel, allowing accurate sampling and fitting of the zero-loss peak for EELS-based thickness measurements.

All raw images were processed by taking regions of uniform contrast, applying an aggressive low-pass filter (8 $nm^{-}1$ passband with Butterworth smoothing of cutoff), and cross-correlating 20–100 images together to form a low-resolution reference image with high signal-to-noise ratio (SNR). Subsequently, the same images were filtered more moderately (16 $nm^{-}1$ passband with Butterworth smoothing of cutoff) and cross-correlated to form a many-unit-cell cross-correlated image with full information transfer and high SNR. Obvious edge artifacts, attributable to pervasive image distortions (uneven rastering and specimen drift) and the cutting of images into patches not exactly commensurate with the crystal unit cell, were cropped away to leave integer multiples of unit cells. The remaining reliable sections of such images could then be spline-interpolated for matching image simulation (by means of image rotation and matching of experiment image sampling to the simulation sampling), allowing straightforward comparison between simulated and experimental images. Crystallographically identical linescans from within the final interpolated experimental image were averaged to produce representative experimental linescans.

Imaging was performed with a detector dynamic range spanning approximately 0–2.5 pA ($0 - 0.25P_0$ in terms of incident probe current P_0) in the most sensitive sections of the detector. Owing to the sensitivity of imaging to detector non-uniformity, [125] detector mapping was done in each session using the same settings of detector gain ("contrast") and voltage offset ("brightness") as used for HAADF imaging, with an incident beam current of 1.5 pA ($0.15P_0$). The method employed to convert raw images into quantitatively calibrated images, described below, adapts the notation and terminology of a recently published study that employed an equivalent method. [126]

Detector maps were converted into reciprocal space measurements of detector response $D(\boldsymbol{k})$ ($\boldsymbol{k}$ is a reciprocal-space vector, for small angles $\approx \lambda k$), such that the dark-level subtracted detector signal $I(\boldsymbol{k})$ was related to any normalized detector mapping current $N_M \equiv P_M/P_0$ according to $I(\boldsymbol{k}) = N_M D(\boldsymbol{k})$. The average detector response $\overline{D}$ (averaged over a large, highly uniform region of the detector, Equation 6.1) and the non-uniform detector efficiency $\hat{D}(\boldsymbol{k})$ (Equation 6.2) were calculated as follows:

$$\overline{D} \equiv \frac{\int\int D(\boldsymbol{k}) d^2\boldsymbol{k}}{\int\int d^2\boldsymbol{k}} \tag{6.1}$$

$$\hat{D} \equiv \frac{D(\boldsymbol{k})}{\overline{D}} \tag{6.2}$$

Combining the measured non-uniform detector response $D(\boldsymbol{k})$ (universal for a given detector setting) with a knowledge of the scattered flux distribution $F(\boldsymbol{r}, \boldsymbol{k})$ (specific to incident probe parameters, incident probe position, projection optics settings, specimen structure, specimen thickness), the normalized imaging current N (Equation 6.3) and detector signal I (Equation 6.4) are each varying as a function of probe position r to form the ADF STEM image as follows (both integrations are performed over the illuminated section of the detector).

$$N(\boldsymbol{r}) = \int\int F(\boldsymbol{r}, \boldsymbol{k}) d^2\boldsymbol{k} \tag{6.3}$$

$$I(\boldsymbol{r}) = \int\int D(\boldsymbol{k})F(\boldsymbol{r},\boldsymbol{k})d^2\boldsymbol{k} \tag{6.4}$$

A damping coefficient ξ (Equation 6.5) can then be defined to capture the attenuation of experimentally detected intensity $I(\boldsymbol{r})$ (Equation 6.6) relative to signal measured by a perfect detector ($D(\boldsymbol{k}) = \overline{D}$ for all $\boldsymbol{k}$), which in principle varies with probe position $\boldsymbol{r}$.

$$\xi(\boldsymbol{r}) = \frac{\int\int D(\boldsymbol{k})F(\boldsymbol{r},\boldsymbol{k})d^2\boldsymbol{k}}{\int\int \overline{D}F(\boldsymbol{r},\boldsymbol{k})d^2\boldsymbol{k}} \tag{6.5}$$

$$I(\boldsymbol{r}) = \overline{D}\frac{\int\int D(\boldsymbol{k})F(\boldsymbol{r},\boldsymbol{k})d^2\boldsymbol{k}}{\int\int \overline{D}F(\boldsymbol{r},\boldsymbol{k})d^2\boldsymbol{k}}\int\int F(\boldsymbol{r},\boldsymbol{k})d^2\boldsymbol{k} = \overline{D}\xi(\boldsymbol{r}N(\boldsymbol{r} \tag{6.6}$$

However, because it is essentially the magnitude rather than the reciprocal-space shape of the scattered flux distribution that is position-dependent (Equation 6.7), a single position-independent damping factor can be defined (Equation 6.8) and the detected signal intensity can be simply transformed to a scale of normalized imaging current (Equation 6.9). This quantification process is illustrated in Figure 6.2.

$$F(\boldsymbol{r},\boldsymbol{k}) \equiv A(\boldsymbol{r})B(\boldsymbol{k}) \tag{6.7}$$

$$\xi(\boldsymbol{r}) = \frac{\int\int D(\boldsymbol{k})A(\boldsymbol{r})B(\boldsymbol{k})d^2\boldsymbol{k}}{\int\int \overline{D}A(\boldsymbol{r})B(\boldsymbol{k})d^2\boldsymbol{k}} = \frac{\int\int D(\boldsymbol{k})B(\boldsymbol{k})d^2\boldsymbol{k}}{\int\int \overline{D}B(\boldsymbol{k})d^2\boldsymbol{k}} \equiv \xi \tag{6.8}$$

$$N(\boldsymbol{r}) = \frac{I(\boldsymbol{r}}{\overline{D}\xi(\boldsymbol{r})} = \frac{I(\boldsymbol{r}}{\overline{D}\xi} \tag{6.9}$$

The same independently published study that set forth our method of STEM quantification, alluded to earlier, also carefully compared results obtained using this method to the standard quantification routines (those applying non-uniform detector response to simulation rather than inverting the response from experimental data), and found

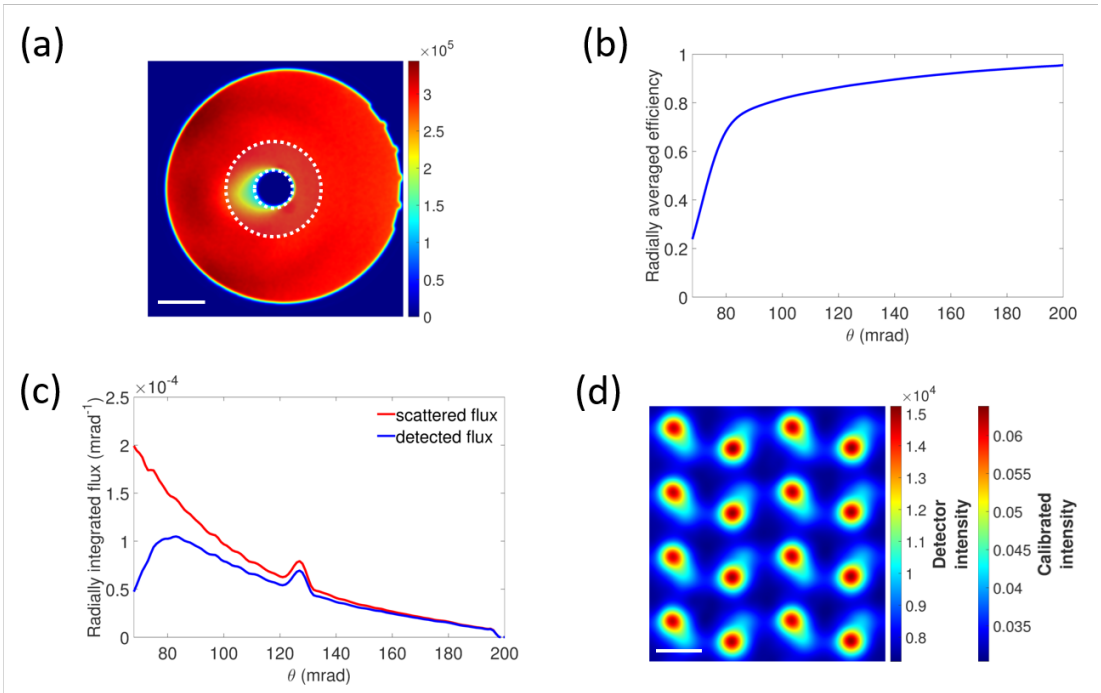

Figure 6.2: Quantification of an experimental HAADF image. (a) Detector response map $D(\boldsymbol{k})$ acquired with 1.5 pA incident current; 68–200 mrad conditions correspond to scale bar length 200 mrad (800 nm^{-1}). (b) Radially averaged efficiency profile $\hat{D}(k)$ for 68–200 mrad collection. (c) Radially integrated fluxes for 68–200 mrad collection, where the scattered flux is attenuated by the efficiency profile to determine the detected flux. (d) Cross-correlated image of 80 nm thick AlN using a 68–200 mrad detector, both in terms of detected intensity $I(\boldsymbol{r})$ and quantitative calibrated intensity $N(\boldsymbol{r})$ ($\overline{D} = 3.10 \times 10^5$, $\xi = 0.77$), scale bar length = 0.2 nm.

them to be equivalent. Because our experimentally recorded flux distribution measurements exhibited poor SNR at high scattering angles and/or were recorded with the HAADF detector inserted, the scattered flux distribution was estimated from frozen phonon position-averaged CBED [127] (PACBED) simulations performed for the estimated thickness. Thickness was estimated from any available combination of experimentally recorded data: low-loss EELS spectra, PACBED patterns, and "position-averaged HAADF" [122] (PAHAADF) imaging. Because the damping factor ξ changes very gradually as a function of increasing thickness, PAHAADF alone was sufficient to estimate thickness to $+/-1$ nm in cases where no reliable low-loss EELS data is acquired or PACBED cannot produce a clear thickness estimate (e.g., in thick specimens due to complex elastic PACBED pattern contrast and strong inelastic scattering distortions). Although applicable in principle, data suitable for the incoherent bright-field [128] method for crystalline thickness determination method was not collected. Crystal orientation was determined using PACBED data.

Even with convergence angle, detector geometry, crystal orientation, and crystal thickness determined from experimental data, critical probe parameters remain strictly unknown: defocus, coherent low-order aberration effects (especially two-fold astigmatism), and the effective demagnified source distribution. Without having acquired focal series data to assist in the determination of defocus, low-order aberrations, and source distribution, a comparatively crude procedure was used to estimate experimental imaging parameters. As much as possible, the orientation of two-fold astigmatism was estimated from visible asymmetry in the high-SNR images. Simulated images with different magnitudes of two-fold astigmatism in this orientation were then checked in slight underfocus and slight overfocus conditions to produce a range of possible defocus/astigmatism combinations. Finally, different source distributions were considered, under the constraint that convolution of those source distributions with simulated images simultaneously yielded a good fit to three different experimental measures: the width of atomic column features, the intensity of atomic columns in the image, and

the "background" level of the image. Considering that there was no measurable change in gun emission current during the two-week span over which these experiments were performed, a single source distribution was applied to all simulations before they were compared to experimental data.

To include the effects of bonding using computational methods, three different bonding models were used: the independent atom model (IAM), the bonded crystal model (BCM), and the fully ionized model (FIM). In IAM, the charge density of the solid was calculated as the superposition of the charge densities of independent neutral atoms. In BCM, the charge density of the solid was calculated as the superposition of atomic ion-core charge densities with valence charge densities calculated by density functional theory (DFT). In FIM, the charge density of the solid was calculated as the superposition of the charge densities of independent full-valence-shell ions. Methods for calculating the charge densities and transforming them into inputs for multislice simulation are detailed within Chapter 5.

Multislice simulations of each bonding model employed probe and transmission functions calculated on a 1024×1024 pixel grid, with a supercell of size 4.31×3.98 nm^2 for AlN and one of size 3.35×2.37 nm^2 for MgO. Each supercell corresponded to 8×8 tiling of the effective rectangular unit cell (0.539×0.498 nm^2 for $\langle\bar{2}110\rangle$-oriented AlN, 0.419×0.296 nm^2 for $\langle 110\rangle$-oriented MgO) at each crystalline orientation, allowing exact sampling of Bragg reflections. Probe positions were sampled on either a 64×64 pixel grid within the rectangular unit cell of each crystal. Slice thicknesses were chosen to be the interplanar spacings along the beam direction for $\langle\bar{2}110\rangle$-oriented AlN (0.155 nm) and $\langle 110\rangle$-oriented MgO (0.148 nm), allowing the correct reproduction of higher-order Laue zone diffraction. To ensure accurate TDS-inclusive simulations, RMS thermal vibration values were determined from the experimental diffraction literature for each AlN [129] (3D RMS displacements of 10.7 pm and 11.6 pm for Al and N, respectively) and MgO [130] (3D RMS displacements of 10.7 pm and 11.4 pm for Mg and O, respectively), and 3–20 frozen phonon configurations were averaged to form a given image or

PACBED pattern. As is standard practice, neither the anisotropy of thermal vibrations nor the contributions of inelastic scattering were included in these simulations. Effects of finite source distribution were included by convolution of the source function with the simulated point-source images.

6.3 Results and discussion

Although it is BCM that expressly emulates the bonding of real solids, it is instructive to compare BCM multislice simulations to the hypothetical extremes of non-existent (IAM) and complete (FIM) charge transfer. If, within experimental uncertainty, BCM image simulations can be found to be a statistically significant best fit relative to IAM and FIM simulations, the effect of bonding on HAADF-STEM image contrast is experimentally demonstrated.

6.3.1 Experimental imaging

Cross-correlated images were obtained from multiple thicknesses of each AlN and MgO. Of these, four thicknesses of each sample were chosen for quantitative analysis. As discussed in the simulation section, for each crystal this included both thicknesses with a predicted strong bonding effect and those with a predicted negligible bonding effect. For the accuracy of bonding-inclusive simulations to be tested, they should match well for "control thicknesses" where the effect of bonding is predicted to be weak as well as thicknesses where it is predicted to be strong.

CBED patterns and quantitatively calibrated HAADF-STEM images from these thicknesses for each AlN (Figure 6.3) and MgO (Figure 6.4) are displayed below. Thickness determination for AlN was performed by comparing experimental PAHAADF mean intensities to those in IAM simulations; the results of which were within 10% of those determined using calibrated low-loss EELS [122] thickness estimates. Due to inaccessibility of the EELS hardware during MgO experiments and distortion of PACBED

patterns by inelastic scattering at high thickness, thickness measurements of MgO were determined from PAHAADF comparisons alone (PACBED patterns were consistent with PAHAADF-based thickness measurement). Owing to strong charging of MgO under the electron beam, imaging was performed with significant two-fold astigmatism in the probe that was clearly revealed only after cross-correlation.

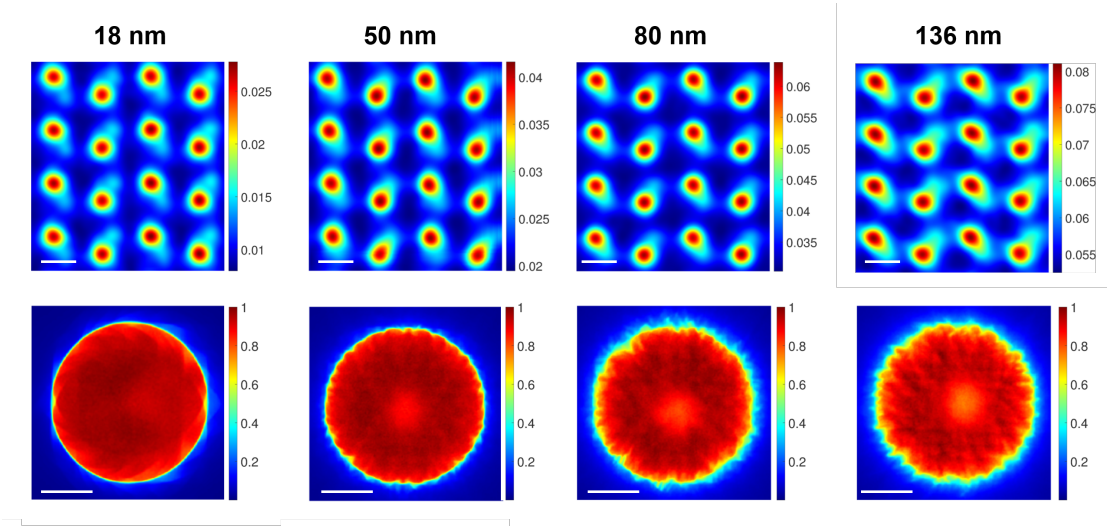

Figure 6.3: Quantitatively calibrated HAADF-STEM imaging of different sections of a $\langle\bar{2}110\rangle$-oriented AlN sample. Thickness was determined by PAHAADF, orientation was determined by PACBED. For images, regions are 2×2 rectangular unit cells in area, intensity is quantitatively calibrated, scale bar length is 0.2 nm. Diffraction patterns are normalized relative to the most intense region of the pattern, scale bar corresponds to 20 mrad (8 nm^{-1}).

Owing to inhomogeneity of the original images — due to hydrocarbon contamination, surface damage, thickness variation, or some combination of the above — cross-correlated images also exhibit inhomogeneity. Representative linescans of these images were constructed by averaging together linescans through each set of equivalent features in the experimental image. Because the SNR of the images after filtering and cross-correlation is extremely high, this error essentially reflects inhomogeneities in the image due to specimen drift, scan distortion, and intrinsinc fine-scale structural variation.

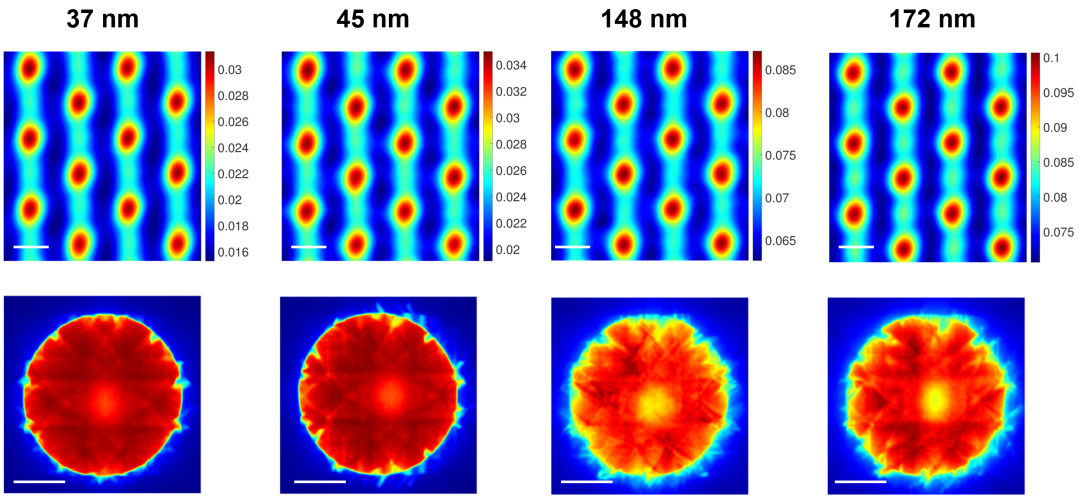

Figure 6.4: Quantitatively calibrated HAADF-STEM imaging of different sections of a ⟨110⟩-oriented MgO sample. Thickness was determined by PAHAADF, orientation was determined by PACBED. For images, regions are 3×2 rectangular unit cells in area, intensity is quantitatively calibrated, scale bar length is 0.2 nm. Diffraction patterns are normalized relative to the most intense region of the pattern, scale bar corresponds to 20 mrad (8 nm^{-1}).

6.3.2 Multislice simulation

Bonding-inclusive multislice simulations of the companion study indicated a strong depth-dependence of the effect of bonding on image contrast. Employing an idealized probe for the HAADF-STEM imaging of these crystals — gaussian focus, no low-order aberrations — the effect of bonding on multislice image simulations is summarized in Figure 6.5. Strongest bonding effects are predicted to emerge at thicknesses 30 nm and above in AlN, and at 50 nm and above in MgO; while image contrast is most altered relative to IAM for FIM simulations, meaningful differences also exist between IAM and BCM. Although these calculations do not include the effects of finite source size, it was shown in Chapter 5 that the effect of bonding on image contrast is robust relative to the blurring effect of a fine source distribution. Thus bonding effects on contrast are preserved in experimental imaging, albeit in a damped form, and point source calculations are sufficient to predict the depth-dependent fluctuation of these contrast changes.

The set of experimental images examined include both thicknesses with a strong theoretically predicted bonding effect and those with a negligible effect (i.e., very small difference between IAM and BCM simulation predictions). With high-quality calibrated experimental data in hand, a direct comparison can be made between experiment and simulation. However, a meaningful comparison requires simulations to replicate as fully as possible the conditions of the experimental imaging.

Crystal thickness (neglecting unknown effects of reconstruction, damage, or contamination at the surfaces by treating the entire thickness as perfect) and crystal orientation were fixed based on experimental data. Although the mis-tilts of the experimental images were small, all being 6 mrad or lesser, the effect was included on account of computational studies [131, 132] showing that even slight misorientation can measurably affect ADF-STEM image contrast of zone-axis-oriented single crystals. Fitting across

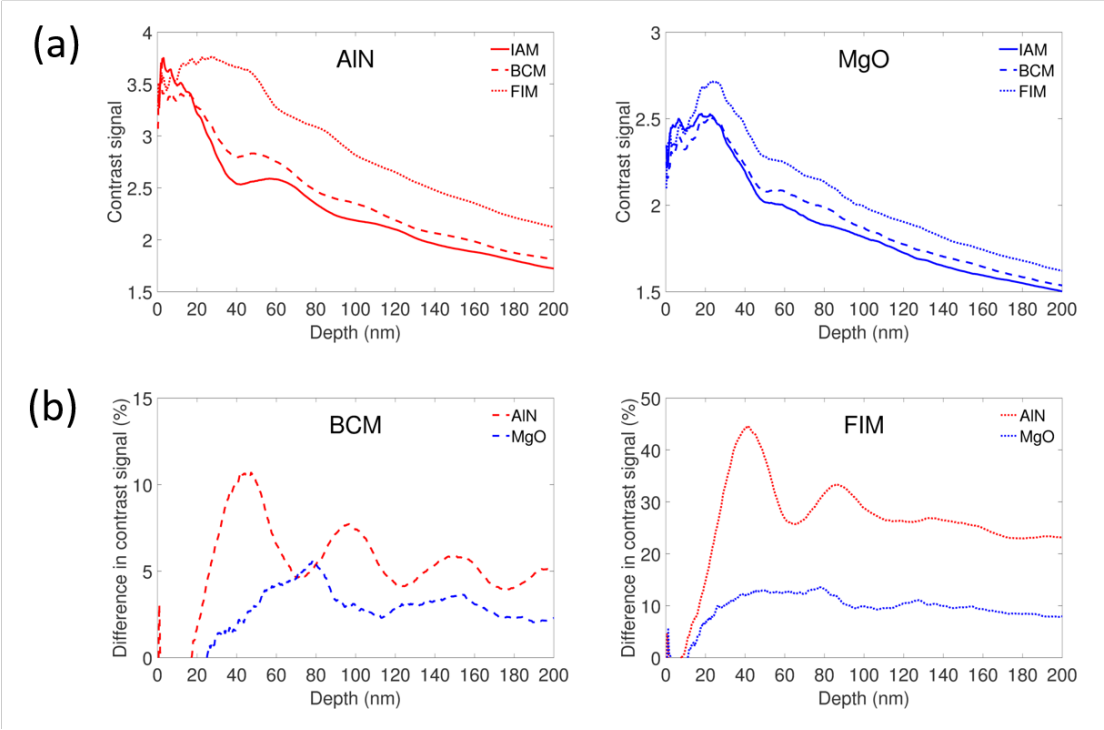

Figure 6.5: HAADF-STEM image contrast for AlN and MgO in point-source conditions. (a) Variation in contrast signal as a function of depth. (b) Differences in contrast signal relative to IAM.

all images yielded a good fit from a gaussian-like function with longer-ranged tails, as determined in independent experimental characterizations [120,121,133] of high-brightness electron sources. In these studies this entailed a gaussian of FWHM 0.05 nm, convolved with a truncated lorentzian of FWHM 0.01 nm. The effect of this source distribution is illustrated below (Figure 6.6) for an approximately aberration-free probe of the same beam energy and convergence angle as used in experiments.

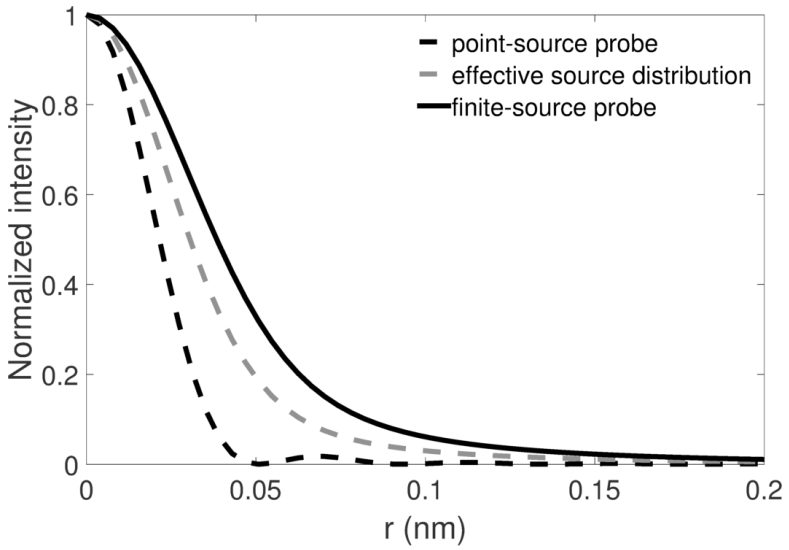

Figure 6.6: Radial profiles of the point-source electron probe, the estimated source distribution, and the finite-source probe. Including source size broadens the incident probe from a FWHM of 0.043 nm to a FWHM of 0.079 nm.

Having estimated the source distribution by fitting to well-focused images, the simulated probe for each image was estimated as fully aberration-corrected apart from two-fold astigmatism; this approximation was justified by stable measurements of higher-order aberrations made using the probe corrector aberration measurement routines immediately prior to experimental imaging. With the orientation of two-fold astigmatism being estimated from visible asymmetries in the images, it is the combination of two-fold astigmatism amplitude and defocus that remain as tunable parameters. These parameters were set so as to have simulated images roughly match both the overall contrast

and linescan anisotropy of the images. Final parameters for imaging simulations of AlN (Table 6.2) and MgO (Table 6.3) are summarized below.

Parameter	**18 nm**	**50 nm**	**80 nm**	**136 nm**
Mistilt (mrad)	6.0	0.5	2.5	5.0
Defocus (nm)	−2.0	+2.0	+1.0	+3.0
Two-fold astigmatism (nm)	0.6	0.0	0.6	0.6

Table 6.2: Summary of parameters used to simulate conditions of each AlN imaging experiment. Zero corresponds to Gaussian focus, while positive values of defocus correspond to overfocus.

Parameter	**37 nm**	**45 nm**	**148 nm**	**172 nm**
Mistilt (mrad)	3.5	3.0	4.5	5.0
Defocus (nm)	+2.0	+3.0	+4.0	+3.5
Two-fold astigmatism (nm)	1.2	1.2	1.2	1.2

Table 6.3: Summary of parameters used to simulate conditions of each MgO imaging experiment. Zero corresponds to Gaussian focus, while positive values of defocus correspond to overfocus.

6.3.3 Comparison of experiment and simulation

The resulting simulations for both AlN (Figure 6.7) and MgO (Figure 6.8) are featured alongside experimental data. In concert with other quantitative STEM studies, good overall agreement is found between carefully tuned frozen-phonon multislice simulations and quantitatively calibrated ADF-STEM imaging.

For some of the experimental images, such as over 100 nm thick of each crystal, none of the simulations match the image contrast of the experimental data. At the very least, this reflects the challenge of exact matching of simulated probe conditions to experiment. In the case of MgO, which hydrolyzes rapidly in atmosphere, it may also reflect altered contrast due to an amorphous layer [134] at the incident surface. The redistribution of elastically scattered intensity by inelastic scattering [135] may also contribute to the discrepancy between experiment and simulation for those higher thicknesses. For 18 nm AlN, overall contrast matches, but the simulated images clearly differ in appearance from

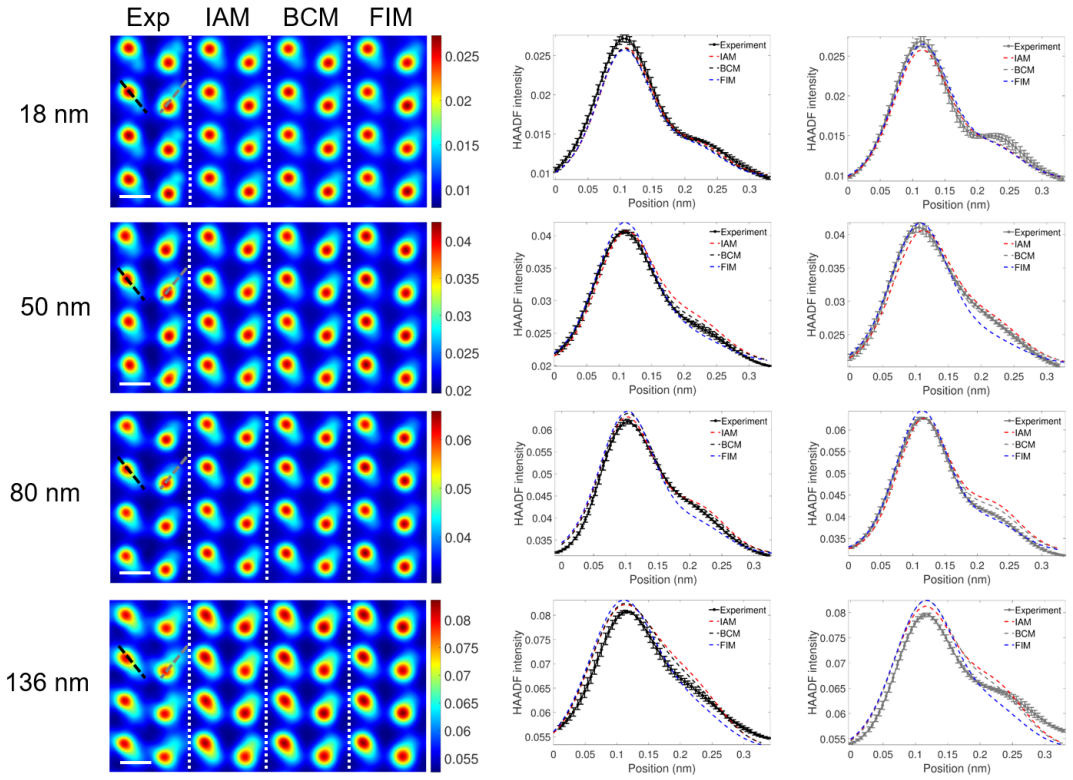

Figure 6.7: Comparison of quantitatively calibrated HAADF-STEM imaging of different sections of a $\langle\bar{2}110\rangle$-oriented AlN sample to corresponding simulations. Regions are 2×2 rectangular unit cells in area, scale bar length is 0.2 nm. Error bars correspond to one standard deviation of linescan-to-linescan variation.

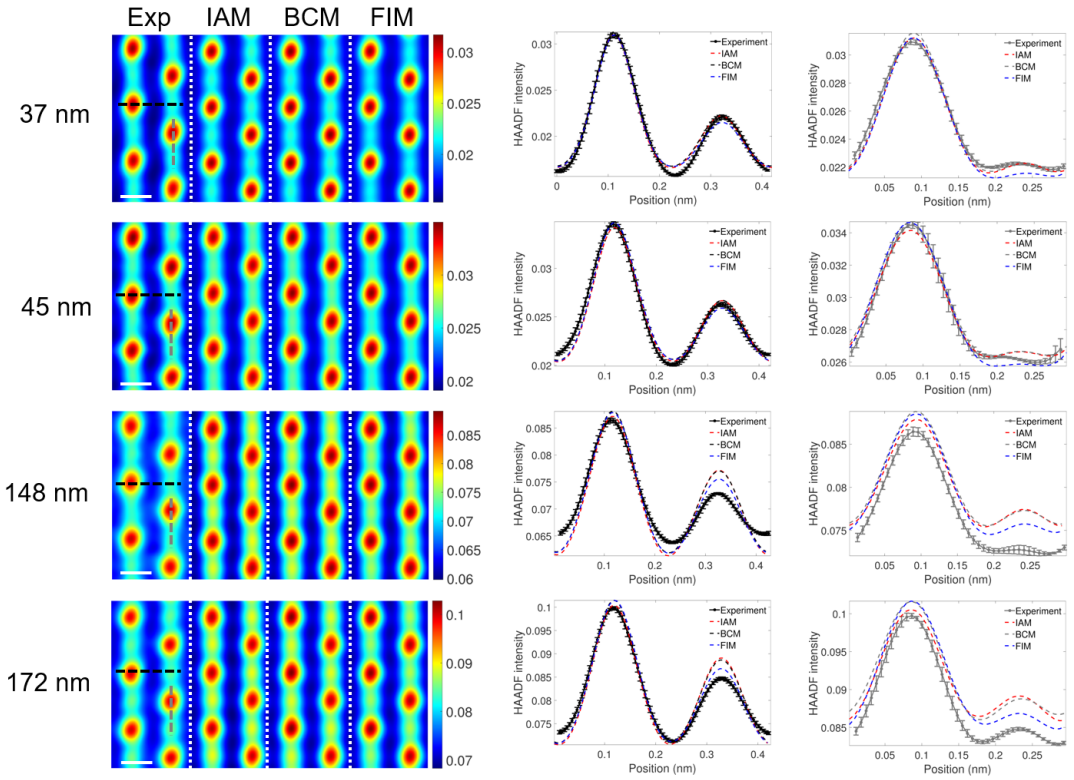

Figure 6.8: Comparison of quantitatively calibrated HAADF-STEM imaging of different sections of a ⟨110⟩-oriented MgO sample to corresponding simulations. Regions are 3×2 rectangular unit cells in area, scale bar length is 0.2 nm. Error bars correspond to one standard deviation of linescan-to-linescan variation.

experiment and the simulation linescans do not reproduce the experimental linescan anisotropy; this mismatch highlights the difficulty of exactly reproducing the magnitude and orientation of experimental probe astigmatism in simulation.

In spite of the difficulty exactly matching simulations and experiments, some of these results do demonstrate varying levels of agreement with image simulations performed using different bonding models. In the case of thicknesses where there is no exclusive best agreement with any one bonding model (18 nm AlN, 37 nm MgO, 45 nm MgO), the effects of bonding must be conceded as undetectable. However, in the AlN image data at thicknesses of 50 and 80 nm, exclusive best agreement between experiment and BCM simulation demonstrates the depth-dependent effect of chemical bonding on HAADF-STEM image contrast. Although the experimental images are "deformed" by the effects of probe aberrations and effective source distribution, the differences between images simulated using each bonding model are preserved and a systematic best match exists. These differences confirm an old result in new fashion: the electron distribution in a polar crystal is best represented by covalent bonding, which differs significantly from an array of independent neutral atoms or an array of independent formal-charge ions.

6.4 Conclusion

Quantitatively calibrated ADF-STEM images the polar light-element crystals AlN and MgO were conducted using a procedure that inverts the effect of detector non-uniformity from experimental data. Direct comparison to bonding-inclusive multislice simulations experimentally confirms the depth-dependent effect of bonding on ADF-STEM imaging, an effect explained and systematically examined in a companion computational study. This constitutes the first measurement of bonding effects in the widely used HAADF-STEM imaging mode, and encourages inclusion of bonding effects to improve the accuracy of TEM image simulation for crystals with highly polar bonding. Furthermore, it shows that while neutral-atom inputs can be measurably incorrect, fully

ionic inputs are also problematic; proper bonding-inclusive inputs must reflect the true magnitude of interatomic charge transfer calculated from first principles.

Although the effects of chemical bonding on ADF-STEM imaging are measurable, they are quite subtle, requiring careful processing of experimental images and fine-tuning of simulation to discern them. Conventional IAM simulations are wholly adequate for qualitative agreement with experiment, and in many cases also for quantitative agreement. However, the intrinsic effect of net interatomic charge transfer on the channeling of a TEM beam in a crystal can only be addressed by bonding-inclusive simulation. Thus use of bonding-inclusive simulation refines quantitative STEM imaging and spectroscopy of bulk polar single crystals, as well as that of defect systems in polar materials (e.g., ordered point defects and epitaxial interfaces). Further work should be done to explore the significance of bonding effects in light-element vs. heavy-element systems. The quantitative significance of including thermal vibration anisotropy and plasmon scattering in multislice simulations is also worthy of further consideration.

It should be noted that this study was limited by typical uncertainties in determining thickness, surface damage effects, effective source distribution, defocus, and astigmatism; reasonable final estimates of these quantities were made, but with much effort and limited confidence. This experience suggests that the development of automated, convenient routines for tasks such as thickness measurement, amorphous layer measurement, detector calibration, source distribution determination, and residual astigmatism measurement are necessary prerequisites for widespread adoption of quantitative STEM methods.

References

[1] Williams, D. & Carter, C. *Transmission electron microscopy: a textbook for materials science* (Springer Verlag, 2009).

[2] Reimer, L. & Kohl, H. *Transmission electron microscopy: physics of image formation*, vol. 36 (Springer, 2008).

[3] Wu, J., Shaw, C. & Martin, D. 2.19 - electron microscopy of organic materials: An overview and review of recent developments. In Matyjaszewski, K. (ed.) *Polymer Science: A Comprehensive Reference*, 509 – 525 (Elsevier, Amsterdam, 2012).

[4] Loane, R. F., Xu, P. & Silcox, J. Incoherent imaging of zone axis crystals with adf stem. *Ultramicroscopy* **40**, 121–138 (1992).

[5] Hillyard, S. & Silcox, J. Detector geometry, thermal diffuse scattering and strain effects in adf stem imaging. *Ultramicroscopy* **58**, 6–17 (1995).

[6] Pennycook, S. Z-contrast stem for materials science. *Ultramicroscopy* **30**, 58–69 (1989).

[7] Egerton, R. F. *Electron Energy-Loss Spectroscopy in the Electron Microscope* (Springer, New York, 2011), 3rd edn.

[8] Batson, P. E. Simultaneous stem imaging and electron-energy-loss spectroscopy with atomic-column sensitivity. *Nature* **366**, 727–728 (1993).

[9] Ahn, C. *Transmission electron energy loss spectrometry in materials science and the eels atlas* (Wiley-VCH, 2004), 2 edn.

[10] Scherzer, O. Spharische und chromatische korrektur von elektronen-linsen. *Optik* **2**, 114–132 (1947).

[11] Haider, M., Uhlemann, S., Schwan, E., Rose, H., Kabius, B. & Urban, K. Electron microscopy image enhanced. *Nature* **392**, 768–769 (1998).

[12] Batson, P. E., Dellby, N. & Krivanek, O. L. Sub-angstrom resolution using aberration corrected electron optics. *Nature* **418**, 617–620 (2002).

[13] Cowley, J. & Moodie, A. The scattering of electrons by atoms and crystals: a new theoretical approach. *Acta Crystallographica* **10**, 609–619 (1957).

[14] Kirkland, E. J. *Advanced Computing in Electron Microscopy* (Springer, New York, 2010), 2nd edn.

[15] Novoselov, K. S. Two-dimensional atomic crystals. *Proceedings of the National Academy of Sciences* **102**, 10451–10453 (2005).

[16] Geim, A. K. & Novoselov, K. S. The rise of graphene. *Nat Mater* **6**, 183–191 (2007).

[17] Wang, Q. H., Kalantar-Zadeh, K., Kis, A., Coleman, J. N. & Strano, M. S. Electronics and optoelectronics of two-dimensional transition metal dichalcogenides. *Nature Nanotechnology* **7**, 699–712 (2012).

[18] Butler, S. Z. *et al.* Progress, challenges, and opportunities in two-dimensional materials beyond graphene. *ACS Nano* **7**, 2898–926 (2013).

[19] Geim, A. K. Graphene: status and prospects. *Science* **324**, 1530–1534 (2009).

[20] Pumera, M. Electrochemistry of graphene: new horizons for sensing and energy storage. *The Chemical Record* **9**, 211–223 (2009).

[21] Dean, C. *et al.* Boron nitride substrates for high-quality graphene electronics. *Nature Nanotechnology* **5**, 722–726 (2010).

[22] Golberg, D., Bando, Y., Huang, Y., Terao, T., Mitome, M., Tang, C. & Zhi, C. Boron nitride nanotubes and nanosheets. *ACS Nano* **4**, 2979–2993 (2010).

[23] Chhowalla, M., Shin, H. S., Eda, G., Li, L.-J., Loh, K. P. & Zhang, H. The chemistry of two-dimensional layered transition metal dichalcogenide nanosheets. *Nature Chemistry* **5**, 263–275 (2013).

[24] Mak, K. F., Lee, C., Hone, J., Shan, J. & Heinz, T. F. Atomically thin mos 2: a new direct-gap semiconductor. *Physical Review Letters* **105**, 136805 (2010).

[25] Kam, K. & Parkinson, B. Detailed photocurrent spectroscopy of the semiconducting group vib transition metal dichalcogenides. *The Journal of Physical Chemistry* **86**, 463–467 (1982).

[26] Beal, A., Hughes, H. & Liang, W. The reflectivity spectra of some group va transition metal dichalcogenides. *Journal of Physics C: Solid State Physics* **8**, 4236 (1975).

[27] Li, H., Zhang, Q., Yap, C. C. R., Tay, B. K., Edwin, T. H. T., Olivier, A. & Baillargeat, D. From bulk to monolayer mos2: evolution of raman scattering. *Advanced Functional Materials* **22**, 1385–1390 (2012).

[28] Yu, Y., Li, C., Liu, Y., Su, L., Zhang, Y. & Cao, L. Controlled scalable synthesis of uniform, high-quality monolayer and few-layer mos2 films. *Scientific Reports* **3** (2013).

[29] Najmaei, S. *et al.* Vapour phase growth and grain boundary structure of molybdenum disulphide atomic layers. *Nature Materials* **12**, 754–759 (2013).

[30] Meyer, J. C., Geim, A. K., Katsnelson, M. I., Novoselov, K. S., Booth, T. J. & Roth, S. The structure of suspended graphene sheets. *Nature* **446**, 60–63 (2007).

[31] Alem, N., Erni, R., Kisielowski, C., Rossell, M., Gannett, W. & Zettl, A. Atomically thin hexagonal boron nitride probed by ultrahigh-resolution transmission electron microscopy. *Physical Review B* **80**, 155425 (2009).

[32] Krivanek, O. L. *et al.* Atom-by-atom structural and chemical analysis by annular dark-field electron microscopy. *Nature* **464**, 571–574 (2010).

[33] Brivio, J., Alexander, D. T. & Kis, A. Ripples and layers in ultrathin mos2 membranes. *Nano Letters* **11**, 5148–5153 (2011).

[34] Huang, P. Y. *et al.* Grains and grain boundaries in single-layer graphene atomic patchwork quilts. *Nature* **469**, 389–392 (2011).

[35] van der Zande, A. M. *et al.* Grains and grain boundaries in highly crystalline monolayer molybdenum disulphide. *Nature Materials* **12**, 554–561 (2013).

[36] Komsa, H.-P., Kurasch, S., Lehtinen, O., Kaiser, U. & Krasheninnikov, A. V. From point to extended defects in two-dimensional mos 2: evolution of atomic structure under electron irradiation. *Physical Review B* **88**, 035301 (2013).

[37] Girit, C. *et al.* Graphene at the edge: stability and dynamics. *Science* **323**, 1705–1708 (2009).

[38] Suenaga, K. & Koshino, M. Atom-by-atom spectroscopy at graphene edge. *Nature* **468**, 1088–1090 (2010).

[39] Zan, R., Ramasse, Q. M., Jalil, R., Georgiou, T., Bangert, U. & Novoselov, K. S. Control of radiation damage in mos2 by graphene encapsulation. *ACS Nano* **7**, 10167–10174 (2013).

[40] Pan, C., Nair, R., Bangert, U., Ramasse, Q., Jalil, R., Zan, R., Seabourne, C. & Scott, A. Nanoscale electron diffraction and plasmon spectroscopy of single-and few-layer boron nitride. *Physical Review B* **85**, 045440 (2012).

[41] Jinschek, J. R., Yucelen, E., Calderon, H. A. & Freitag, B. Quantitative atomic 3-d imaging of single/double sheet graphene structure. *Carbon* **49**, 556–562 (2011).

[42] Gass, M. H., Bangert, U., Bleloch, A. L., Wang, P., Nair, R. R. & Geim, A. K. Free-standing graphene at atomic resolution. *Nature Nanotechnology* **3**, 676–681 (2008).

[43] Bangert, U. *et al.* Stem plasmon spectroscopy of free standing graphene. *physica status solidi (a)* **205**, 2265–2269 (2008).

[44] Kotakoski, J., Jin, C., Lehtinen, O., Suenaga, K. & Krasheninnikov, A. Electron knock-on damage in hexagonal boron nitride monolayers. *Physical Review B* **82** (2010).

[45] Shi, Y., Huang, J.-K., Jin, L., Hsu, Y.-T., Yu, S. F., Li, L.-J. & Yang, H. Y. Selective decoration of au nanoparticles on monolayer mos2 single crystals. *Scientific reports* **3** (2013).

[46] Kelly, B. Thermal vibration amplitudes of carbon atoms in the graphite lattice parallel to the basal planes. *Journal of Nuclear Materials* **34**, 189–192 (1970).

[47] Schoenfeld, B., Huang, J. & Moss, S. Anisotropic mean-square displacements (msd) in single-crystals of 2h-and 3r-mos2. *Acta Crystallographica Section B: Structural Science* **39**, 404–407 (1983).

[48] Wen, J. *et al.* The formation and utility of sub-angstrom to nanometer-sized electron probes in the aberration-corrected transmission electron microscope at the university of illinois. *Microscopy and Microanalysis* **16**, 183–193 (2010).

[49] Loane, R. F., Xu, P. & Silcox, J. Thermal vibrations in convergent-beam electron diffraction. *Acta Crystallographica Section A* **47**, 267–278 (1991).

[50] Eda, G., Fujita, T., Yamaguchi, H., Voiry, D., Chen, M. & Chhowalla, M. Coherent atomic and electronic heterostructures of single-layer mos2. *ACS Nano* **6**, 7311–7317 (2012).

[51] Ramasse, Q. M., Seabourne, C. R., Kepaptsoglou, D.-M., Zan, R., Bangert, U. & Scott, A. J. Probing the bonding and electronic structure of single atom dopants in graphene with electron energy loss spectroscopy. *Nano Letters* **13**, 4989–4995 (2013).

[52] Fertig, J. & Rose, H. Resolution and contrast of crystalline objects in high-resolution scanning-transmission electron-microscopy. *Optik* **59**, 407–429 (1981).

[53] Loane, R. F., Kirkland, E. J. & Silcox, J. Visibility of single heavy atoms on thin crystalline silicon in simulated annular dark-field stem images. *Acta Crystallographica Section A* **44**, 912–927 (1988).

[54] Lebeau, J. M. & Stemmer, S. Experimental quantification of annular dark-field images in scanning transmission electron microscopy. *Ultramicroscopy* **108**, 1653–8 (2008).

[55] MacArthur, K., Pennycook, T., Okunishi, E., D'Alfonso, A., Lugg, N., Allen, L. & Nellist, P. Probe integrated scattering cross sections in the analysis of atomic resolution haadf stem images. *Ultramicroscopy* **133**, 109–119 (2013).

[56] Zhou, W. *et al.* Intrinsic structural defects in monolayer molybdenum disulfide. *Nano Letters* **13**, 2615–2622 (2013).

[57] Meyer, J., Geim, A., Katsnelson, M., Novoselov, K., Obergfell, D., Roth, S., Girit, C. & Zettl, A. On the roughness of single- and bi-layer graphene membranes. *Solid State Communications* **143**, 101–109 (2007).

[58] Kumar, P., Agrawal, K. V., Tsapatsis, M. & Mkhoyan, K. A. Quantification of thickness and wrinkling of exfoliated two-dimensional zeolite nanosheets. *Nature Communications* **6** (2015).

[59] Coppens, P. *X-Ray Charge Densities and Chemical Bonding*, vol. 4 (Oxford University Press, New York, 1997).

[60] Zuo, J. M., Kim, M., O'Keeffe, M. & Spence, J. C. H. Direct observation of d-orbital holes and cu-cu bonding in cu2o. *Nature* **401**, 49–52 (1999).

[61] Zuo, J. M. Measurements of electron densities in solids: a real-space view of electronic structure and bonding in inorganic crystals. *Reports on Progress in Physics* **67**, 2053 (2004).

[62] Nakashima, P. N. H., Smith, A. E., Etheridge, J. & Muddle, B. C. The bonding electron density in aluminum. *Science* **331**, 1583–1586 (2011).

[63] Eguchi, T. *et al.* Imaging of all dangling bonds and their potential on the ge/si(105) surface by noncontact atomic force microscopy. *Physical Review Letters* **93**, 266102 (2004).

[64] Gross, L., Mohn, F., Moll, N., Liljeroth, P. & Meyer, G. The chemical structure of a molecule resolved by atomic force microscopy. *Science* **325**, 1110–1114 (2009).

[65] Lee, H. J. & Ho, W. Single-bond formation and characterization with a scanning tunneling microscope. *Science* **286**, 1719–1722 (1999).

[66] Weiss, C., Wagner, C., Temirov, R. & Tautz, F. S. Direct imaging of intermolecular bonds in scanning tunneling microscopy. *Journal of the American Chemical Society* **132**, 11864–11865 (2010).

[67] Kimoto, K., Asaka, T., Nagai, T., Saito, M., Matsui, Y. & Ishizuka, K. Element-selective imaging of atomic columns in a crystal using stem and eels. *Nature* **450**, 702–4 (2007).

[68] Muller, D. A., Kourkoutis, L. F., Murfitt, M., Song, J. H., Hwang, H. Y., Silcox, J., Dellby, N. & Krivanek, O. L. Atomic-scale chemical imaging of composition and bonding by aberration-corrected microscopy. *Science* **319**, 1073–1076 (2008).

[69] D'Alfonso, A. J., Freitag, B., Klenov, D. & Allen, L. J. Atomic-resolution chemical mapping using energy-dispersive x-ray spectroscopy. *Physical Review B* **81**, 100101 (2010).

[70] Chu, M. W., Liou, S. C., Chang, C. P., Choa, F. S. & Chen, C. H. Emergent chemical mapping at atomic-column resolution by energy-dispersive x-ray spectroscopy in an aberration-corrected electron microscope. *Physical Review Letters* **104**, 196101 (2010).

[71] Kothleitner, G., Neish, M. J., Lugg, N. R., Findlay, S. D., Grogger, W., Hofer, F. & Allen, L. J. Quantitative elemental mapping at atomic resolution using x-ray spectroscopy. *Physical Review Letters* **112**, 085501 (2014).

[72] Lu, P., Romero, E., Lee, S., MacManus-Driscoll, J. L. & Jia, Q. Chemical quantification of atomic-scale eds maps under thin specimen conditions. *Microscopy and Microanalysis* **20**, 1782–1790 (2014).

[73] O'Keefe, M. A., Buseck, P. R. & Iijima, S. Computed crystal structure images for high resolution electron microscopy. *Nature* **274**, 322–324 (1978).

[74] Kirkland, E. J., Loane, R. F. & Silcox, J. Simulation of annular dark field stem images using a modified multislice method. *Ultramicroscopy* **23**, 77–96 (1987).

[75] Chakoumakos, B. C. Systematics of atomic displacement parameters in perovskite oxides. *Physica B: Condensed Matter* **241243**, 361–363 (1997).

[76] Oxley, M. P. & Allen, L. J. Impact parameters for ionization by high-energy electrons. *Ultramicroscopy* **80**, 125–131 (1999).

[77] Allen, L. J. & Josefsson, T. W. Inelastic scattering of fast electrons by crystals. *Physical Review B* **52**, 3184–3198 (1995).

[78] Oxley, M. P. & Allen, L. J. Delocalization of the effective interaction for inner-shell ionization in crystals. *Physical Review B* **57**, 3273–3282 (1998).

[79] Cosgriff, E. C., Oxley, M. P., Allen, L. J. & Pennycook, S. J. The spatial resolution of imaging using core-loss spectroscopy in the scanning transmission electron microscope. *Ultramicroscopy* **102**, 317–326 (2005).

[80] Allen, L. J., DAlfonso, A. J. & Findlay, S. D. Modelling the inelastic scattering of fast electrons. *Ultramicroscopy* **151**, 11–22 (2015).

[81] Watanabe, K., Yamazaki, T., Kikuchi, Y., Kotaka, Y., Kawasaki, M., Hashimoto, I. & Shiojiri, M. Atomic-resolution incoherent high-angle annular dark field stem images of si(011). *Physical Review B* **63**, 085316 (2001).

[82] Etheridge, J., Lazar, S., Dwyer, C. & Botton, G. A. Imaging high-energy electrons propagating in a crystal. *Physical Review Letters* **106** (2011).

[83] Perdew, J. P., Burke, K. & Ernzerhof, M. Generalized gradient approximation made simple. *Physical Review Letters* **77**, 3865–3868 (1996).

[84] Giannozzi, P. *et al.* Quantum espresso: a modular and open-source software project for quantum simulations of materials. *Journal of Physics: Condensed Matter* **21**, 395502 (2009).

[85] Richardson, W. H. Bayesian-based iterative method of image restoration. *Journal of the Optical Society of America* **62**, 55–59 (1972).

[86] Biggs, D. S. C. & Andrews, M. Acceleration of iterative image restoration algorithms. *Applied Optics* **36**, 1766–1775 (1997).

[87] White, R. L. Image restoration using the damped richardson-lucy method. In Crawford, D. L. & Craine, E. R. (eds.) *Instrumentation in Astronomy VIII*, vol. 2198, 1342–1348 (SPIE Proceedings 2198, 1994).

[88] Lugg, N. R., Neish, M. J., Findlay, S. D. & Allen, L. J. Practical aspects of removing the effects of elastic and thermal diffuse scattering from spectroscopic data for single crystals. *Microscopy and Microanalysis* **20**, 1078–1089 (2014).

[89] Penrose, R. A generalized inverse for matrices. *Mathematical Proceedings of the Cambridge Philosophical Society* **51**, 406–413 (1955).

[90] Paige, C. C. & Saunders, M. A. Lsqr: An algorithm for sparse linear equations and sparse least squares. *ACM Transactions on Mathematical Software* **8**, 43–71 (1982).

[91] Yankovich, A. B. *et al.* Picometre-precision analysis of scanning transmission electron microscopy images of platinum nanocatalysts. *Nature Communications* **5** (2014).

[92] Zuo, J. M., Blaha, P. & Schwarz, K. The theoretical charge density of silicon: experimental testing of exchange and correlation potentials. *Journal of Physics: Condensed Matter* **9**, 7541 (1997).

[93] Cowley, J. M. Scanning transmission electron microscopy of thin specimens. *Ultramicroscopy* **2**, 3–16 (1976).

[94] Pennycook, S. & Boatner, L. Chemically sensitive structure-imaging with a scanning transmission electron microscope. *Nature* **336**, 565–567 (1988).

[95] Nellist, P. D. *et al.* Direct sub-angstrom imaging of a crystal lattice. *Science* **305**, 1741–1741 (2004).

[96] Erni, R., Rossell, M. D., Kisielowski, C. & Dahmen, U. Atomic-resolution imaging with a sub-50-pm electron probe. *Physical Review Letters* **102** (2009).

[97] Mittal, A. & Mkhoyan, K. A. Limits in detecting an individual dopant atom embedded in a crystal. *Ultramicroscopy* **111**, 1101–1110 (2011).

[98] Hillyard, S., Loane, R. F. & Silcox, J. Annular dark-field imaging: Resolution and thickness effects. *Ultramicroscopy* **49**, 14–25 (1993).

[99] Ishizuka, K. Prospects of atomic resolution imaging with an aberrationcorrected stem. *Journal of electron microscopy* **50**, 291–305 (2001).

[100] Allen, L. J., Findlay, S. D., Oxley, M. P. & Rossouw, C. J. Lattice-resolution contrast from a focused coherent electron probe. part i. *Ultramicroscopy* **96**, 47–63 (2003).

[101] Kourkoutis, L. F., Parker, M. K., Vaithyanathan, V., Schlom, D. G. & Muller, D. A. Direct measurement of electron channeling in a crystal using scanning transmission electron microscopy. *Physical Review B* **84** (2011).

[102] Smyth, D. M. Defects and order in perovskite-related oxides. *Annual Review of Materials Science* **15**, 329–357 (1985).

[103] Hwang, H. Y., Iwasa, Y., Kawasaki, M., Keimer, B., Nagaosa, N. & Tokura, Y. Emergent phenomena at oxide interfaces. *Nature Materials* **11**, 103–113 (2012). 10.1038/nmat3223.

[104] Kohn, W. & Sham, L. J. Self-consistent equations including exchange and correlation effects. *Physical Review* **140**, A1133–A1138 (1965).

[105] Ewald, P. P. Die berechnung optischer und elektrostatischer gitterpotentiale. *Annalen der Physik* **369**, 253–287 (1921).

[106] Dwyer, C. & Etheridge, J. Scattering of angstrom-scale electron probes in silicon. *Ultramicroscopy* **96**, 343–360 (2003).

[107] Hall, C. R. & Hirsch, P. B. Effect of thermal diffuse scattering on propagation of high energy electrons through crystals. *Proceedings of the Royal Society of London A: Mathematical, Physical and Engineering Sciences* **286**, 158–177 (1965).

[108] Wang, Z. L. & Cowley, J. M. Simulating high-angle annular dark-field stem images including inelastic thermal diffuse scattering. *Ultramicroscopy* **31**, 437–453 (1989).

[109] Fanidis, C., Van Dyck, D. & Van Landuyt, J. Inelastic scattering of high-energy electrons in a crystal in thermal equilibrium with the environment ii. solution of the equations and applications to concrete cases. *Ultramicroscopy* **48**, 133–164 (1993).

[110] Forbes, B. D., Martin, A. V., Findlay, S. D., DAlfonso, A. J. & Allen, L. J. Quantum mechanical model for phonon excitation in electron diffraction and imaging using a born-oppenheimer approximation. *Physical Review B* **82** (2010).

[111] LeBeau, J. M., D'Alfonso, A. J., Findlay, S. D., Stemmer, S. & Allen, L. J. Quantitative comparisons of contrast in experimental and simulated bright-field scanning transmission electron microscopy images. *Physical Review B* **80** (2009).

[112] Muller, D. A., Edwards, B., Kirkland, E. J. & Silcox, J. Simulation of thermal diffuse scattering including a detailed phonon dispersion curve. *Ultramicroscopy* **86**, 371–380 (2001).

[113] Martin, A. V., Findlay, S. D. & Allen, L. J. Model of phonon excitation by fast electrons in a crystal with correlated atomic motion. *Physical Review B* **80** (2009).

[114] Stadelmann, P. A. Ems - a software package for electron diffraction analysis and hrem image simulation in materials science. *Ultramicroscopy* **21**, 131–145 (1987).

[115] Suenaga, K., Okazaki, T., Okunishi, E. & Matsumura, S. Detection of photons emitted from single erbium atoms in energy-dispersive x-ray spectroscopy. *Nature Photonics* **6**, 545–548 (2012).

[116] Allen, L. J., Findlay, S. D., Lupini, A. R., Oxley, M. P. & Pennycook, S. J. Atomic-resolution electron energy loss spectroscopy imaging in aberration corrected scanning transmission electron microscopy. *Physical Review Letters* **91** (2003).

[117] LeBeau, J. M., Findlay, S. D., Allen, L. J. & Stemmer, S. Quantitative atomic resolution scanning transmission electron microscopy. *Physical Review Letters* **100** (2008).

[118] Rosenauer, A., Gries, K., Muller, K., Pretorius, A., Schowalter, M., Avramescu, A., Engl, K. & Lutgen, S. Measurement of specimen thickness and composition

in al(x)ga(1-x)n/gan using high-angle annular dark field images. *Ultramicroscopy* **109**, 1171–82 (2009).

[119] LeBeau, J. M., Findlay, S. D., Wang, X., Jacobson, A. J., Allen, L. J. & Stemmer, S. High-angle scattering of fast electrons from crystals containing heavy elements: Simulation and experiment. *Physical Review B* **79** (2009).

[120] Dwyer, C., Maunders, C., Zheng, C. L., Weyland, M., Tiemeijer, P. C. & Etheridge, J. Sub-0.1-angstrom-resolution quantitative scanning transmission electron microscopy without adjustable parameters. *Applied Physics Letters* **100**, 191915 (2012).

[121] Xin, H. L., Dwyer, C. & Muller, D. A. Is there a stobbs factor in atomic-resolution stem-eels mapping? *Ultramicroscopy* **139**, 38–46 (2014).

[122] Ishikawa, R., Lupini, A. R., Findlay, S. D. & Pennycook, S. J. Quantitative annular dark field electron microscopy using single electron signals. *Microscopy and microanalysis : the official journal of Microscopy Society of America, Microbeam Analysis Society, Microscopical Society of Canada* **20**, 99–110 (2014).

[123] Hwang, J., Zhang, J. Y., DAlfonso, A. J., Allen, L. J. & Stemmer, S. Three-dimensional imaging of individual dopant atoms insrtio3. *Physical Review Letters* **111** (2013).

[124] Ishikawa, R., Lupini, A. R., Findlay, S. D., Taniguchi, T. & Pennycook, S. J. Three-dimensional location of a single dopant with atomic precision by aberration-corrected scanning transmission electron microscopy. *Nano Letters* **14**, 1903–8 (2014).

[125] Findlay, S. D. & LeBeau, J. M. Detector non-uniformity in scanning transmission electron microscopy. *Ultramicroscopy* **124**, 52–60 (2013).

[126] Martinez, G. T., Jones, L., De Backer, A., Beche, A., Verbeeck, J., Van Aert, S. & Nellist, P. D. Quantitative stem normalisation: The importance of the electron flux. *Ultramicroscopy* **159P1**, 46–58 (2015).

[127] Lebeau, J. M., Findlay, S. D., Allen, L. J. & Stemmer, S. Position averaged convergent beam electron diffraction: theory and applications. *Ultramicroscopy* **110**, 118–25 (2010).

[128] Xin, H. L., Zhu, Y. & Muller, D. A. Determining on-axis crystal thickness with quantitative position-averaged incoherent bright-field signal in an aberration-corrected stem. *Microscopy and Microanalysis* **18**, 720–727 (2012).

[129] Schulz, H. & Thiemann, K. H. Crystal structure refinement of aln and gan. *Solid State Communications* **23**, 815–819 (1977).

[130] Lawrence, J. Debye-waller factors for magnesium oxide. *Acta Crystallographica Section A* **29**, 94–95 (1973).

[131] Yamazaki, T., Kawasaki, M., Watanabe, K., Hashimoto, I. & Shiojiri, M. Effect of small crystal tilt on atomic-resolution high-angle annular dark field stem imaging. *Ultramicroscopy* **92**, 181–189 (2002).

[132] Maccagnano-Zacher, S. E., Mkhoyan, K. A., Kirkland, E. J. & Silcox, J. Effects of tilt on high-resolution adf-stem imaging. *Ultramicroscopy* **108**, 718–26 (2008).

[133] Verbeeck, J., Bch, A. & Van den Broek, W. A holographic method to measure the source size broadening in stem. *Ultramicroscopy* **120**, 35–40 (2012).

[134] Mkhoyan, K. A., Maccagnano-Zacher, S. E., Kirkland, E. J. & Silcox, J. Effects of amorphous layers on adf-stem imaging. *Ultramicroscopy* **108**, 791–803 (2008).

[135] Mkhoyan, K. A., Maccagnano-Zacher, S. E., Thomas, M. G. & Silcox, J. Critical role of inelastic interactions in quantitative electron microscopy. *Phys. Rev. Lett.* **100**, 025503 (2008).

Appendix A

Slice thickness effects in multislice simulation

In the TEMSIM multislice code [14] the scattering atoms of the specimen are modeled as 2-D projected atomic potentials that are calculated from parametrized electron scattering factors of atoms (using the Hartree-Fock approximation), equivalent to integrating the 3-D electrostatic potentials of individual atoms along the z-axis from $-\infty$ to $+\infty$. The validity of this infinite z-projection method was tested by comparing the results of beam propagation simulations in a crystal using this simple model with results from a more accurate model. For better accuracy, 3-D charge densities of atoms were calculated using the DFT-based Quantum Espresso code [84] with PBE-GGA functionals [83] and then inverted to 3-D electrostatic potentials using a FFT-based solution of Poissons equation. [105] The potential could then be sampled with sub-atomic slicing, the projected sub-atomic potentials being calculated by integrating only over the corresponding sub-atomic slice thickness. The results are shown in Figure A.1. Here, for beam energy $E = 100$ keV and $\alpha_{obj} = 25$ mrad, aberration-free STEM probe intensity profiles were calculated in an isolated column of Ge with a z-spacing of 2 Ådown the atomic column, employing varying slice thicknesses. The results show that simple and more accurate models produce very similar beam behavior as the beam travels through an atomic column. The very small discrepancies are due to differences in the bandwidth-limiting schemes of the two different models, resulting in slightly sharper peaks in the projected potential for the PBE-GGA-based model.

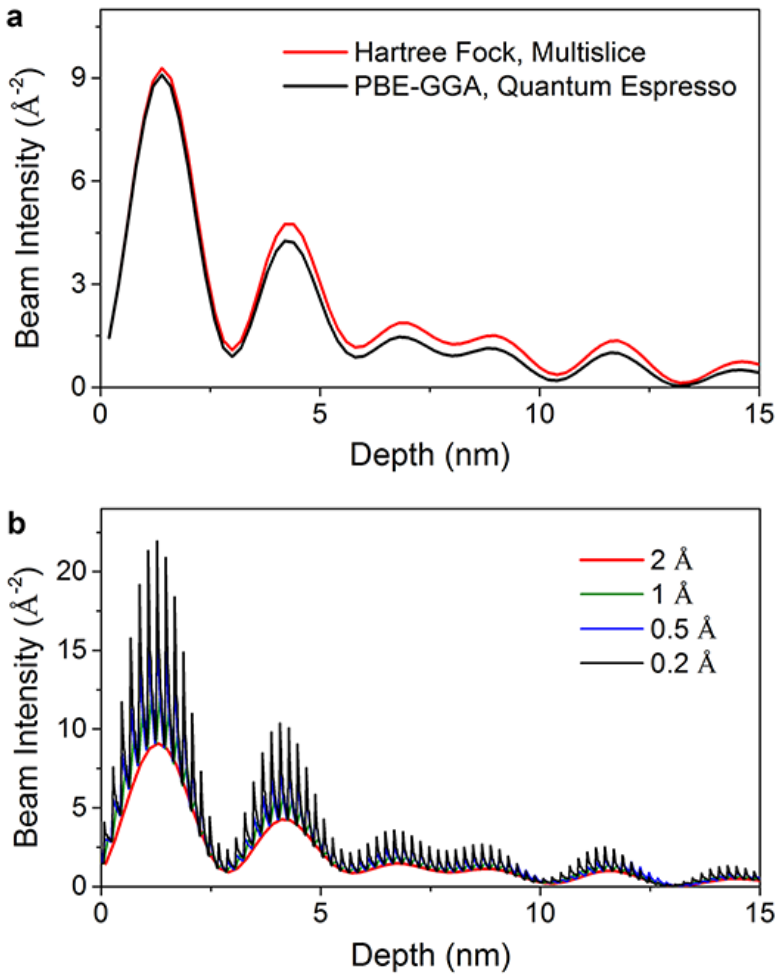

Figure A.1: Beam intensity profiles of $E_0 = 100$ keV and $\alpha_{obj} = 25$mrad aberration-free STEM probe in an isolated column of Ge with interatomic spacing 2 Å. (a) Comparison of two methods used to calculate projected atomic potentials: (i) integration along the entire z-axis with 3-D atomic potentials calculated using Hartree-Fock approximation (standard multislice approach implemented in TEMSIM) and (ii) integration along the z-axis through the slice thickness of 3-D atomic potentials calculated using Quantum Espresso code with PBE-GGA functionals. (b) Comparison of beam intensity profiles simulated with projected atomic potentials calculated using Quantum Espresso code with PBE-GGA functionals with different slicing, including sub-atomic slicing (0.5 and 0.2 Åslice thicknesses).